MAGNETIC AND ELECTRONIC PROPERTIES OF RATTLING SYSTEMS, AN EXPERIMENTAL AND THEORETICAL STUDY

A Dissertation

by

SERGIO YANUEN RODRÍGUEZ ROBLES

Submitted to the Office of Graduate Studies of
Texas A&M University
in partial fulfillment of the requirements for the degree of

DOCTOR OF PHILOSOPHY

August 2011

Major Subject: Physics

MAGNETIC AND ELECTRONIC PROPERTIES OF RATTLING SYSTEMS, AN EXPERIMENTAL AND THEORETICAL STUDY

A Dissertation

by

SERGIO YANUEN RODRÍGUEZ ROBLES

Submitted to the Office of Graduate Studies of
Texas A&M University
in partial fulfillment of the requirements for the degree of

DOCTOR OF PHILOSOPHY

Approved by:

Chair of Committee,	Joseph H. Ross, Jr.
Committee Members,	Donald G. Naugle
	Glenn Agnolet
	Tahir Cagin
Head of Department,	Edward S. Fry

August 2011

Major Subject: Physics

ABSTRACT

Magnetic and Electronic Properties in Rattling Systems,
an Experimental and Theoretical Study. (August 2011)
Sergio Yanuen Rodríguez Robles, B.S., Universidad Autónoma de Zacatecas;
M.S., University of Texas at El Paso
Chair of Advisory Committee: Dr. Joseph H. Ross, Jr.

The search for heat regenerators is currently very important due to the amount of wasted heat produced in different human activities. Thermoelectric materials have emerged as a possible solution to the world's demand and reuse of energy. Recent advances have included the development of materials with tailored phonon properties, including localized "rattling" oscillator modes. In addition a number of interesting physical properties have emerged in rattling systems. This dissertation reports a study of several such systems, experimentally and computationally. Experiments performed include XRD, electron micro-probe, electrical and thermal conductivity, Seebeck coefficient measurements, dc magnetization, dc susceptibility and NMR. In the computational side several $ab-initio$ models have been considered to understand the structural, vibrational and magnetic properties observed in these compounds.

Among the studied compounds, the Fe-Al-Zn materials showed interesting magnetic properties combined with anomalous vibrational behavior in a chain geometry. Computational results indicated that the moment is affected by Fe antisites, but also the neighbor configuration contributes to it.

Al-V-La is an example of a classical Einstein oscillator material. These properties are related to the existence of loose atoms inside the material. A purely computational study on these materials denoted the existence of two weakly bonded sites.

The clathrate structural results from first-principles considerations elucidated the preferred structural configurations in several clathrates. This included Ba-Cu-Ge clathrates, where it was confirmed that the compound follows the Zintl electron counting balance. Also the bonding inside these materials was studied to address the binding of the local-oscillator atoms within the material.

For Ba-Ga-Sn clathrates an unusual dimorphism was studied, with both of the two different types of structures investigated. For type-I $Ba_8Ga_{16}Sn_{30}$ the preferred configuration was obtained from NMR lineshape simulations and energy considerations. For the type-VIII $Ba_8Ga_{16}Sn_{30}$ the experimental thermoelectric properties were analyzed in conjunction with computational modeling.

Finally in Ba-Al-Ge clathrates the local environments, preferred configuration and vacancy formation were clarified. This included an extensive experimental and computational study on $Ba_8Al_xGe_{46-x-y}\square_y$ systems. The different local Al environments were elucidated, with the location of vacancies influencing the surroundings. Also the correlation between the Al substitution and number of vacancies was studied.

To my wife, son and family

ACKNOWLEDGMENTS

I would like to recognize and express my sincere gratitude to my advisor Dr. Joseph H. Ross, Jr., for all the support, encouragement and patience shown throughout these years. I enjoyed all the work done and the fruitful discussions that we had during my Ph.D. period.

While working on the understanding needed for this dissertation, I was able to work and interact with a large number of collaborators: K. D. D. Rathnayaka, KyongWan Kim, Federico Lopez, Arlene Ford, Levica Smith, Sean Grant. I also worked closely with members of Dr. Ross's group: Venkat Goruganti, Weiping Gou, Ji Chi, Haoyu Qian, Xiang Zheng, Laziz Saribaev and Jing-Han Chen. A special mention goes to Lisa Perez for the help provided regarding linux problems.

I give many thanks to Dr. Donald Naugle for allowing me to use the arc melting and PPMS. I also thank the Chemistry Department for the use of XRD, and SQUID. I also acknowledge the Supercomputer Center for the computing time provided.

I would like to thank the members of my committee Donald Naugle, Glenn Agnolet, and Tahir Cagin for their input, time and suggestions.

Very special recognition goes to all my family for all the encouragement and support through all these years. I really owe special gratitude to my wife, Iliana Sanchez and son, Santiago, for all their patience, support, encouragement and especially my wife for everything she has done for me over these years.

Last but not least, I would like to acknowledge Conacyt, the Robert A. Welch Foundation and the Physics Department for financial support during my Ph.D. studies.

TABLE OF CONTENTS

CHAPTER Page

LIST OF TABLES

TABLE Page

LIST OF FIGURES

FIGURE Page

FIGURE Page

CHAPTER I

INTRODUCTION

A. Background

Huge amounts of wasted heat are generated by oil combustion, industrial processes, and home heating, and this also makes a big impact in the environment. Recently thermoelectric (TE) generators and refrigerators have emerged as a possible solution for the world's energy demand and use of wasted heat. Research in TE's started in the first decades of the XIX century when the macroscopic effects were all discovered. In TE's the presence of electrical currents coupled with thermal currents lead to different types of effects depending on the conditions and injected current. TE coolers use the Peltier effect, where the application of an electric current creates a temperature difference. Meanwhile TE generators use the Seebeck effect, wherein a gradient in temperature generates an electric voltage.

TE's have been known for long time, but due to the conflicting properties needed to make a good thermoelectric material they were inefficient and not cost-effective. Recent development of complex high-efficiency materials has led to a renaissance in the field. For example, in the mid 1990s theoretical predictions suggested that nanostructural engineering could lead to significantly improved efficiency. At the same time complex bulk structures (skutterudites [1], Zintl phases [2] and clathrates [3]) also showed enhanced efficiencies. Different approaches have been followed in the development of new materials, from complexity within the unit cell to nanostructured and thin films, some of which approaches will be described here.

This dissertation follows the style of Physical Review B.

B. Selection and Optimization Criteria

The maximum efficiency of a TE material is characterized by the dimensionless figure of merit

$$ZT = \frac{S^2 \sigma T}{\kappa} \tag{1.1}$$

where S is the Seebeck coefficient, σ the electrical conductivity, and κ the thermal conductivity. Thus to maximize ZT a large Seebeck coefficient, high electrical conductivity and low thermal conductivity are needed. These quantities are not independent since usually when S increases, σ decreases. As an example in a metal or degenerate semiconductor, the Seebeck coefficient is given by [4]

$$S = \frac{8\pi^2 k_B^2}{3eh^2} m^* T \left(\frac{\pi}{3n}\right)^{2/3}, \tag{1.2}$$

whereby to maximize ZT a low carrier concentration is needed. However the electrical conductivity or resistivity is related to n by $\frac{1}{\rho} = \sigma = ne\mu$, hence low n gives a decrease in the conductivity, and consequently ZT. Moreover large effective masses produce high Seebeck coefficients (as seen from Eq. (1.2)) but also low conductivity due to the heavy carriers having slower velocities and thus small mobilities. Therefore different conflicts arise in the design of a good TE material. Consequently a balance between high effective masses and high mobilities must be found. It was proposed that electron confinement produced high effective masses and therefore large Seebeck coefficients [5]. Also the Seebeck coefficient and electrical conductivity may be decoupled due to electron filtering [6]. In this technique barriers are created in bulk materials to create a superlattice, then only electrons with high energy will be able for thermionic emission over the barrier, enhancing the Seebeck coefficient.

Another problem in optimizing ZT is the low thermal conductivity required. In TE materials the thermal conductivity is composed of two parts: $\kappa = \kappa_e + \kappa_l$, where

κ_e is due to the heat transported by electrons and holes, while κ_l is due to the phonons traveling through the lattice. Normally $\kappa_e = L\sigma T = ne\mu LT$ where L is the Lorenz factor. There are different strategies to reduce κ_l including rattling structures, separation of electron-crystal from phonon glass behavior and the scattering of phonons at interfaces. Ideally a good thermoelectric material should be able to decouple these conflicting properties. Below some of the different materials with high thermoelectric properties are discussed.

C. Established and Future Materials for Thermoelectric Applications

Several materials are already established as thermoelectrics, and are used for specific purposes. For example due to their reliability thermoelectric coolers were used by NASA for Cassini spacecraft. However the thermal and transport properties can be enhanced for better performance and for more widespread application. In Fig. 1 a number of different commercially available thermoelectric materials [7] are shown together with their figure of merit in the temperature range of enhanced thermoelectric properties. A good thermoelectric material desired for applications needs to have a $ZT > 1$. Next I describe some of the established materials and briefly discuss some of the trends for future materials in thermoelectric applications.

1. Group V_2-VI_3

Bismuth telluride (Bi_2Te_3) is a simple compound semiconductor useful for thermoelectric refrigeration at ordinary temperatures. Its structure is formed by planes with the following construction Te_1-Bi-Te_2-Bi-Te_1-Bi-Te_2-Bi... perpendicular to the c axis. The Bi and Te layers have strongly ionic-covalent bonds but there are no electrons to bind the remaining Te_1 layers [8]. One important property that limits a

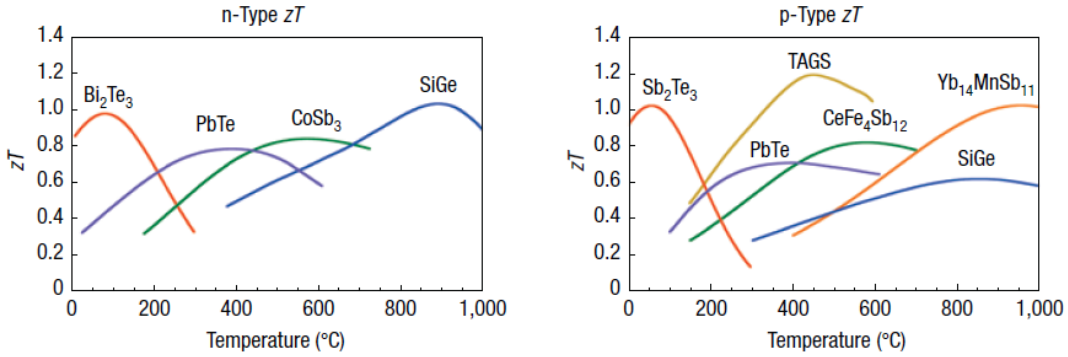

Fig. 1. Figure of merit for commercially available thermoelectrics. Left n-type, right p-type. Reprinted by permission from [7] ©(2008) Macmillan Publishers Ltd: Nature Materials.

higher ZT in these materials is the easy diffusion of copper, silver and gold at relatively low temperatures [9]. Copper, silver and gold act as donor impurities changing the thermoelectric properties. Intrinsic bismuth telluride is p-type and has a Seebeck coefficient of about 230 μV K^{-1}. The Seebeck coefficient falls when acceptor impurities are added and the resistivity decreases. On the other hand when donor impurities are added, S reaches a maximum of about 260 μV K^{-1}, then falls to zero and reaches a minimum at about -270 μV K^{-1}. S is independent of orientation for extrinsic bismuth telluride [10]. The electronic and thermal parts of the thermal conductivity are of comparable magnitude in these structures [11]. These compounds show a low $\kappa = 1.5$ Wm^{-1}K^{-1} perpendicular to the c axis [12] and $\kappa = 0.7$ Wm^{-1}K^{-1} parallel to the c axis at 300 K [10].

Addition of antimony and/or selenium to bismuth telluride improves the figure of merit mainly because there is a reduction in κ_L [13]. The best $p-$type compositions for thermoelectric refrigeration are $Bi_{0.5}Sb_{1.5}Te_3$ and for n-type $Bi_2Te_{2.7}Se_{0.3}$. The thermoelectric properties of these commercial alloys are $S = \pm 210 \mu$V K^{-1}, $\rho = 1.0 \times 10^{-5} \Omega$m, $\kappa = 1.4$ Wm^{-1}K^{-1}, and $ZT = 0.9$ at room temperature.

2. Lead Telluride and Related Compounds

Lead telluride (PbTe) is a thermoelectric generator material that meets the high atomic weight that helps in the scattering of heat-carrying phonons and low thermal conductivity criteria with good electric properties. It has a cubic sodium chloride structure, so there is no anisotropy in the properties. PbTe was the first compound where the lattice thermal conductivity was reduced without a considerable change in the mobility [14]. It has a band gap of 0.32 eV at 300 K which permits the Seebeck coefficient to reach a value of 300 μVK^{-1} after doping. n and p-type can be produced by departures from stoichiometry [15]. The effective masses of both type carriers are 0.03 m$_e$. The dimensionless figure of merit is 0.3 at room temperature, but at higher temperature it becomes higher than that of Bi_2Te_3 [16]. It is possible to obtain a value close to one for Z_nT but the value of Z_pT is about 0.7 at 700 K when substituted with Te, Ag, Ge or Sb (known collectively as TAGS), where Z_nT refers to the n-type doped material and Z_pT to p-type doped, respectively. A high figure of merit of 1.4 is obtained by TAGS-85, 85% GeTe, at about 750 K, which reduces to 0.8 for temperatures of about 500 K, the S lies between 150 and 200 μVK^{-1} in this range [17].

3. Complex Nanostructured Materials

Given the practical limits in ZT thus far observed in bulk materials, it is important to identify additional means to improve the behavior. Creating artificially structured materials to reduce κ_l is one promising means to do this. Films of Bi_2Te_3-Sb_2Te_3 and PbTe-PbSe and Si nanowires have shown low thermal conductivity values (0.2-0.5 Wm^{-1}K^{-1}) [18, 19]. Very high dimensionless figures of merit ($ZT > 2$) have been reported on thin films but results are difficult to reproduce. The challenge for

a bulk nanostructured material is the electron scattering at the boundaries leading to a decrease in electrical as well as thermal conductivities [20]. To prevent grain-boundary scattering one method that was suggested is the spontaneous partitioning of a precursor phase into thermodynamically stable phases [21]. This means that the ideal nanostructured material could have thermodynamically stable, coherent, epitaxy-like, interfaces between the constituent phases. A fundamental problem with this approach is that rapid diffusion in the liquid phase leads to coarse microstructures [22, 23].

4. Phonon-Glass Electron-Crystal Materials

Another means to tailor the thermal conductivity, most relevant to the clathrates, is to incorporate "rattler" atoms, which may impede the phonon conductivity. Slack [24] introduced the Phonon-Glass Electron-Crystal (PGEC) concept. Materials demonstrating such behavior possesses good semiconductor electronic properties, but their thermal properties are equivalent with those associated with amorphous materials. Thermoelectric properties can also be enhanced by multiple valleys near the Fermi level which leads to a high effective mass. These types of properties have been identified in skutterudites and clathrates. The PGEC concept is one of the most significant innovations for thermoelectric in the last 30 years, but such materials are difficult to produce.

One very important property in the PGEC approach is to have very low thermal conductivity (κ) similar to amorphous materials. Based on an Einstein model Cahill [25] proposed that to obtain a low κ several attributes need to be fulfilled. The first requirement is possession of loose atoms, with no long-range correlations between the positions of the loose atoms. Also, there should not be disorder produced by point defects since this does not help in producing glass-like lattice vibrations. The

type of structure that may satisfy all the conditions is what is called the "open structure" compound. In such structures there is the possibility of obtaining good electrical properties. At minimum one of the sites may be inside the "cage" formed by the atoms in the other crystallographic sites. The movement of the atoms inside the cages produces the scattering of phonons that carry heat. The other framework atoms should dominate the electronic properties of the material.

CHAPTER II

GROUP IV CLATHRATES

The word clathrate comes from the Latin '*clatratus*' meaning with bars or a lattice. Hydrate clathrates have been known for more than a century. Cros and colleagues [26] reported in 1965 the existence of two clathrate phases isomorphic with hydrate clathrates such as $(Cl_2)_8(H_2O)_{46}$ and $(CCl_4)_8(H_2O)_{136}$. These were Na_8Si_{46} and $Na_{24}Si_{136}$. Clathrates have gained considerable attention due to their thermal and electrical properties, and potential for thermoelectric device application with possible phonon-glass electron-crystal (PGEC) behavior [27, 28, 29, 30, 31]. These materials have shown interesting properties such as rattling of the guest atoms at low frequencies [32], and carrier densities can also be adjusted [33], making them particularly attractive for several potential applications. Sometimes even the structure can be tuned as in the case of $Ba_8Ga_{16}Sn_{30}$ [34]. Recently much work has been devoted to $Ba_8Ga_{16}Ge_{30}$, which exhibits a particularly large thermoelectric efficiency at high temperatures. The change in molar ratio (Ga/Ge) was identified to lead to a large variation in thermoelectric properties [35, 36]. Superconductivity and magnetism has also been observed in a number of these clathrate materials [37, 38].

A. Clathrate Structures

The semiconductor clathrates consist typically of Si, Ge or Sn open sp^3 framework networks with guest atoms inside, even though some Si and Ge type-II clathrates can also be formed as empty frameworks [39, 40]. The most common kinds of clathrates are type-I such as Na_8Si_{46}, type-II such as above-mentioned $Na_{24}Si_{136}$ and type-VIII such as $Eu_8Ga_{16}Ge_{30}$. All of the clathrates structures are listed in Table I together with the ideal formula, where X and Y refers to different type cages and E is the

Table I. Structure types of clathrates, with an example of a corresponding material where available.

Type	Ideal formula	Polyhedral Void	Space group	Semiconductor Clathrate
I	6X2Y46E	$[5^{12}6^2]_6[5^{12}]_2$	$Pm\bar{3}n$	$Ba_8Al_{16}Ge_{30}$
II	8X16Y136E	$[5^{12}6^4]_8[5^{12}]_{16}$	$Fd\bar{3}m$	Na_xGe_{136}
III	20X10Y172E	$[5^{12}6^2]_{16}[5^{12}6^3]_4[5^{12}]_{10}$	$P4_2/mmm$	$Cs_{30}Na_{1.33x-10}Sn_{172-x}$
IV	8X6Y80E	$[5^{12}6^2]_4[5^{12}6^3]_4[5^{12}]_6$	$P6/mmm$	K_7Ge_{40-x}
V	4X8Y68E	$[5^{12}6^4]_4[5^{12}]_8$	$P6_3/mmc$	
VI	16X156E	$[4^35^96^27^3]_{16}[4^45^4]_{12}$	$I\bar{4}3d$	
VII	2X12E	$[4^66^8]_2$	$Im\bar{3}m$	
VIII	8Y46E	$[3^34^35^9]_8$	$Im\bar{3}m$	$Ba_8Ga_{16}Sn_{30}$
IX	16Y8X100E	$[5^{12}]_8 + [4^{10}]_4 + \ldots$	$P4_132$	Ba_6Ge_{25}

framework atoms. The polyhedral void is listed in the third column, the numbers indicate the constituent units of each cage, for example in type-I $[5^{12}6^2]_6$ represents the tetrakaidecahedron (large cage) that it composed of 12-five sided poligons and 2-six sided ones, as shown in Fig. 2. The space group is listed in the fourth column. Finally an example of each structure were available is included in the fifth column. For this study the relevant structures are type-I and type-VIII. In Figs. 2 and 3 the type-I and type-VIII structures are shown; both have cubic symmetry. The general formula for type-I and type-VIII is A_8E_{46}. In type-I every unit cell is formed by two dodecahedral cages and six tetrakaidecahedra as shown in Fig. 2. In the Wyckoff notation this structure has three framework sites, $6c$, $16i$ and $24k$, and also two guest sites, $2a$ and $6d$. In the type-VIII clathrates the unit cell is composed of eight distorted dodecahedra as shown in Fig. 3. In the Wyckoff notation type-VIII clathrates have

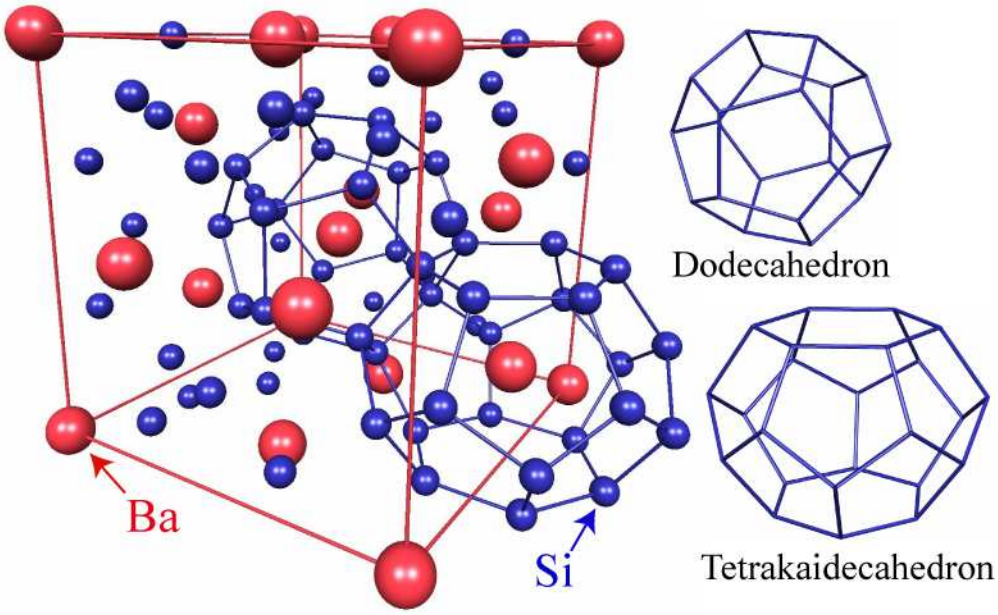

Fig. 2. Type-I clathrate structure, together with the two basic cages forming the framework and the cubic unit cell.

four framework sites 2a, 8c, 12d and 24g, and also one guest site 8c. In these formulas A typically represents alkali-metal or alkaline-earth atoms, and E a group IV element (Si, Ge, or Sn), although Zn, Cd, Al, Ga, In, Sb, or Bi and others can be substituted as well.

Semiconductor clathrates have covalent bonds between framework atoms and are very stable against chemical reagents. In clathrates the guest atoms are nominally not covalently bonded to atoms in the framework; rather they are free to move inside the cage ('rattling'). Guest atoms also behave as charge donors to stabilize the complete framework structure.

An important concept for clathrate stability is the Zintl concept [41], which states that: "the more electropositive 'guest'atoms donate their valence electrons to the more electronegative 'host'(or cage) atoms such that the latter complete their valence requirement (octet rule) and build a covalently bonded cage structure". For

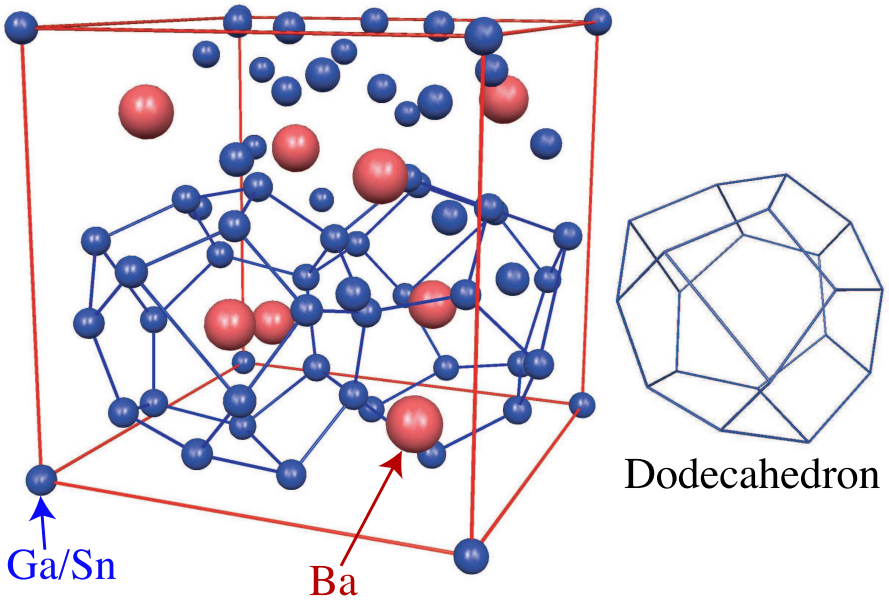

Fig. 3. Type-VIII clathrate structure, together with the basic cage forming the framework and the cubic unit cell.

example we consider $Ba_8Al_{16}Ge_{30}$ which is a Zintl phase. In this compound each framework atom has four framework neighbors. Ge has four valence electrons, but Al has only 3 valence electrons so in this composition we have a deficit of 16 electrons. However Ba adopts a 2^+ state and there are 8 Ba, so the extra 16 charges transfer to the framework giving a charge balance. In cases where this charge balancing is not achieved spontaneous vacancies can appear, as in the case of $Ba_8Ge_{43}\square_3$, where $\square$ represents the vacancy. In the latter case the vacancies also show ordering, arranging themselves in a helical path along the (100) direction [42, 43]. Each vacancy is expected to take up 4 electrons, so in the case of $Ba_8Ge_{43}\square_3$ only 12 electrons would be accommodated by the framework rather than the expected 16. This gives an indication of the limitations in the Zintl concept. There are also cases where there is an unbroken framework as in Ba_8Si_{46} [44], which has a large electron imbalance and is a good metal.

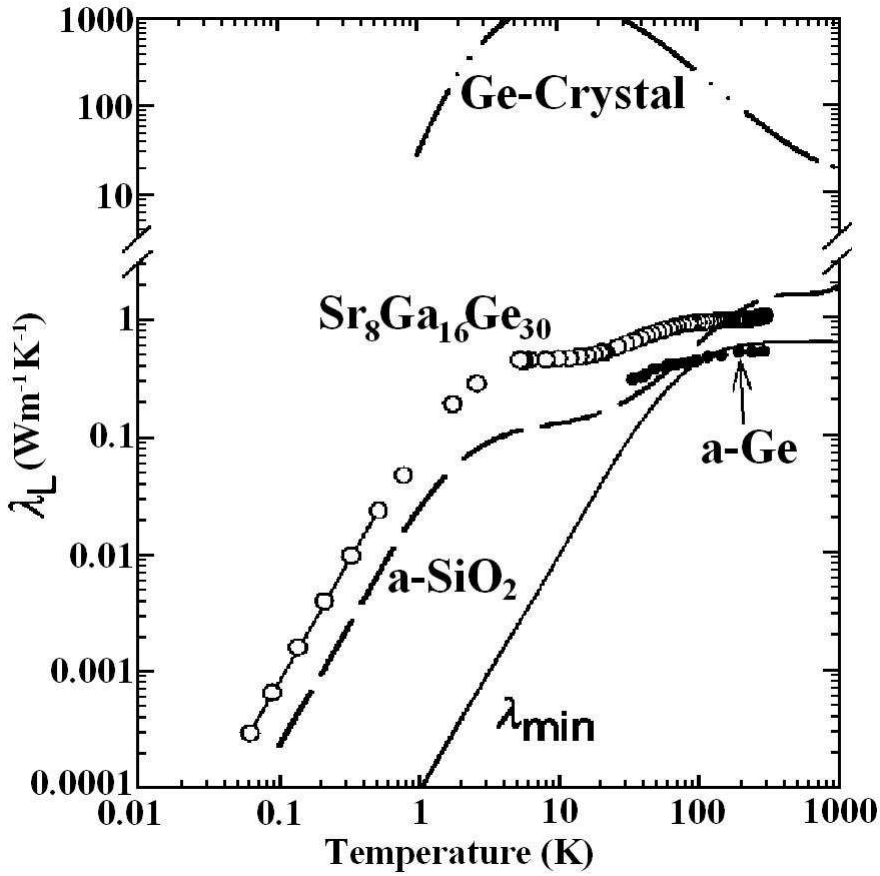

Fig. 4. Lattice thermal conductivity λ_L for different materials. λ_{min} represents the minimum lattice thermal conductivity for Ge. Reprinted with permission from [27] © (1998) American Institute of Physics.

B. Properties of Semiconductor Clathrates

In recent years clathrate research has regained interest following the 1998 work by Nolas *et al* [27]. This study found that in the temperature range $T < 300$ K, the lattice thermal conductivity for $Sr_8Ga_{16}Ge_{30}$ showed a magnitude and temperature dependence similar to amorphous Ge and amorphous SiO_2, where the main contribution comes from the scattering of acoustic phonons by the encaged ions resulting in low thermal conductivities. This situation gives these materials the potential for possible thermoelectric devices. The latter idea was first proposed by Slack [24] when

he expressed that the "rattling" of the atoms inside the cages may contribute to low thermal conductivities. In Fig. 4 it is shown that in the temperature range 30 K $\leq$ T $\leq$ 300 K, the thermal conductivity is close to that of amorphous Ge. Another indication of the "glass-like" thermal conductivity is the T^2 dependence at low temperature similar to amorphous materials. Therefore it is hoped that by adjusting the doping level a good figure of merit for thermoelectric applications can be obtained. Besides such practical issues many other properties have been observed in this type of materials such as superconductivity [37] and possible Rabi oscillators [45].

Superconductivity in clathrates was found by Kawaji *et al.* [37], in the type-I clathrate $Na_{2.9}Ba_{4.5}Si_{46}$, with a critical temperature of about $T_c = 4$ K. From magnetization measurements it was observed that its behavior corresponds to that of a type-II superconductor. In 2003 Fukuoka *et al.* [46] found that for Na free, Ba-containing silicon clathrates $Ba_{8-x}Si_{46}$ ($0 < x \leq 1.4$) prepared under high pressure and high temperature conditions (3 GPa, 1300 °C), the superconducting transition temperature ranges from 9.0 to 6.0 K. The variation was due to a decrease of Ba content in the samples. It was observed that after annealing the Ba content decreased from 7.76 to 6.63 per cell, which resulted in a lower superconducting transition temperature. The change of Ba content was observed only on the $2a$ sites while the $6d$ sites remained unchanged. The reason for this Ba deficiency on the $2a$ site is not fully understood but it is thought that it is due to the size of the small cage which appears to be too small for the Ba atomic radius. From electronic calculations [47, 44] it was found that the difference in the critical temperature between $Na_{2.9}Ba_{4.5}Si_{46}$ and $Ba_{7.76}Si_{46}$ is the result of a strong hybridization between the $5d$ Ba and Si_{46} states which resulted in a sharp narrow band near the Fermi level. The Na atoms cannot form such hybridization, and they appear to be ions electronically isolated from the Si_{46} framework.

Magnetic properties have been obtained in clathrates by two different methods: The first one is by substituting early transition metals into the framework. Two examples of this kind are: type-I $Ba_8Mn_xGe_{46-x}$ for $1 \leq x \leq 2$ [48] and chiral $Ba_6Fe_3Ge_{22}$ [49]. These materials are difficult to prepare. In the case of type-I $Ba_8Mn_xGe_{46-x}$ it exhibits a ferromagnetic transition at about 10 K. The Mn atoms occupied the 6*c* sites preferentially according to X-ray diffraction and Rietveld refinements. Spontaneous magnetization increases approximately linearly as the number of Mn increases, with a maximum for $Ba_8Mn_2Ge_{44}$. Mn cannot be substituted for $x \geq 2$ due to structure instability. For $Ba_6Fe_3Ge_{22}$, 3 Fe are substituted from the chiral clathrate Ba_8Ge_{25}, by rf induction and arc melting the samples several times to eliminate other phases. This material has a ferromagnetic transition at 170 K. The second way to produce magnetic clathrates is by substitution of magnetic ions inside the cages. The most common is partial or full substitution of Eu. A few examples are: $\alpha-Eu_8Ga_{16}Ge_{30}$ and $\beta-Eu_8Ga_{16}Ge_{30}$, which show a structural dimorphism similar to $Ba_8Ga_{16}Sn_{30}$. In the case of $\beta-Eu_8Ga_{16}Ge_{30}$ the Eu atoms can tunnel between four different sites separated by 0.55 Å inside the large cages [45]. The highest ferromagnetic transition temperature in a Eu-containing clathrate of $T_c = 38$ K corresponds to $Eu_2Ba_6Ga_8Si_{36}$.

C. *Ab − initio* Calculations on Clathrates

Different *ab − initio* calculations have been performed to try to explain the properties of clathrates. Some studies show that the change in superconducting temperature correlates very well with the electron density of states near the Fermi level. For example Tse *et al.* [50] in a study of $Ba_8Ag_nSi_{46-n}$ (n =0, 1, 3, and 6) where Ag occupies the 6*c* sites, showed that the density of states is affected most strongly near the Fermi level as the number of Ag increases from 0 to 6, reducing its den-

sity of states from a sharp peak to a weak shoulder. This feature is also observed in the respective photoelectron spectrum [51], and the superconductivity transition temperature is changed from T_c=8 K for Ba_8Si_{46} to zero for $Ba_8Ag_6Si_{40}$. These results support the BCS theory that the DOS at the Fermi level is the dominant factor responsible for the high superconducting transition temperature of Ba_8Si_{46}. Also the Raman spectra were compared with theoretical calculations giving good agreement. Li *et al.* [52] with a joint experimental and theoretical investigation corroborated this behavior for $Ba_8Ga_xSi_{46-x}$ (x =6, 10, 16). The substitution of Ga leads to a decrease of the density of states at the Fermi level, a lowering of carrier concentration, and a breaking of the integrity of the sp^3-hybridized networks.

First principles calculated thermal properties like specific heat and the thermal expansion coefficient can also be compared with experiment. In the paper by Qiu *et al.* [53] a comparison in the range 35-310 K between specific heat data and a theoretical model for Na_8Si_{46} revealed a extremely good match. This result helped in the assignment of the vibrational spectrum of Na_8Si_{46} providing strong evidence for low-frequency librational modes associated with motions of the guests in the cages resulting in enhanced low-temperature anharmonicity. The lattice parameter as a function of temperature was also compared, giving a reasonable fit.

Another important aspect to understand is the electron effective mass. This parameter can enhance the figure of merit which can be expressed as $Z \propto m^{*3/2}\mu/\kappa_L$, where m^* is the effective mass, μ the mobility and κ_L the lattice thermal conductivity. Assuming that the main scattering mechanism is alloy disorder for SrGaGe clathrates, Fujita *et al.* [54], estimated that the room temperature effective mass is 3.1 m_e which is consistent with the DOS obtained by bandstructure calculations. The number of states they obtained was 8 $\times 10^{20}$ cm^{-3}, which corresponds almost exactly to the carrier concentration in their samples. Also the Seebeck coefficient for this effective

mass compares quite well with the experimental data.

In 2003 Madsen *et al.* [55] estimated by theoretical modeling a dimensionless figure of merit of 1.2 at 400 K for an optimally $p-$doped gallium-germanium framework type$-$VIII europium clathrate. Using a virtual crystal approximation in a relaxed structure for an undoped material, clathrates containing Sr, Ba, and Eu with type-I and type-VIII structures were found to be semiconductors with bandgaps around 0.6-0.9 eV. The conduction bands hybridize with the unoccupied d states of the guest atoms. This means that the thermoelectric properties of $n-$doped type-I clathrates depend strongly on the guest atom while $p-$doped clathrates are relatively unaffected.

In a recent paper, Nenghabi *et al.* [56] found that $Ba_8Al_{16}Si_{30}$ is an indirect band narrow gap semiconductor and is energetically more stable than the Ge counterpart $Ba_8Al_{16}Ge_{30}$ which is a direct band gap semiconductor. In an analysis of the formation energy of both clathrates, the calculated energies were found to be lower than the isolated bulk constituents. Thus they are energetically favorable to form. By doing a vibrational properties analysis they found that the low frequency modes of the Ba rattler lie below 50 cm^{-1}. By comparing the vibrational density of states there is an up-shift of 100 cm^{-1} in the vibrational spectrum for $Ba_8Al_{16}Ge_{30}$ with respect to $Ba_8Al_{16}Si_{30}$ due to the shorter and stronger Si-Si bonds.

D. Clathrates Figure of Merit

Regarding experimental issues the largest dimensionless figure of merit found in this type of compound is 1.35 at 900 K for $Ba_8Ga_{16}Ge_{30}$ grown by Czochralski method [35]. This is a large value, making the material a promising candidate for medium and high temperature thermoelectric applications. However in their 46-mm-long crystal, cut into disks, this value was found in only one of the 18 disks. The molar ratio

Ga/Ge has been identified as a key parameter for explaining the large variability in thermoelectric properties, and the Seebeck coefficient is affected by a small change in the composition. Recent theoretical [55] end experimental [57] investigations suggest that p-type $Ba_8Ga_{16}Ge_{30}$ may have a larger figure of merit than the n-type.

In a recent study of type-VIII single-crystals $Ba_8Ga_{16-x}Al_xSn_{30}$ ($0 \leq x \leq 12$) [58] grown by Sn flux a large figure of merit was also obtained. In the case of $Ba_8Ga_{10}Al_6Sn_{30}$ ZT =1.2 was obtained at 500 K. In these samples the carrier density hardly changes with the substitution of Al. Therefore it is hoped that chemical modifications, doping, and better crystal growth can make clathrate materials commercially useful.

CHAPTER III

EXPERIMENTAL METHODS

For my dissertation work several experimental techniques and methods were used to develop and characterize semiconducting clathrate materials. I used an arc melting system and solid state reaction for sample preparation. Powder x-ray diffraction (XRD) measurements were carried out on a Bruker D8 system for structure determination. A Quantum Design Physical Property Measurement System (PPMS) was employed for resistivity, Seebeck coefficient, and thermal conductivity measurements as a function of temperature. Nuclear magnetic resonance (NMR) measurements were performed on a home built spectrometer [59] to probe for electron local environment around the nucleus, dynamics and interactions. Wavelength dispersion spectroscopy (WDS) were done in a Cameca SX50 equipped with 4 wavelength-dispersive X-ray spectrometers for phases determination and elemental compound composition. Quantum Design Magnetic Property Measuring System (MPMS) semiconducting quantum interference device (SQUID) magnetometer was used for measurement of magnetic properties.

Ba-Al-Ge samples for the first study were prepared by Dr. Weiping Gou, while all the rest of the samples described here were prepared by me. NMR measurement were taken either by Dr. Weiping Gou or Xiang Zheng. All XRD measurements were done by me. I highly appreciate the help received in PPMS measurements from Dr. K. D. D. Rathnayaka and Dr. KyongWan Kim in sample mounting, electrical and thermal properties measurements. WDS measurements were performed by Laziz Saribaev, while I analyzed the obtained results. In addition I performed all of the calculations described in the next chapter.

In this chapter a brief description of each of the experimental methods and

apparatus used is given.

A. Sample Preparation

An arc melting technique was used for sample preparation. In this technique an arc was created between a tungsten tip and a water cooled copper crucible when a difference in voltage is applied. The chamber was filled with argon because it is easy to ionize, the flow of electrons becomes relatively effortless, and oxidation is avoided.

All samples were prepared by first mixing the pure elements by such an arc melting process. Stoichiometric compositions of elements were melted several times to ensure homogeneous composition. After the arc melting process samples were placed in sealed quartz tubes under vacuum for further annealing. The annealing process often required typically 100 hours at a high temperature; the annealing temperature depends on the phase diagram of each compound.

Since Ba reacts readily with air, oxidation of this element is an important concern. To avoid oxidation, Ba was cut in a nitrogen glove box. When transporting to the arc melting system the least contact with the environment is the best, therefore I tried to make the process as fast as possible.

B. XRD

To confirm structure of the compounds powder X-ray diffraction was performed on a Bruker D8 X-ray powder diffractometer. In this technique X-rays are diffracted by the sample into specific directions. These diffracted beams follow Bragg's law, which is $n\lambda = 2d \sin\theta$. From the angles and intensities in the diffracted pattern a 3 dimensional mapping of the structure can be generated.

In this technique the sample was powdered into fine grains to ensure that the

crystal orientation covers all angles. X-ray diffraction using copper K_α radiation was used to determine the crystal structure. For peak search, the EVA program by Bruker was used. Rietveld refinement was done using the EXPGUI package [60].

C. NMR

In nuclear magnetic resonance (NMR) measurement the sample is placed in a high magnetic field, at which point the nuclear spins exhibit a small net alignment pointing along the direction of the applied field. After the equilibrium magnetization is obtained, the equilibrium can be broken by an external rf magnetic signal. In this way information about spin dynamics, interactions, chemical bonding, local environments, etc. can be obtained.

D. PPMS Measurements

The Quantum Design PPMS provides precise temperature and magnetic field control. The temperature range is from 1.9 K to 400 K, while the magnetic field can be adjusted from 0 T to 9 T. The system provides a variety of automated measurements, among them thermal and electronic transport properties, heat capacity and magnetometry.

Resistivity measurements were done using a standard four point probe method. A current is passed by the outer contacts and the resulting longitudinal voltage difference is measured in the inner contacts. In this way the resistivity is determined as a function of temperature. In all samples silver print with 2 μm gold wires was used as contacts.

Thermal conductivity is obtained by applying heat to one end of the sample with a heat sink on the opposite end. Two thermometers are placed between the

heat source and heat sink so the gradient in temperature could be measured between them.

To measure the Seebeck coefficient the same configuration is used, but in this case a specific temperature drop between the thermometers is used. For these measurements the voltage drop created between the thermometer contacts is also monitored. With the three quantities described above (resistivity, thermal conductivity, and Seebeck coefficient) the dimensionless thermoelectric figure of merit can be easily calculated.

E. Electron Micro-probe

Electron micro-probe analysis is a non-invasive method that provides fundamental compositional information of solid materials in spot sizes as small as a few micrometers. It uses a high-energy focused beam of electrons to generate X-rays characteristic of the elements. Chemical composition is determined by comparing the intensity of X-rays from standards with those from unknown materials and correcting for the effects of absorption and fluorescence in the sample.

Such a micro-probe instrument includes a scanning electron microscope, electron probe X-ray micro-analyzer (WDS and EDS spectrometers), BSE detector, and optical microscope. Among these techniques, for this project we used only WDS. WDS measurements were performed in a Cameca SX50 equipped with 4 wavelength-dispersive X-ray spectrometers, a PGT energy-dispersive X-ray system and cathodoluminescence detector. Samples were the same as the ones used for XRD experiments, fined grained powders. These grains were put into epoxy and then mechanically polished to obtain a flat surface.

F. SQUID Magnetometry

The Quantum Design Magnetic Property Measurement System (MPMS) sample magnetometer was used for magnetization and susceptibility measurements. It provides precise temperature and magnetic field control. The temperature ranges from 1.9 K to 400 K, while the magnetic field can be adjusted from 0 T to 9 T. The system uses a high sensitivity superconducting quantum interference device (SQUID) that provides a variety of automated measurements, among which are AC and DC magnetic susceptibility and magnetic moment.

DC susceptibility measurements were done by inserting the samples into a constant magnetic field, then measuring the magnetic moment of the sample. The moment is measured by induction techniques, performed by moving the sample with respect to a set of pickup coils.

There are two distinct ways to measure magnetization with a SQUID magnetometer. The field cooling (FC) method is to apply the field far above a characteristic temperature T_f and cool the sample in a field to $T \ll T_f$, all the while recording the magnetization. The zero field cooling (ZFC) method is to cool the sample in zero field to $T \ll T_f$, and at this low temperature apply the field. After this one heats the sample while measuring M up to $T \gg T_f$ with the field constant. An observed difference between ZFC and FC magnetization indicates that the free energy has a complicated many valley structure below T_f. A remenant magnetic field of less than 3 mOe is the key to the precise measurement of FC and ZFC magnetization.

CHAPTER IV

THEORETICAL METHODS

In recent times numerical modeling has become one important tool in the development of new materials. With the advent of computers this numerical work has become faster and easier. A lot of problems are solved using first principle calculations. Utilizing density functional theory (DFT) the many-body problem of interacting electrons is mapped onto a one electron reference that leads in principle to the same density as the real system [61]. In DFT, exchange and correlation terms are included but they are treated approximately. Some specific approximations are the local density approximation (LDA) and generalized gradient approximation (GGA) [62]. Both of these have shown to be reliable and useful tools in many applications. These techniques have been widely used with good results in periodic systems. In addition, they have been shown to be trustable in real materials that show defects, grain boundaries, dislocations, vacancies, etc.

Nowadays there are two most common ways of solving the Schrödinger equation for interacting electrons using DFT. One method uses pseudopotentials with relatively simple basis sets, while the other uses complex basis sets such as the Linear Augmented Plane Wave Method (LAPW) [63]. The latter will be discussed here. In this case the planewaves are adjusted near the atoms instead of the Hamiltonian to simulate the rapid variations in the valence wavefunctions.

A. Density Functional Theory

DFT theory was developed by Hohenberg and Kohn [64]. Their theorem states that the total energy can be described as a functional of the ground state electronic

density, ρ:

$$E = E[\rho].$$

In this case the corresponding Hamiltonian has the general form

$$E[\rho] = T_s[\rho] + E_{ei}[\rho] + E_{ii}[\rho] + E_H[\rho] + E_{xc}[\rho]. \tag{4.1}$$

Here $T_s[\rho]$ denotes the single particle kinetic energy, $E_{ei}[\rho]$ is the Coulomb interaction energy between electrons and the nuclei, $E_{ii}[\rho]$ is the interaction of the nuclei with each other, and $E_H[\rho]$ is the Hartree component of the electron-electron energy,

$$E_H[\rho] = \frac{e^2}{2} \int d^3\vec{r} d^3\vec{r}' \frac{\rho(\vec{r})\rho(\vec{r}')}{|\vec{r} - \vec{r}'|}.$$

In the LDA[61], $E_{xc}[\rho]$ is written as

$$E_{xc}[\rho] = \int d^3\vec{r} \rho(\vec{r}) \epsilon(\rho(\vec{r})),$$

where $\epsilon(\rho)$ is approximated by a local function of the density. In the GGA, the local gradient is used together with the local density to incorporate more information about the electron gas, so then $\epsilon(\rho)$ is replaced by $\epsilon(\rho, |\nabla\rho|)$.

To solve Eq. (4.1) several methods have been implemented. The LAPW method is a modification of the augmented planewave method (APW) which was developed by Slater in 1937 [65]. Therefore the APW method will be explained first and then I will focus on the LAPW method. To solve the Schrödinger equation for materials the space is divided into two regions. One of these corresponds to spherical volumes close to the nuclei, where the potential and wavefunctions are similar to those inside an atom. This space is denoted by S, and is called the "core region". The other region is the interstitial space or "valence region"which is involved in atom binding, and denoted by I. In the APW approximation the strong core potential is replaced

by a pseudopotential, whose ground state wavefunction φ^{PS} mimics the all electron valence wavefunction outside a selected core radius. In this case the solutions to Schrödinger's equation are planewaves outside the sphere and radial solutions inside the sphere:

$$\varphi(\vec{r}) = \begin{cases} \Omega^{-1/2} \sum_{\mathbf{G}} c_{\mathbf{G}} e^{i(\mathbf{G}+\mathbf{k})\cdot\mathbf{r}} & \mathbf{r} \in I \\ \sum_{lm} A_{lm} u_l(r) Y_{lm}(\hat{\mathbf{r}}) & \mathbf{r} \in S \end{cases}$$

where φ is a wavefunction, Ω is the cell volume, and u_l is the regular solution of

$$\left[-\frac{d^2}{dr^2} + \frac{l(l+1)}{r^2} + V_l(r) - E_l \right] r u_l(r) = 0.$$

Here, $c_{\mathbf{G}}$ and A_{lm} are expansion coefficients, E_l is an energy parameter, V_l is the spherical component of the potential in the sphere, and

$$A_{lm} = \frac{4\pi i^l}{\Omega^{1/2} u_l(R)} \sum_{\mathbf{G}} c_{\mathbf{G}} j_l(|\mathbf{k}+\mathbf{G}|R) Y_{lm}^*(\mathbf{k}+\mathbf{G}).$$

A few problems are encountered with the APW method; the main drawback is that the basis set is dependent on the energy parameter, thus a different energy-dependent set of APW basis functions must be found for each eigenenergy. Another problem is the term $u_l(r)$ appearing in the above equation. This quantity vanishes on the sphere boundary for general values of the energy parameter E_l, and then the planewaves and the radial wavefunctions become decoupled. To solve the energy dependence of the basis set several methods were developed. A flexible and accurate approach is the LAPW method which uses linear combination of $u_l(r)Y_{lm}(\hat{\mathbf{r}})$ and their energy derivatives with respect to the linearization parameters, E_l:

$$\varphi(\vec{r}) = \begin{cases} \Omega^{-1/2} \sum_{\mathbf{G}} c_{\mathbf{G}} e^{i(\mathbf{G}+\mathbf{k})\cdot\mathbf{r}} & \mathbf{r} \in I \\ \sum_{lm} \left[A_{lm} u_l(r) + B_{lm} \dot{u}_l(r) \right] Y_{lm}(\hat{\mathbf{r}}) & \mathbf{r} \in S. \end{cases}$$

The energy derivative, $\dot{u}_l(r)Y_{lm}(\hat{\mathbf{r}})$ satisfies

$$\left[-\frac{d^2}{dr^2}+\frac{l(l+1)}{r^2}+V_l(r)-E_l\right]r\dot{u}_l(r)=ru_l(r).$$

Then we just need a single diagonalization to obtain all the eigenenergies in contrast to APW.

In the LAPW method there are three different categories for the electronic states: core, semi-core and valence states. The core states are completely confined inside the spheres. They are treated in an atomic fully relativistic fashion as thawed core. The valence states are partly delocalized and obtained with the LAPW method. Finally the semi-core states need special attention because they are high lying core states with a principal quantum number one less than the valence states. Singh [66] treated these states with local orbitals (LOs). A LO is constructed by the LAPW radial functions u and $\dot{u}$ at one energy $E_{1,l}$ in the valence band region and a third radial function $E_{2,l}$:

$$\varphi_{LO}(\vec{r})=\begin{cases}0 & \mathbf{r}\,\epsilon\, I\\ \left[A_{lm}u_l(r,E_{1,l})+B_{lm}\dot{u}_l(r,E_{1,l})+C_{lm}u_l(r,E_{2,l})\right]Y_{lm}(\hat{\mathbf{r}}) & \mathbf{r}\,\epsilon\, S.\end{cases}$$

The three coefficients are determined by the normalization and the requirement that the LO should have zero value and slope at the sphere boundary. These local orbitals are added in the case when a single choice of energy E_l is not adequate to describe all the bands that must be considered (*e.g.* the $5p$ state in the $4f$ elements).

B. WIEN2k and NMR Lineshape Simulations

Ab-initio calculations were carried out using the full-potential linearized augmented plane-wave (FP-LAPW) method as implemented in the WIEN2k package [67]. This code started to develop in the late 80s. Many different properties can be

calculated using this program such as density of states, bandstructures, electron and spin densities [55], structure factors which can be compared with x-ray diffraction experiments [68], total energies, forces, equilibrium geometries, optimized structures, molecular dynamics [10], phonons from which vibrational properties can be obtained [11], optical properties [12], Fermi surfaces [13], and electric field gradients (EFG's) [69]. The EFG is a quantity related to the ground state density that is sensitive to the anisotropy of the charge density close to the nucleus and can be measured by nuclear quadrupole interactions.

In all cases we used the Generalized Gradient Approximation (GGA), with the Perdew-Burke-Ernzerhof (PBE) formalism for the exchange-correlation term. I obtained EFG's for different sites from the calculated all-electron charge distribution, using a method used in recent years with considerable success for analysis of NMR spectra [70, 71]. Relations for NMR transition frequencies between the m^{th} and $(m+1)^{\text{th}}$ levels in a single crystal are well established [72], with quadrupole shifts given in terms of the EFG principal values ($\frac{\partial^2 V}{\partial x^2}$, $\frac{\partial^2 V}{\partial y^2}$, $\frac{\partial^2 V}{\partial z^2}$), $\eta = (\frac{\partial^2 V}{\partial x^2} - \frac{\partial^2 V}{\partial y^2})/\frac{\partial^2 V}{\partial z^2}$, and $\nu_Q = \frac{3e^2qQ}{2I(2I-1)h}$, with $eq = \frac{\partial^2 V}{\partial z^2}$ the largest principal value and Q the nuclear quadrupole moment. From computed EFG matrix elements the quadrupole lineshape was simulated by summing a contribution from each m to $m+1$ transition, with a weighting factor $\sqrt{(I+m)(I-m+1)}$ for each m, and using standard expressions for the angular dependence [72]. The results were used to calculate the powder patterns numerically, by summing uniformly over all solid angles. The quadrupole contributions to the NMR can be treated with perturbation theory, for all cases I considered first and second-order quadrupole shift for each transition [73]. In some cases an anisotropic chemical shift was also included in the angular summation, although this did not provide apparent improvement and hence was not used in any of the final simulations.

C. Quantum Theory of Atoms In Molecules

The Quantum Theory of Atoms In Molecules (QTAIM) was developed in the early 1960s by Richard Bader [74]. It relies on the idea that the bonding of atoms can be analyzed from the topology of the quantum electron density. To determine the physics of this electron density one needs to consider the field it produces by tracing out the trajectories of the vector gradient of the density. The density exhibits a maximum at the position of each nucleus, so these trajectories end at each nucleus. The nuclei are called the attractors. The space within the molecule or solid is disjointly and exhaustively partitioned into basins, a basin being the region of space traversed by the trajectories terminating at a given nucleus or attractor. Since a single attractor is associated with each basin, an atom is defined as the union of an attractor and its basin. A critical point denotes an extremum in $\rho(\vec{r})$, a point where $\nabla\rho(\vec{r}) = 0$. With each critical point there are an associated set of trajectories that start at infinity and end at a critical point. These define an interatomic surface that separates the basins of neighboring atoms. There is a unique pair of trajectories that originates at each such critical point and terminates, one each, at the neighboring nuclei. They define a curve through space along which the electron density is a maximum. The two sets of trajectories associated with such a critical point, are called bond critical point. Two atoms are considered to be bonded if their atomic volumes share a common interatomic surface, and there is a (3,-1) critical point on this surface. A (3,-1) point is defined as a point were two values of the Hessian matrix at the critical are negative, meanwhile the third one is positive (i.e. a saddle point). The bonds are classified as closed shell or open shell, if the Laplacian of the electron density at the critical point is positive or negative, respectively.

D. Transport Properties Calculations

Several properties can be calculated from energy bands and their derivatives. Using Boltzmann transport theory [75] these properties can be calculated. In the presence of an electric and magnetic field and a thermal gradient, the electrical current can be written as

$$j_i = \sigma_{ij} E_j + \sigma_{ijk} E_j B_k + v_{ij} \nabla_j T + \dots . \tag{4.2}$$

In terms of the group velocity,

$$v_\alpha(i,\vec{k}) = \frac{1}{\hbar}\frac{\partial \varepsilon_{i,\vec{k}}}{\partial k_\alpha}, \tag{4.3}$$

and the inverse mass tensor,

$$M^{-1}_{\beta u}(i,\vec{k}) = \frac{1}{\hbar^2}\frac{\partial^2 \varepsilon_{i,\vec{k}}}{\partial k_\beta \partial k_u}, \tag{4.4}$$

the conductivity tensor is given by

$$\sigma_{\alpha,\beta}(i,\vec{k}) = e^2 \tau_{i,\vec{k}} v_\alpha(i,\vec{k}) v_\beta(i,\vec{k}). \tag{4.5}$$

All these quantities depend on the relaxation time τ. In the present cases we will use the simplest approximation, keeping it constant.

The transport tensors can be calculated from the conductivity distributions

$$\sigma_{\alpha\beta}(T;\mu) = \frac{1}{\Omega}\int \sigma_{\alpha\beta}(\varepsilon)\left(-\frac{\partial f_\mu(T;\varepsilon)}{\partial \varepsilon}\right) d\varepsilon \tag{4.6}$$

$$\nu_{\alpha\beta}(T;\mu) = \frac{1}{eT\Omega}\int \sigma_{\alpha\beta}(\varepsilon)(\varepsilon-\mu)\left(-\frac{\partial f_\mu(T;\varepsilon)}{\partial \varepsilon}\right) d\varepsilon \tag{4.7}$$

$$\kappa^0_{\alpha\beta}(T;\mu) = \frac{1}{e^2T\Omega}\int \sigma_{\alpha\beta}(\varepsilon)(\varepsilon-\mu)^2\left(-\frac{\partial f_\mu(T;\varepsilon)}{\partial \varepsilon}\right) d\varepsilon \tag{4.8}$$

where f_μ is the Fermi function, κ^0 is the electronic part of the thermal conductivity.

The Seebeck coefficient can be calculated as

$$S_{ij} = E_i(\nabla_j T)^{-1} = (\sigma^{-1})_{\alpha i} v_{\alpha,j}. \tag{4.9}$$

By assuming a rigid band model to adjust the Fermi level, the calculated Seebeck coefficient (Eq. (4.9)) can be compared with the experimental measurement.

CHAPTER V

RESULTS AND DISCUSSIONS

A. Fe-Al-Zn Materials

1. Magnetic and Vibrational Behavior in Fe_4Al_{11-y} and $Fe_4Al_{10-x}Zn_x$ Materials.[1]

Al-rich Fe aluminides, along with other transition-metal aluminides, form complex atomic structures. These compounds show a variety of different magnetic properties. In the case of $FeAl_2$ the material shows a concentrated-moment behavior [76], while FeAl is a nonmagnetic ordered intermetallic. Intermediate behavior is observed in Fe_2Al_5, where dilute moments are present and attributed plausibly to wrong site Fe occupation [77]. Recently this material also showed anomalous vibrational properties [77] manifested in the specific heat at low temperatures. At low temperatures a linear behavior typical of metals is identified, however this is replaced by a downturn below 20 K. By analysis of the specific heat it was concluded that the low-energy excitations are due to a set of localized anharmonic vibrations, attributed to the atomic motions of the partially occupied chains [77].

---

[1]Part of this chapter is reprinted with permission from "Dilute magnetism and vibrational entropy in Fe_2Al_5" by Ji Chi, Xiang Zheng, Sergio Y. Rodriguez, Yang Li, Weiping Gou, V. Goruganti, K. D. D. Rathnayaka, and Joseph H. Ross, Jr., 2011, Physical Review B v. 82, p. 174419, ©(2010) American Physical Society.

Part of this chapter is reprinted with permission from "NMR and computational studies of $Ba_8Ga_{16}Sn_{30}$ clathrates" by Sergio Y. Rodriguez, Xiang Zheng and Joseph H. Ross, Jr., 2011. Mater. Res. Soc. Symp. Proc., v. 1267, p. DD04-07, ©(2010) Materials Research Society.

Part of this chapter is reprinted with permission from "NMR experiments and electronic structure calculations in type-I BaAlGe clathrates" by Weiping Gou, Sergio Y. Rodriguez, Yang Li, and Joseph H. Ross, Jr., 2009. Physical Review B vol 80, page 144108, ©(2009) American Physical Society.

Part of this chapter is reprinted with permission from "Zintl behavior and vacancy formation in type-I Ba-Al-Ge clathrates" by Sergio Y. Rodriguez, Laziz Saribaev, and Joseph H. Ross, Jr., 2010. Physical Review B vol 82, page 064111, ©(2010) American Physical Society.

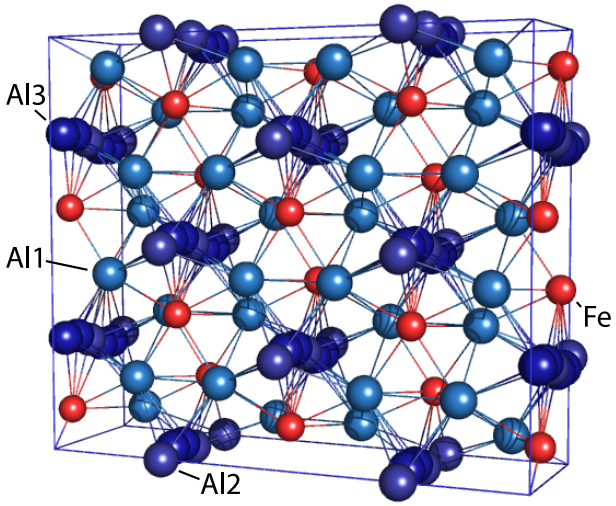

Fig. 5. Fe_2Al_5 orthorhombic structure, with a $2 \times 2 \times 1$ superstructure. Larger spheres denote Al, and smaller spheres Fe, as labeled. Undulating chains of overlapping Al(2) and Al(3) sites are shown here as if completely occupied. Zn occupy the Al(2) and Al(3) sites. Reprinted figure with permission from [77] © (2010) by the American Physical Society.

For this study a combination of both theoretical and experimental results were obtained for $Fe_4Al_{11-x}Zn_x$ materials with $0 \leq x \leq 1$ and Fe_4Al_{11-y} with $0 \leq y \leq 3$. These materials were considered in order to understand the magnetic and vibration properties. Fe_2Al_5 includes closely-spaced Al sites in the channels, and hopping between these sites can have a large effect on the vibrational behavior. Also, I considered cases with Zn substitution to study the effect of Zn in the materials behavior. All of these materials have the same structure as Fe_2Al_5. $Fe_4Al_{11-x}Zn_x$ is a quasicrystal approximant with pentagonal channels through which are threaded one-dimensional arrays of partially occupied aluminum sites spaced very closely. These materials have an orthorhombic structure ($Cmcm$, space group #63) as shown in Fig. 5. To study the structural, vibrational and magnetic behavior of these materials we measured NMR lineshapes, coupled with first principles calculations.

a. Sample Preparation

Samples for this study were prepared by me, except that Fe_4Al_{10} was prepared by Ji Chi. Stoichiometric compositions of pure elements were mixed by arc melting. The resulting polycrystalline ingots were annealed in vacuum-sealed quartz tubes at 600 °C for one week.

b. Experiment

XRD measurements were performed on a Bruker D8 X-ray Powder Diffractometer using Cu K_α radiation. Structural refinement of X-ray data was carried out using the GSAS software package [60]. NMR experiments were performed by Ji Chi and Xiang Zheng using a pulse spectrometer [59] from 4.2 to 450 K at two fixed fields. Susceptibility and magnetization measurements were performed using a Quantum Design MPMS SQUID magnetometer.

Due to fluorescence of Fe from Cu K_α radiation a broad background was added in the Rietveld refinements, since there was not any other X-ray source available. We used these data only to confirm that the materials have the correct structure. For the $Fe_4Al_{10.5}Zn_{0.5}$ sample there is only one phase. In this structure there are three different Al sites. Al(1) sites (8/cell) are fully occupied while the overlapping sites Al(2) (4/cell) and Al(3) (8/cell) make up disordered chains as shown in Fig. 5.

For Fe_2Al_5 the room temperature ^{27}Al NMR spectrum has a two peaked structure (shown in Fig.6), while at low temperatures the signal becomes broader due to the presence of paramagnetic moments. The pulse-length behavior confirmed the central portions of these lines to be central transitions for ^{27}Al(I=5/2) connecting -1/2 $\leftrightarrow$ +1/2 states. From a previous Magic Angle Spinning-NMR measurement it was deduced that the two peaked structure corresponded to a single site rather than

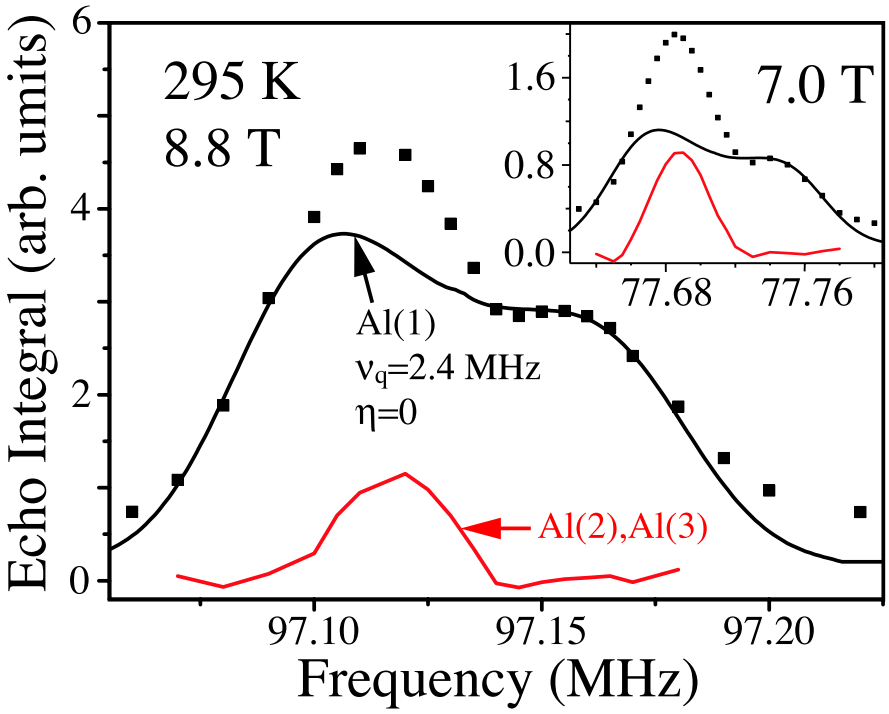

Fig. 6. NMR lineshape simulations for Fe_2Al_5 at two constants fields. Reprinted figure with permission from [77] © (2010) by the American Physical Society.

splitting due to two inequivalent sites. Eight of the ten Al atoms per cell belong to the Al(1) site, so we can deduce that the main contribution is related to this site. From the two different constant field measurements the magnetic and quadrupole contributions could be separated, since the magnetic shift is proportional to B and the second order quadrupole is inversely proportional to B [72]. From fitting of the spectral center of mass for 295 K data at the two constant fields we extracted a magnetic shift of $K = +0.020(1)\%$ and a second order quadrupole of $\nu_Q = 1.9$ MHz with $\eta = 0$.

In numerical NMR lineshape simulations starting with the experimental values for $\nu_Q = 1.9$ MHz and $\eta = 0$, I found that the main features of the spectra could be fitted consistently vs. field only by using a larger ν_Q than obtained from the center of mass values, with $\eta \approx 0$ and $K = +0.025\%$. Fig. 6 shows the superposition of such

a single-site quadrupole spectrum with ν_Q=2.39 MHz for two different fields. The results are relatively insensitive to the parameter η, however we found that computed curves for $\eta \geq 0.3$ agreed poorly with the data. With this plot superposed, we find in addition a second peak, as shown from the difference curves plotted in Fig. 6. This additional peak makes up $12 - 22\%$ of the total spectral weight. The difference in magnitude between the two fields may be an artifact of the fitting. According to the measured site occupations, 20% the Al reside on the two channel sites, so it is reasonable to conclude that the additional peak corresponds to these sites while the fitted $\nu_Q = 2.39$ MHz resonance is attributed to Al(1). These results placed NMR analysis on a firm footing, which allows the magnetic shift to be well established. This result, in turn, allowed us to clarify the vibrational nature of the low temperature anomaly. We therefore determined to study substituted alloy in order to further clarify the role of the chain atoms in these anomalies.

c. Computational Results and Discussion

Spin polarized calculations were performed with the FP-LAPW method using the WIEN2k code [67]. All structures were minimized in volume and internal structural parameters. In order to address the magnetization of wrong-site Fe atoms, we included several configurations with Fe on chain sites as well as with varying occupation of the partially filled Al(2) and Al(3) sites. This procedure also allowed us to address the possible presence of narrow features in the density of states near the Fermi level [78, 79, 80], as found in some quasicrystals and approximants. Therefore we examined the behavior of several distinct configurations of Fe_4Al_{11-x} with $0 \leq x \leq 3$ and $Fe_4Al_{11-y}Zn_y$ with $0.5 \leq y \leq 1$.

In Table II the eight structures considered are listed. These superstructures were constructed starting with the parent Fe_2Al_5 configuration, for which the experimen-

Table II. Site occupations from type-I Rietveld refinements.

Structure	Supercell	Fe in the chain	Magnetic Moment (μ_B)
Fe_4Al_{11}	$1 \times 1 \times 1$	0	1.22
$Fe_4Al_{10.12}$	$1 \times 1 \times 4$	0.25	1.25
Fe_4Al_{10}	$1 \times 1 \times 1$	0	0.13
$Fe_4Al_{9.33}$	$1 \times 1 \times 2$	0.5	3.00
Fe_4Al_9	$1 \times 1 \times 1$	0	3.58
Fe_4Al_8	$1 \times 1 \times 1$	1	2.68
$Fe_4Al_{10}Zn$	$1 \times 1 \times 1$	0	0.00
$Fe_4Al_{10.5}Zn_{0.5}$	$1 \times 1 \times 2$	0.5	2.52

tally observed occupation of the chain sites is 0.36 for Al(2) and 0.23 Al(3), with Al(1) fully occupied [12]. For the first simulation we set the occupation to 0.25 for Al(2) and for Al(3) (thus placing one Al(2) and two Al(3) along the chain in each cell), making a net composition of Fe_4Al_{11}. To obtain this configuration Al was substituted in the chains spaced every fourth site counting along the chains, forming a $1 \times 1 \times 2$ supercell in the original $Cmcm$ (s.g. #63) symmetry. Once substituted the symmetry of the system changes to monoclinic $C2/m$ (s.g. #12). The Fe_4Al_{11} configuration is a "filled-chain" configuration, with Al-Al spacings of 2.82 and 2.84 Å along the chain direction, comparable to with the Al-Al spacing in Al metal, 2.86 Å. However note that Fe_4Al_{11} represents the upper limit of Al occupation, while the nominal composition as typically observed must include larger Al-Al spacings along the chains corresponding to non-bonding links in the chain direction.

Additional configurations considered included correspondingly larger Al-Al spacing along the chains. In the cases of Fe_4Al_{10} and Fe_4Al_9 one and two Al atoms were removed from the filled-chain Fe_4Al_{11} configuration, respectively. To investigate frac-

tional occupation of Fe on chain sites, we also increased the Fe_4Al_{11} superstructure size and substituted some of the Al(2) sites by Fe, for example $Fe_4Al_{9.33}$ representing a $1\times1\times2$ supercell (Fe_8Al_{22}) with one chain site replaced by Fe, giving the composition Fe_9Al_{21}.

In the case of the Zn containing structures, to construct $Fe_4Al_{10}Zn$ we took the parent structure Fe_4Al_{11} and substituted one of the Al(2) sites by Zn. For $Fe_4Al_{10.5}Zn_{0.5}$ I made a $1\times1\times2$ supercell based on Fe_4Al_{11}, and replaced one Al(2) atoms by Fe and one by Zn, giving the composition $Fe_8Al_{21}Zn$.

In Table II the eight different configurations considered are shown together with the supercell size in each case, and the number of Fe-occupied chain sites per formula unit. The last column indicates the computed magnetic moment of each configuration, per formula unit. The first five rows belong to Fe_4Al_{11-y} configurations, and in these cases it is clearly seen that the magnetic moment increases as the number of Fe atoms along the chains increases, changing from 1.22 μ_B for Fe_4Al_{11} with zero Fe along the chains to 3.00 μ_B for $Fe_4Al_{9.33}$ with 0.5 Fe along the chain per f.u. However we find that even without substitution of Fe on the chains, an intrinsic moment can appear in a way that is strongly dependent on the neighbor configuration. Thus it seems that Fe along the chains is not the only thing that affects the magnetic moment. For example, Fe_4Al_{11} only Al are placed along the chains and there is a large magnetic moment similar to the one with 0.25 Fe on the chain. Also in Fe_4Al_9 a relatively high moment is found, as might be expected as the number of Fe-Al neighbors decreases [76]. Consequently it seems that the large moment appears to be tied to neighbor configuration as shown below.

The inclusion of Zn into the chains suppresses the magnetic moment; for example incorporation of 0.5 Zn per unit cell reduces the magnetic moment of $Fe_4Al_{10.5}Zn_{0.5}$ by 0.48 μ_B compared with $Fe_4Al_{9.33}$. A more drastic change occurs when the Fe in

the chains is fully substituted with Zn, in the $Fe_4Al_{10}Zn$ configuration. In this case the magnetic moment completely disappears.

In Fig. 7(a) and Fig. 7(b) the densities of states for spin up and spin down states, respectively, are shown from the spin-dependent calculation per formula unit (f.u.). From the figures it can be observed that there exists a pseudogap at the Fermi level as expected for Hume-Rothery type materials. However, there are also narrow features observed near the Fermi energy which can be correlated with the magnetic moments. In the case of Fe_4Al_{11} the spin majority is for spin up, meanwhile for Fe_4Al_8 the spin down is the majority. On the other hand in Fe_4Al_{10} spin up and spin down states are practically the same. The difference between the number spin up and spin down states in Fe_4Al_{11} is 4.44 states/eV f.u., while for Fe_4Al_8 the difference is 2.34 states/eV f.u., but for Fe_4Al_{10} the difference becomes zero.

In the case of Fe_4Al_{11} the inset of Fig. 7(a) shows the total (non spin-polarized) density of states. While most of the $d-$states are below the Fermi level, a very narrow peak is observed at E_f. For this peak the density of states is strongly dominated by a Fe atom situated on a regular framework site having only one occupied chain Al site within 2.4 Å, whereas the other Fe sites have two such Al neighbors. The calculated moment is also strongly localized on this site. Thus it appears that the observed dilute magnetism includes an intrinsic feature associated with the different local neighbor configurations in addition to the contributions from anti-site configurations where Fe atoms occupy chain sites. The dangling bonds associated with these sharp features at E_f may also contribute to the observed anomalous vibrational features.

In a previous study of specific heat of Fe_2Al_5 an anomalous γ (T-linear term) was observed, with a downturn at low temperatures [77]. Sample-dependent values were observed close to $\gamma = 100$ mJ/mol K^2 (adjusted to formula unit = Fe_4Al_{10}) and this was attributed to anharmonic vibrational modes associated with the disordered

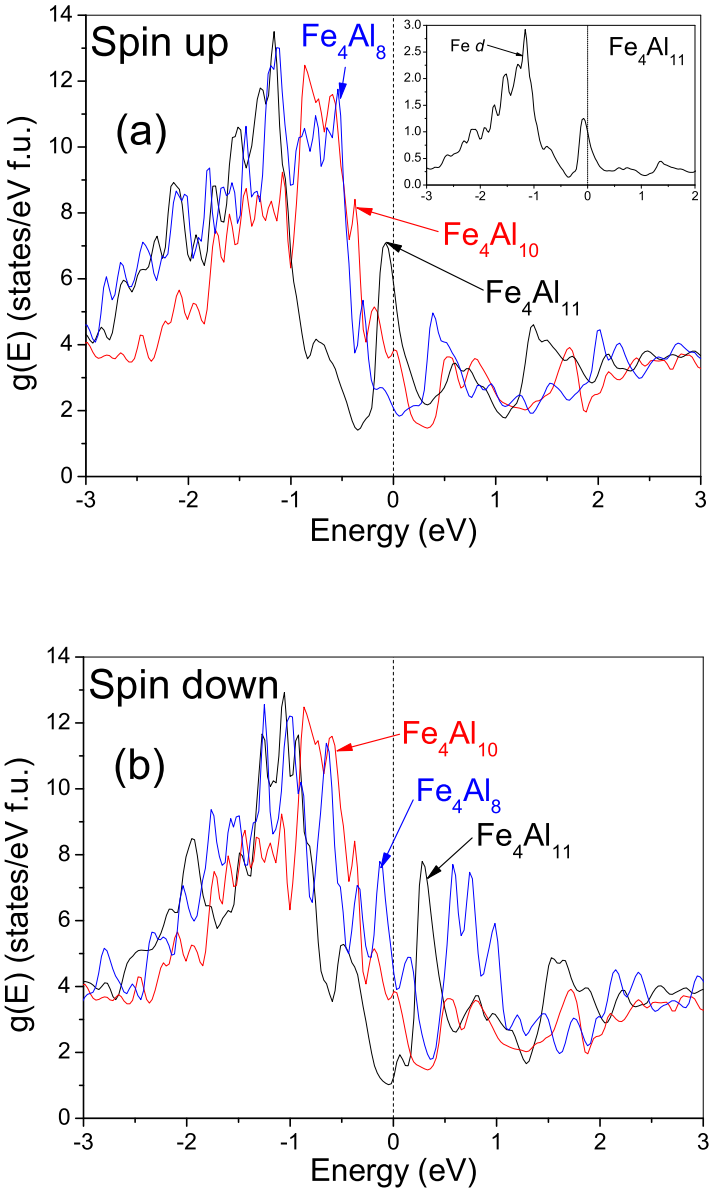

Fig. 7. Density of states for different Fe-Al superstructures, including cases with no Fe antisites along the chains. (a) Spin up states. (b) Spin down states. Inset in (a): Fe partial $d - g(E)$ for Fe_4Al_{11} from a spin-independent calculation.

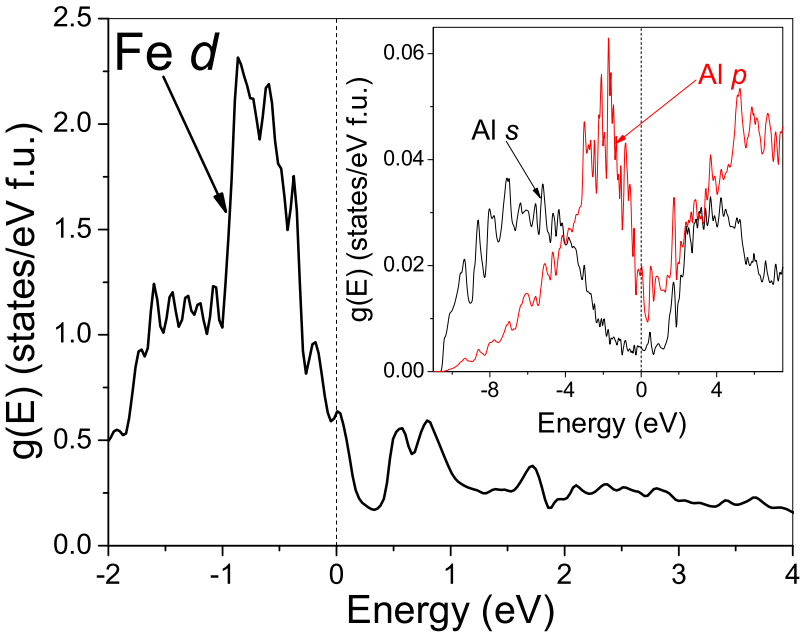

Fig. 8. Fe $d-g(E)$ for the Fe_4Al_{10} superstructure. Inset: Al s and $p-g(E)$ for Fe_4Al_{10}.

structural chains. From the density of states calculated here for Fe_4Al_{10} we obtained a density of states at the Fermi level of 14.1 states/eV f.u.. Using the standard relation for metallic systems, we obtain $\gamma = 8.3$ mJ/mol K^2 for Fe_4Al_{10}. Even with the narrow peak observed in Fe_4Al_{11} (Fig. 8) this value becomes 20 mJ/mol K^2. These values are much smaller than fitted from experimental measurements confirming that the main contribution is not due to electrons, reinforcing the analysis by Chi *et al.* [77].

In Fig. 8 the partial density of states for Fe d states is shown, while in the inset the Al s and p states are shown, for Fe_4Al_{10}. In Fe_4Al_{10} the d states have the largest contribution for Fe sites. There are two inequivalent Fe sites but their contributions are practically the same. Also the density of states is practically the same for all three Al sites. From Fig. 8 the large pseudogap due to strong $sp-d$ hybridization can be clearly seen.

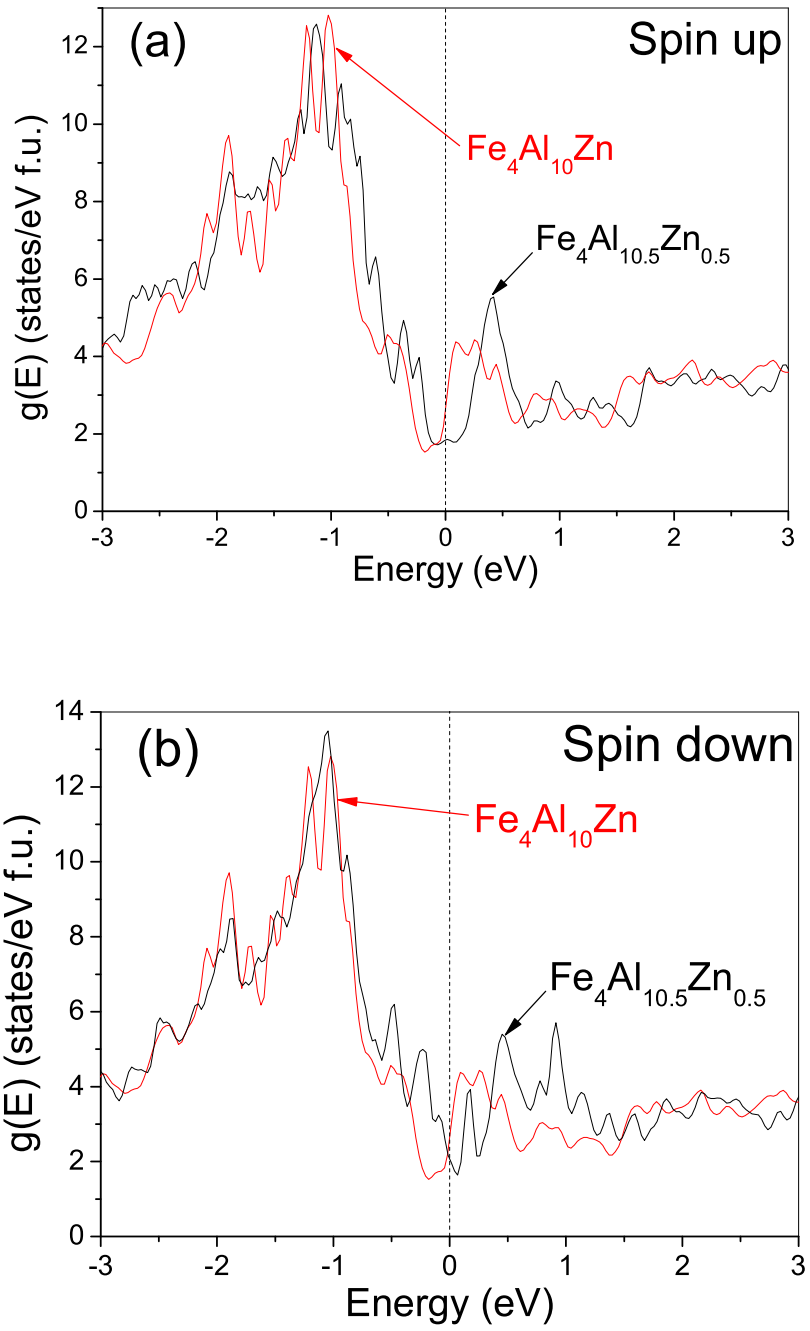

Fig. 9. Density of states for different Fe-Al-Zn superstructures. (a) Spin up states. (b) Spin down states.

In Fig. 9(a) and Fig. 9(b) the densities of states for Zn substituted configurations are shown. In the case of $Fe_4Al_{10}Zn_{0.5}$ the spin down is the majority. The difference between the density of spin up and spin down states for this case is 2.34 states/eV f.u., while for $Fe_4Al_{10}Zn$ the difference is practically zero. From Table II, Fig. 9(a) and Fig. 9(b) it is clearly observed that the replacement of Fe for Zn in the chains leads to a reduction in spin difference leading to a reduction in the magnetic moment. Starting with a partial reduction for $Fe_4Al_{10.5}Zn_{0.5}$, the moment becomes completely suppressed when chain-site Fe is entirely substituted by Zn.

In summary an experimental and computational study in Fe-Al and Fe-Al-Zn was performed to get a better understanding of the magnetic and vibrational properties. NMR lineshapes help to clarify the nature of the low temperature anomaly previously observed in resistivity measurements. *Ab initio* calculations helped in the description of the magnetic properties due to the Fe antisites. From the results it is inferred that Fe along the chains produces a higher magnetic moment but also the neighbor configuration can lead to an enhancement. However full substitution of Zn in the chains suppresses all magnetic behavior.

B. Al-V-La Materials

1. Vibrational Behavior in $Al_{20}V_2La$

Interesting vibrational behavior has been observed in $Al_{10}V$ [81, 82] which is the parent structure for $Al_{20}V_2La$. The intermetallic compound $Al_{10}V$ behaves as an Einstein oscillator and the low temperature resistivity and heat capacity agree well with this model. Caplin [81] showed that $Al_{10}V$ has a local soft mode at $T =$ 22 K that is associated with Al loosely occupying a large cage. In $Al_{10}V$ there are three different Al sites: $96g$ site = Al(1), $48f$=Al(2), and $16c$ =Al(3), one void ($8b$), and one V site($16c$). Sometimes the void is filled by an additional Al, so that the composition range could be extended to $Al_{10.5}V$. In the void we can also substitute La. The corresponding site is centered in an Al Friauf polyhedron [82]. It was found that the diameter of the void is about 3.2 Å, compared with the Al covalent diameter of 2.8 Å[82]. The limiting cases correspond to $Al_{10}V$ and $Al_{10.5}V$, with the void totally empty and fully occupied, respectively.

The $Al_{20}V_2La$ framework of multiply-connected Al atoms is shown in Fig. 10 ($Fd\bar{3}m$ space group #227). Work in our lab on transport and heat capacity measurements in $Al_{20}V_2La$ indicated that the vibrational properties correspond to two Einstein oscillators embedded in a Debye metal [83]. To further understand the weak coupling that exists inside the Friauf polyhedron I performed *ab initio* computational studies.

a. Computational Results and Discussion

First principles calculations were implemented with the FP-LAPW method using the WIEN2k code [67]. All structures were minimized in volume and internal structural parameters. For QTAIM analysis of the resulting electron densities, we

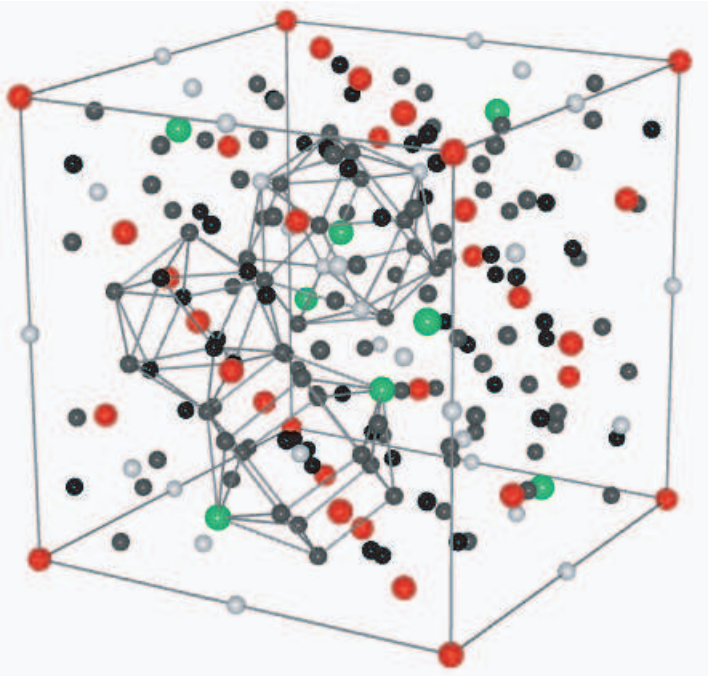

Fig. 10. $Al_{20}V_2La$ cubic structure. Largest spheres represent La (green), intermediante spheres V (red), and smallest spheres (black and grey) Al. Grey spheres represent the Al(3) site.

used the CRITIC program to perform basin integrations and connectivity analysis. Three different superstructures were considered for this study: $Al_{20}V_2La$, $Al_{21}V_2$, and $Al_{18}V_2La$. For $Al_{20}V_2La$ the three Al sites are fully occupied and La occupies the void. In the case of $Al_{21}V_2$ all the sites are occupied by Al including the void. Finally for $Al_{18}V_2La$, the vacancy is occupied by La but the Al(3) site is empty. In the case of $Al_{20}V_2La$ the computed lattice constant after relaxation was 14.598 Å similar to previously reported [82], and nearly the same as the experimental value. For $Al_{21}V_2$ the computed value was about 1% smaller than the reported value [84].

The calculated electron density of states is shown in Fig. 11 for $Al_{20}V_2La$. A good part of the V contribution is seen to span E_F, consistent with hybridization expected for a covalently bonded V-Al(2) framework structure as identified in $Al_{10}V$

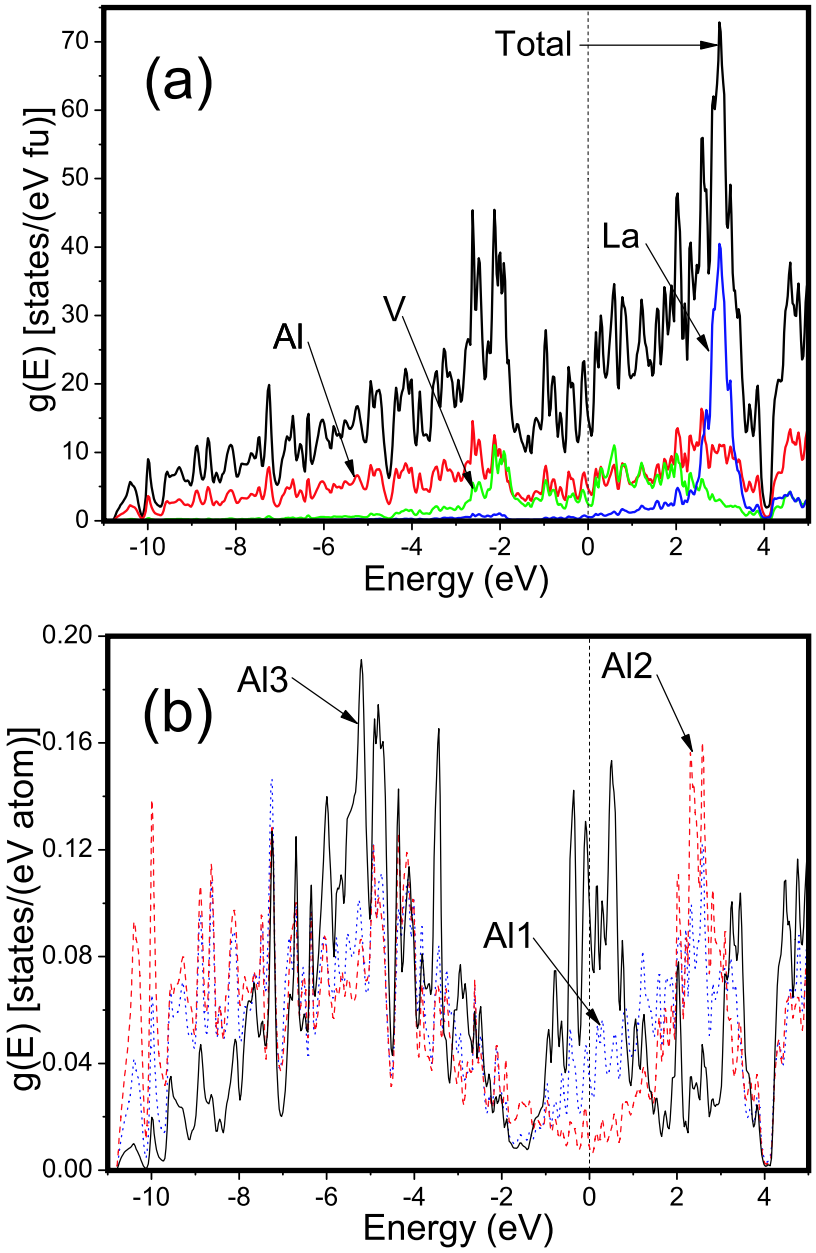

Fig. 11. (a) Total computed electron density of states $g(E)$ for $Al_{20}V_2La$. (b) $s-$partial computed electron density of states $g(E)$ for the three Al sites.

[82], except for the lack of a prominent minimum in Al $g(E)$ near E_F as might be expected for a hybridization gap mechanism [85]. From the $s-$partial computed electron densities of states it can be seen that there is a broad minimum for Al(1) and Al(2). Both of these sites were also identified as covalently bonded in $Al_{10}V$ [82] consistent with this result. But Al(3) can be distinguished as having a maximum near E_F, an indication for the non-bonding character of these atoms.

For the calculated $g(E_F)$ a value of 13.5 states/(eV f.u.) was obtained, where the formula unit refers to the $Al_{40}V_4La_2$ basic symmetry unit from the calculation. We found that this value depends on the broadening function used; in this case we used a Gaussian of width 0.04 eV. The calculated $g(E)$ corresponds to an electronic contribution to the specific heat $\gamma = 16$ mJ/(mol K^2), with moles referenced to the 23-atom basic formula unit. Our experimental value was 20.8 mJ/(mol K^2) [83]. These values are in reasonable agreement.

Narrow features near E_F were found in the calculated $g(E)$ as previously observed for $Al_{10}V$ [82]. I checked that this was not an artifact due to the finite number of k-points used in the calculations, but the number of k points used were enough to have a well converged calculation. Therefore it corresponds to an intrinsic property of these compounds. Also from the bandstructure shown in Fig. 12(a) it is observed that the bands close to E_F include some that are very flat which can correspond to the spikiness in the density of states. I found that these have a large contribution from the non-bonded Al(3) site. For example, Fig. 12(b) shows the Al sites' s contributions for one of the bands crossing E_F. There has been considerable interest in the presence of "spiky" $g(E)$ features in quasicrystals and complex materials [80]. In the present case the spikiness observed for the Al(3) site can be connected to the existence of an array of weakly-bonded metal atoms within the more strongly connected framework.

In order to understand the weak bonding between Al(3) and the void, the forma-

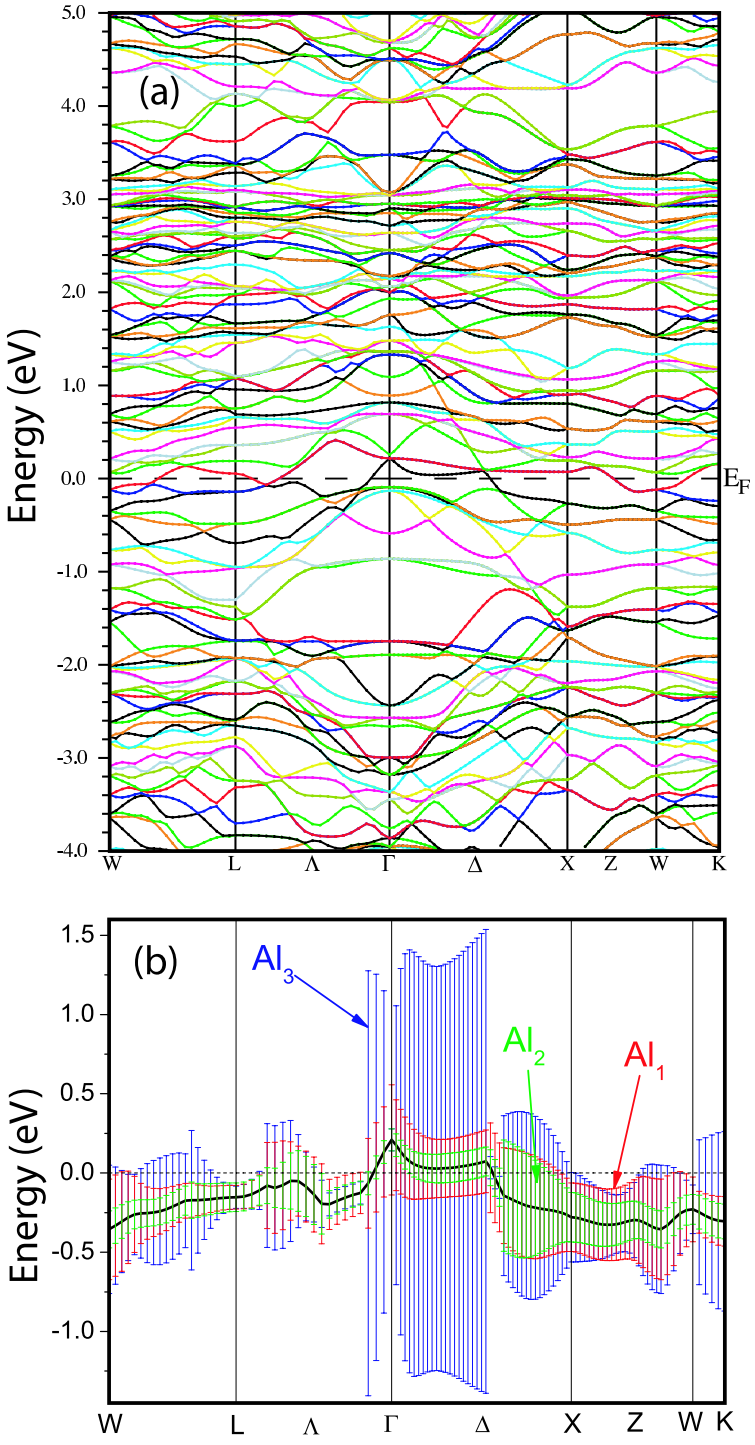

Fig. 12. (a) $Al_{20}V_2La$ bandstructure along the symmetry indicated. (b) One of the bands crossing E_F, with vertical bars indicating the Al-s partial contribution for each Al site.

tion energies were calculated vs. the composition. In each of the cases a corresponding number of calculated per-atom energies for fcc Al and hexagonal La were added to arrive at the formation energy. In the case of $Al_{20}V_2La$ the energy of one atom in fcc Al was added, while for $Al_{21}V_2$ the respective energy of one atom from hexagonal La was added and finally for $Al_{18}V_2La$, three fcc Al atoms were added. The formation energy calculated for $Al_{20}V_2La$, per formula unit relative to the equivalent number of atoms for elemental metals, is -5.38 eV. The calculated La-filled configuration was found to be considerably more stable than the unfilled counterpart by 3.23 eV per formula unit. This result also matches the relative ease with which these compounds can be produced. Jahnatek *et al.* [82] previously reported that the Al filled 8*a* site in $Al_{10.5}V$ was marginally less stable than the unfilled version. By contrast to the marginal stability for Al occupying the 8*a* site, removing Al(3) atoms costs considerable energy; by our calculations the difference is 0.59 eV per site to remove all of the Al(3) atoms from $Al_{20}V_2La$, with the atoms removed forming bulk Al metal. (Note that this is somewhat different from the vacancy formation energy as conventionally defined.) This result is consistent with experimental evidence that the Al(3) sites tend to remain filled, and shows that these sites as a whole are not completely nonbonded.

NMR measurements in our lab allowed us to identify two of the three Al sites (Al(1) and Al(2)), while Al(3) was thought to have a broad signal due to the weak bonds. However, with the help of the first principles calculations I was able to reveal the Al(3) site. From the calculations the EFG's were obtained for all sites. By using the standard equations described in a previous chapter NMR lineshape simulations were performed. Fig. 13 shows the $Al_{20}V_2La$ central transition NMR lineshape simulation compared to the ^{27}Al spin-echo spectrum. In this simulation the main peak at about 98.085 MHz corresponds to the Al(1) site. In the simulations a different distribution of isotropic shifts was added to all sites, corresponding to the breadth of the

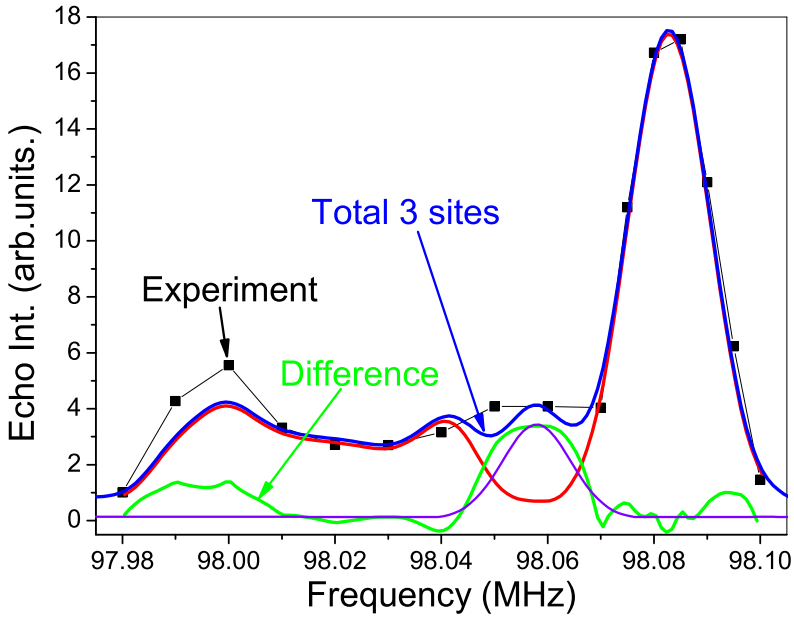

Fig. 13. Measured and calculated NMR lineshape for $Al_{20}V_2La$.

central line, and representing a Knight shift distribution. The center of mass used in the calculations was 97.9974 MHz, as already stated different isotropic Knight shifts were added to each site. For Al(1) a shift of 58 kHz was added, Al(2) did not have any shift and for Al(3) the shift was 32 kHz. Additional center-of-mass shifts for each site due to the second-order quadrupole effect are relatively small and were included in the calculation. Another parameter used was the overall amplitude adjustment which depended in the multiplicity of the sites involved; for example, by symmetry Al(1) has 6 times more atoms than Al(3) therefore its amplitude was multiplied by 6. Al(2) correspondingly has 3 times more atoms than Al(3). At first it was thought that the central transition was due only to Al(1) and Al(2) as shown in Fig. 13 with a red line, and that Al(3) would have a broad contribution because it corresponds to one of the weakly-bonded sites perhaps an indication of disorder. But it is clearly seen with the difference (green) line from the simulation that there is an extra peak at about 98.06 MHz. By setting the multiplicity to one and including the Al(3) site

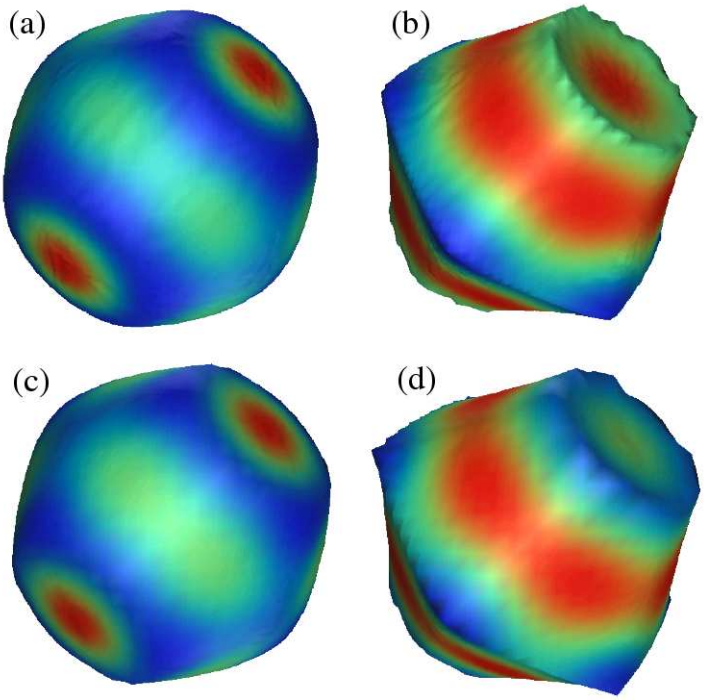

Fig. 14. Atomic basins calculated for (a) La 8*a* site in $Al_{20}V_2La$; (b) Al(3) (16*c*) site in $Al_{20}V_2La$; (c) Al(4) (8*a*) site in $Al_{21}V_2$; (d) Al(3) (16*a*) site in $Al_{21}V_2$.

an excellent agreement is obtained as shown in Fig. 13 with the blue line. This reinforces the formation energy calculation described above, indicating that the Al(3) sites are completely occupied, or nearly so. Our Rietveld refinements also showed this to be the case, however there has been some discrepancy in quoted results for related compounds [83].

We can further use the calculated electron density from the *ab initio* calculations to analyze bonding characteristics through Quantum Theory of Atoms in Molecules (QTAIM) methods. In this model the basins of attraction are constructed using the gradient of the charge density surrounding each atom. Since for ionic crystals basin charges typically approach the expected oxidation states [86] they can provide a good measure of the charge transfer. As seen from Table III, the main such effect in $Al_{20}V_2La$ is a transfer of charge from La to V and the Al framework, with La having

Table III. Basin charges for $Al_{20}V_2La$ and $Al_{21}V_2$, and parameters calculated for bond critical points. $Al_{21}V_2$ labeled according to $Al_{20}V_2La$ convention, with Al(4) = 8*a* site. Units: $\nabla^2\rho$ in $e/Å^4$, ρ in $e/Å^2$.

	$Al_{20}V_2La$	$Al_{21}V_2$
Site	charge(e)	charge(e)
La [Al(4)]	1.0	0.3
V	-0.2	-0.3
Al(1)	0.0	0.0
Al(2)	-0.1	0.0
Al(3)	0.0	0.1
bond	$\nabla^2\rho$, ρ	$\nabla^2\rho$, ρ
Al(1)-Al(2)	-0.132, 0.130	-0.155, 0.131
Al(1)-Al(1)	-0.275, 0.132	-0.364, 0.142
Al(1)-Al(1)	-0.164, 0.123	-0.244, 0.133
Al(2)-V	-0.109, 0.151	-0.146, 0.155
Al(3)-Al(1)	0.049, 0.084	0.046, 0.084
Al(3)-La/Al(4)	0.311, 0.084	0.116, 0.071
Al(1)-La/Al(4)	0.386, 0.075	0.146, 0.071

one net positive charge, thus a considerable portion of the valence charge remaining on-site. The spherical shape of the La basin, shown in Fig. 14(a), is characteristic of such a charged cation. By contrast, the Al(3) basin exhibits 10 equivalent faces with little curvature corresponding to the lack of polarity.

The bond critical points are listed in the lower portion of Table III. The positive $\nabla^2\rho$ and relatively small ρ for each of such point surrounding the La and Al(3) sites are indicative of weak closed-shell or ionic bonding for these sites. Since Al(3) is uncharged, its connection to the cage atoms may be considered to be a very weak metallic bond.

For $Al_{21}V_2$, the basins and the critical values are nearly identical to those of $Al_{20}V_2La$, except for critical values involving the Al(4), the site that replaces for La. Al(4) on this site is found to be ionic, but to a lesser extent than La. Otherwise, the physical properties of the two frameworks should be nearly identical, and treating $Al_{20}V_2La$ as a filled version of $Al_{21}V_2$ should be an appropriate model. Thus our work would also imply that similar vibrational behavior should be characteristic of both materials, including the well-studied $Al_{10}V$.

In summary for this material, a computational study of Al-V-La compounds allowed us to understand the vibrational properties observed in these materials. The strong bond between Al(2) and V sites was confirmed. Narrow features in $g(E)$ at E_F were observed which we attributed to the flatness of the bands. The spikiness in $g(E)$ could be connected to the fact that there is an arrangement of weakly bonded sites. From NMR lineshape simulations we were able to identify the contributions from the three distinct Al sites. Also the weak bonding of the Al(3) and La sites was examined through computed formation energies and through a quantum theory of atoms in molecules treatment.

C. Ba-Cu-Ge Clathrates

1. Structural Behavior in $Ba_8Cu_xGe_{46-x}$

From a previous Ba-Cu-Ge clathrates structure analysis in our group it was determined that these materials have type-I structure with copper content between 4.9 and 5.3 per formula unit, nearly independent of the starting composition [49]. The obtained composition agreed quite closely with the Zintl charge electron balance counting. This implies a gap in the electronic band structure. We initiated this work to establish whether the Zintl behavior inferred from the previous work was correct, including the expected insulating behavior for the $Ba_8Cu_{5.3}Ge_{40.7}$ composition. Also interesting magnetic behavior has been observed in Ba-Cu-Ge clathrates. Magnetization measurements in two different studies indicate a large diamagnetic term in Ba-Cu-Ge clathrates [49, 87]. A more striking effect was the appearance of low-moment ferromagnetism at low temperatures attributed to a dilute concentration of random defects [49]. To understand the magnetic properties and the structural behavior observed in Ba-Cu-Ge clathrates, I performed experimental and *ab initio* computational studies on different type-I $Ba_8Cu_xGe_{46-x}$ $4 \leq x \leq 6$. Exploration of ordered and disordered structures on these materials may give some answers to the magnetic and structural behavior on these compounds.

a. Sample Preparation

Three type-I $Ba_8Cu_xGe_{46-x}$ samples with $x = 4$, 5.3 and 6 were prepared from the pure elements, mixed according to the desired composition, with an initial arc melting under argon. The sample with $x = 5.3$ was prepared by Xiang Zheng, while the other two were prepared by me. A homogeneous type-I phase was obtained in all cases by soaking at 950 °C for three days, then cooling down to 700 °C for four days,

Table IV. X-ray measured parameters for the three samples obtained through Rietveld refinement.

	Cu_4	$Cu_{5.3}$	Cu_6
a (Å)	10.696	10.695	10.693
Relative Occupancy			
Ba $2a$	0.97	0.97	0.97
Ba $6d$	0.96	1.00	1.00
Cu $6c$	0.85	0.80	0.83
Ge $6c$	0.10	0.10	0.10
Cu $16i$	0.03	0.03	0.03
Ge $16i$	0.96	0.96	0.96
Cu $24k$	0.05	0.04	0.05
Ge $24k$	0.93	0.95	0.95
R_p	0.1231	0.1054	0.1000
W_p	0.0798	0.0706	0.0667

similar to the procedure reported by Li et al. [49].

b. Experiment

XRD measurements were performed on a Bruker D8 X-ray Powder Diffractometer, with Rietveld refinement performed using GSAS [60]. NMR experiments were performed at a field of 9 T using a pulse spectrometer [59]. Magnetic properties were measured with a MPMS SQUID magnetometer.

The lattice constant in the previous study was shown to decrease as the number of Cu atoms is increased [49]. From Table IV we see that the same trend is observed, with lattice constants that are similar to those previously reported [49],

where $Ba_8Cu_{5.3}Ge_{40.7}$ is denoted by $Cu_{5.3}$, and similarly for all others. The results also show that the guest sites are almost completely occupied and the Cu atoms reside mostly on the 6*c* sites, although a small part of them are on the 16*i* and 24*k* sites. The reliability of these results can be obtained from the last 2 rows in Table IV.

In Fig. 15 the DC magnetization vs H is shown for the $Ba_8Cu_{5.3}Ge_{40.7}$ sample at 2 K and 100 K. At high field it exhibits a diamagnetism of -0.00129 emu/mol (-2.93×10^{-7} emu/gr.) at 100 K, and -0.00122 emu/mol (-2.78×10^{-7} emu/gr.) at 2 K. These values are about three times smaller than previously found [49]. The diamagnetism is still unusually large as measured here. The diamagnetic susceptibility is considerably larger than the simple core diamagnetism, probably due to interband terms [88]. Recently related models have been of interest in graphene [89]. The flat bands of clathrates and also $Al_{20}V_2La$ provide a good motivation for such large interband terms. We found no evidence of intrinsic paramagnetism in the Zintl composition as previously reported for some samples [49].

c. Computational Results and Discussion

First principles calculations were implemented with the FP-LAPW method by using the WIEN2k code [67]. All structures were minimized in volume and internal structural parameters except for the Zintl configuration due to the large amount of computational time. (However, currently Jing-Han Chen is working in our group on additional extensions of this work to a larger superstructure representing the Zintl composition.) For QTAIM analysis of the resulting electron densities, we used the CRITIC program to perform basin integrations and connectivity analysis. Five distinct cases were considered for this study. In a previous study [90] it was already reported that the Cu atoms preferentially occupy the 6*c* site, also indicated by x-ray results shown in Table IV. I explored cases with different occupations of the frame-

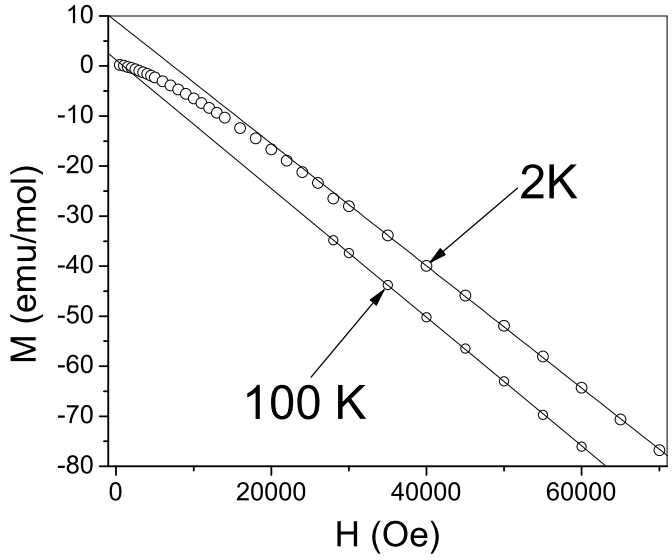

Fig. 15. Dc magnetization vs H for the nominal $Ba_8Cu_{5.3}Ge_{40.7}$ together with a linear fit at 2 K and 100 K.

work sites including those departing from the full occupation of the 6c site by Cu. In one case the Zintl configuration $Ba_8Cu_{5.3}Ge_{40.7}$ was considered with a $1 \times 1 \times 3$ supercell, however this cell was only optimized in volume but not in internal parameters.

Formation energies were obtained from the equation

$$E_{\rm form}(Ba_8Cu_xGe_{46-x}) = E_{Ba_8Cu_xGe_{46-x}} - 8E_{\rm Ba} - xE_{\rm Cu} - (46-x)E_{\rm Ge}, \qquad (5.1)$$

where x is the number of Cu per unit cell. Cases we considered include x =6 and 5. $E_{\rm Ba}$ is the energy per Ba atom in Ba metal, and similarly for the others.

The minimum energy is for the configuration 6-0-0, where the three numbers refer to the Cu occupations of the 6c, 16i and 24k sites, respectively. The lowest computed formation energy is -15.28 eV in this configuration. Also the configurational entropy of these materials was calculated with Boltzmann's entropy formula $S = k_B \log W$, where k_B is the Boltzmann's constant and W is the number of possible

Table V. Calculated lattice constants and relative formation energies (absolute in parenthesis) for different $Ba_8Cu_xGe_{46-x}$ configurations. The first column three numbers refers to the occupation of the $6c$, $16i$, and $24k$ sites, respectively.

Configuration	Lattice constant (Å)	Formation energy (eV)
6-0-0	10.84	0.00 (-15.28)
5-0-0	10.87	0.22 (-15.06)
5-1-0	10.84	1.75 (-13.53)
5-0-1	10.70	2.34 (-12.94)

configurations calculated using the binomial coefficient. In the case of the 5-1-0 configuration the temperature needed to reach the same free energy as the lowest energy configuration 6-0-0 is about 4450 K. For the 5-0-1 configuration the result is 5450 K. These two temperatures are very high. From Table V and the calculated configurational entropies it is clearly seen that the Cu atoms are most likely on the $6c$ site.

The computed lattice constants for $Ba_8Cu_6Ge_{40}$ in the 6-0-0 and $Ba_8Cu_5Ge_{41}$ in the 5-0-0 configurations show behavior similar to the experimental data, with the inclusion of Cu decreasing the lattice constant. Also in the 5-0-1 configuration the lattice constant is much smaller indicating that this may not be a physical case.

The Zintl concept implies a gap in the electron density of states at the Fermi level. In Fig. 16 the bandstructures together with $g(E)$ are shown for the three lowest energy calculations. There is a gap for $Ba_8Cu_6Ge_{40}$ and $Ba_8Cu_5Ge_{40}$ but it is not at the Fermi level because these are not Zintl configurations due to the excess or lack of Cu. The system behaves close to that of a rigid band model where the band dispersion is the same but the Fermi level changes. The Zintl configuration shown

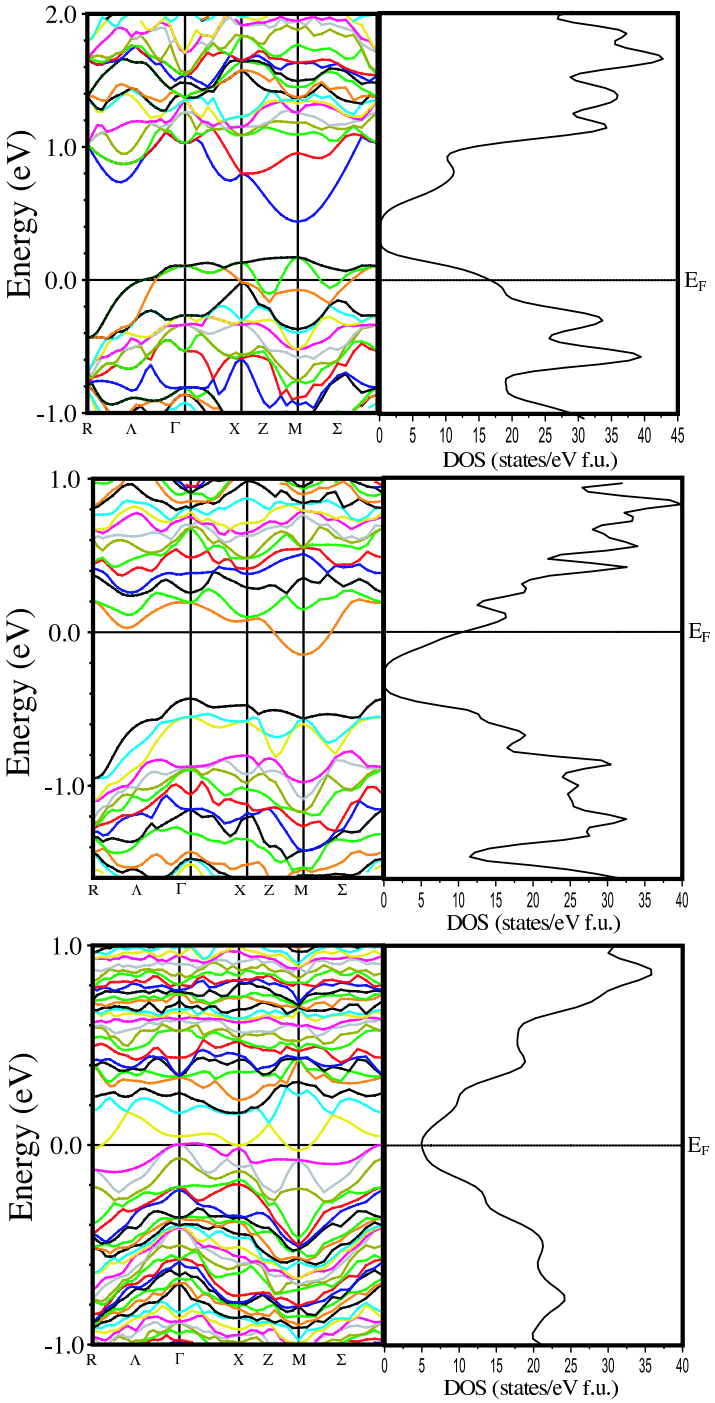

Fig. 16. Bandstructures and $g(E)$ for 6-0-0, 5-0-0 and 5.3-0-0 configurations in $Ba_8Cu_xGe_{46-x}$ with $5 \leq x \leq 6$.

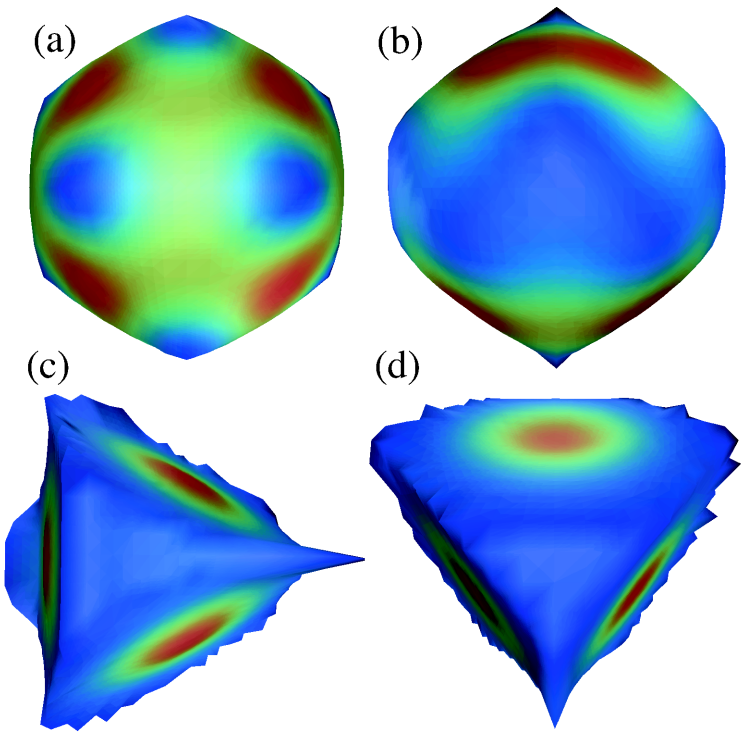

Fig. 17. Atomic basins calculated for (a) Ba 2*a* site; (b) Ba 6*d* site; (c) Cu 6*c* site; (d) Ge 24*k* site in $Ba_8Cu_6Ge_{40}$ in the 6-0-0 configuration.

in Fig. 16(c) was also calculated and a pseudo-gap is observed, however without complete minimization of parameters in this case. Recently Jing-Han Chen started the minimization of the internal parameters in the Supercomputing Center [91]. In the new calculation the pseudo-gap changed to a nearly complete gap at E_F with the optimization of the internal parameters. From these results it is confirmed that Ba-Cu-Ge clathrates follow a Zintl stabilization mechanism.

In Fig. 17 the calculated basins from QTAIM calculations are shown. Fig. 17 (a) and (b) correspond to the 2*a* and 6*d* sites, respectively. From the shape of the basins it can be inferred that the atomic displacement of the cage-center atom is more restricted for the small cage. Ba in the smaller cage is less likely to rattle since it has stronger bonds with the framework. The six-ring faces of the framework in the large cage are

Table VI. Basin charges for $Ba_8Cu_6Ge_{40}$, and parameters calculated for bond critical points. Units: $\nabla^2\rho$ in $e/\text{Å}^4$, ρ in $e/\text{Å}^2$.

Site	Basin charge
Ba2*a*	1.21
Ba6*d*	1.40
Cu6*c*	-0.14
Ge16*i*	-0.19
Ge24*k*	-0.33
bond	$\nabla^2\rho$, ρ
Ge24*k*-Ge24*k*	-0.018, 0.058
Ge16*i*-Ge24*k*	-0.028, 0.063
Cu6*c*-Ge24*k*	0.056, 0.048
Ge24*k*-Ba6*d*	0.023, 0.011
Ge16*i*-Ge16*i*	-0.042, 0.068
Ba2*a*-Ge16*i*	0.033, 0.015
Ba2*a*-Ge24*k*	0.025, 0.012

parallel to the flat faces of the corresponding basin (Fig. 17(b)). This reflects the rattling of the guest atoms in the large cages which is easier and essentially restricted to these planes. It can also be seen from the atomic displacement parameters that Ba in the large cage was more likely to rattle [92]. In Fig. 17 (c) and (d) the Cu 6*c* and Ge 24*k* basins are shown. For the Ge 16*i* site (not shown) the basin is similar to that of the Ge 24*k* site. These basins form nested tetrahedra, making it clear that the framework behaves as an sp^3 network of connected atoms.

In Table VI all the bond critical points for $Ba_8Cu_6Ge_{40}$ in the 6-0-0 configuration are listed. From these it can be deduced that the Ba in the large cage is only bound to the Ge 24k sites, its bond is the weakest of all. By contrast, the Ba in the small cage has bonds with the Ge 16i and Ge 24k sites, however they are also weak. The positive $\nabla^2\rho$ and relatively small ρ for each Ba in the 2a and Cu 6c sites are indicative of weak closed-shell or ionic bonding for these sites as the results from the previous section in Al-V-La [83]. The strongest bonds belong to the Ge-Ge in the 16i sites. The main charge transfer is to the Ge 24k sites from the Ba atoms as seen in Table VI. Cu on the 6c sites has a strongly ionic bond, even though it adheres to a close Zintl stabilization mechanism. By contrast in Ba_8Ge_{43} there is the appearance of three vacancies per unit cell which violates the Zintl criterion [93]. As will be shown latter in the chapter this material, with substitution of Al, behaves as an "imperfect" Zintl material.

D. Ba-Ga-Sn Materials

$Ba_8Ga_{16}Sn_{30}$ is an interesting material because besides its excellent thermoelectric properties and the possibility for carrier tuning, it shows a structural dimorphism, crystallizing as type VIII (α phase) or type I (β phase) clathrate, depending on the annealing conditions. Both types have been shown to have low thermal conductivity with a behavior similar to amorphous SiO_2, together with prominent rattling behavior [34, 94, 95]. Thus it is important to study the variations in thermal and electrical behavior for the two different types of structures.

1. $Ba_8Ga_{16}Sn_{30}$ Type-I Clathrates

a. Sample Preparation

After exploring the annealing conditions, two type-I samples of nominal composition $Ba_8Ga_{16}Sn_{30}$ were successfully prepared from the pure elements, mixed according to the desired composition, with an initial arc melting under argon. Type-I was obtained by soaking at 900 °C for 50 hours, then slow cooling (100 hours) to 500 °C, similar to the procedure reported by Suekuni *et al.* [34].

b. Experiment

XRD measurements were performed on a Bruker D8 X-ray Powder Diffractometer, with Rietveld refinement performed using EXPGUI [60]. Wavelength dispersion spectroscopy (WDS) measurements were done in a Cameca SX50 equipped with 4 wavelength dispersive x-ray spectrometers. NMR experiments were performed by Xiang Zheng at a field of 9 T using a pulse spectrometer described previously [59].

From XRD and WDS measurements it was found that the two type-I samples consist of a type-I major phase, with a small $Ba(Ga,Sn)_4$ minor phase as well as some

Table VII. Framework site occupations from Rietveld refinements of type-I $Ba_8Ga_{16}Sn_{30}$. Reprinted table with permission from [96] © (2010) Cambridge Journals.

Sample	Atom	6*c*	16*i*	24*k*
IA	Ga	2.01	5.81	8.15
IA	Sn	3.25	9.58	16.93
IB	Ga	2.42	5.57	7.93
IB	Sn	3.26	10.77	15.77

remaining Sn and Ga flux. The $Ba(Ga,Sn)_4$ amount is such that only about 1 % of Ga atoms occur in this phase, giving for example negligible contribution to NMR measurements. I found no evidence for coexistence of type I and type VIII clathrate structures in these samples. The refined Ga and Sn framework occupation values are summarized in Table VII. In scans of our samples by WDS, the obtained composition assuming a completely full framework for type I is $Ba_{7.80}Ga_{16.15}Sn_{29.85}$. If we assume that the framework occupation is similar to the sum of the Ga and Sn atoms from Rietveld refinements shown in Table VII, the compositions are: $Ba_{7.64}Ga_{16.00}Sn_{29.58}$ for type I.

c. Computational Results and Discussion

Ab-initio calculations were done for calculation of the EFG's, with subsequent numerical simulation of NMR lineshapes as described before. Calculations were implemented with FP-LAPW method by using the WIEN2k code [67]. All superstructures were minimized in volume and internal parameters.

I considered 16 different superstructures with distinct occupation of framework sites. These are summarized in Table VIII, where the first three columns indicate the

number of Ga atoms per cell in each site of the parent $Pm\bar{3}n$ structure, and the fourth column shows the number of adjacent Ga-Ga pairs per cell. Cubic cell symmetry was retained, leaving 54 independent atoms ($P1$ space group), except for a few cases allowing higher symmetry. Half of these configurations were taken from previous work on $Ba_8Ga_{16}Ge_{30}$ [97] and $Ba_8Al_xGe_{46-x}$ [98] where the minimum energy configurations where found. Additional configurations were modeled after the proposal by Kozina *et al.* [99] for $Ba_8Ga_{16}Sn_{30}$. In the latter work, EXAFS simulations indicated the number of Ga-Ga bonds to be 15±5 % of all framework bonds, corresponding to a range of 3 to 6 Ga-Ga bonds per unit cell. By Rietveld refinements of XRD it was found that the Ga framework occupation is close to 4, 6, and 6 in the $6c$, $16i$ and $24k$ sites, respectively.

The configurations in Table VIII are arranged from lowest to highest relative formation energy. The formation energy was calculated from the equation

$$E_{\text{form}}(Ba_8Ga_{16}Sn_{30}) = E_{Ba_8Ga_{16}Sn_{30}} - 8E_{\text{Ba}} - 16E_{\text{Ga}} - 30E_{\text{Sn}} \tag{5.2}$$

where E_{Ba} is the energy per Ba atom in Ba metal, similarly for all others. The lowest formation energy was for the configuration 3-1-12-0, where the four numbers correspond to the first four columns in Table VIII. This configuration also corresponds to the lowest energy configuration in the case of $Ba_8Ga_{16}Ge_{30}$ [97] and $Ba_8Al_{16}Ge_{30}$ [98]. The absolute 3-1-12-0 formation energy is -17.8122 eV. However, 3-5-8-0 is almost identical in energy, and moreover is in close agreement with the Ga framework occupation obtained through Rietveld refinements. This configuration (with per-site occupation very close to a random configuration) was not considered in previous studies [97, 98].

From the results reported in Table VIII it is also clearly seen that Ga-Ga bonds are not energetically favorable, as the formation energy generally increases as the

Table VIII. Ga framework occupation for $Ba_8Ga_{16}Sn_{30}$ with the type-I parent structure. Two different 4-6-6-4 and 4-6-6-3 configurations have been included. Δ E refers to the relative energy per formula unit with respect to the lowest energy configuration, 3-1-12-0. Reprinted table with permission from [96] © (2010) Cambridge Journals.

6*c*	16*i*	24*k*	Ga-Ga bonds	Δ E (eV)
3	1	12	0	0
3	5	8	0	0.0159
3	4	9	0	0.1742
3	2	11	0	0.2026
3	3	10	0	0.3295
3	4	9	2	0.3844
4	2	10	2	0.4024
4	6	6	4	0.6855
5	3	8	4	0.8898
4	6	6	4	0.9513
4	6	6	2	1.0774
4	6	6	0	1.1973
4	6	6	5	1.3009
4	6	6	3	1.4388
4	6	6	1	1.4400
4	6	6	3	2.2125

number of Ga-Ga bonds increases, and the lowest-energy configurations found all contain no Ga-Ga bonds. Thus it appears that a conformation with zero Ga-Ga bonds is most favored, which follows the general trend observed in previous studies [97, 98] for Ba-Al-Ge and Ba-Ga-Ge materials.

From the *ab initio* calculations we obtained electric field gradients (EFG's) for each Ga site from the calculated all-electron charge distribution, using a method used in recent years with considerable success for analysis of NMR spectra [70]. We applied this method to $Ba_8Al_xGe_{46-x}$ [98] with excellent results as will be shown in the next section. From computed EFG matrix elements the quadrupole lineshape was simulated by summing a contribution from each m to $m+1$ transition for ^{71}Ga, including the first and second-order quadrupole shift for each transition. The nuclear quadrupole moment used for ^{71}Ga was Q = 0.11 $\times$ 10^{-28} m^2.

Four different configurations are compared in Fig. 18(a) and Fig. 18(b), including the two lowest energy and the 4-6-6-4 and 5-3-8-4 configurations. It is seen that the best fit to the data is represented by the 5-3-8-4 configuration. Along with 5-3-8-4, the proposed [99] 4-6-6-4 and 4-6-6-5 (not shown) are similar but their calculated lineshapes have a larger deviation from the experimental results. Comparing simulations (not shown) for all of the configurations in Table VIII, none yields an agreement as close as these three. Generally, the width of the simulated satellite spectrum becomes broader as the number of Ga-Ga bonds increases, since the asymmetry induced by Ga-Ga bonds results in a larger EFG. This is shown for the four configurations in Fig. 18(a) and Fig. 18(b). Increased EFG's also lead to increased second-order quadrupole broadening of the central line.

In Fig 19(a) and Fig. 19(b) only the simulations for the best fit configurations are shown. For both the agreement is reasonable, although 5-3-8-4 is closest to the NMR results. These configurations indicate a number of Ga-Ga bonds similar to what

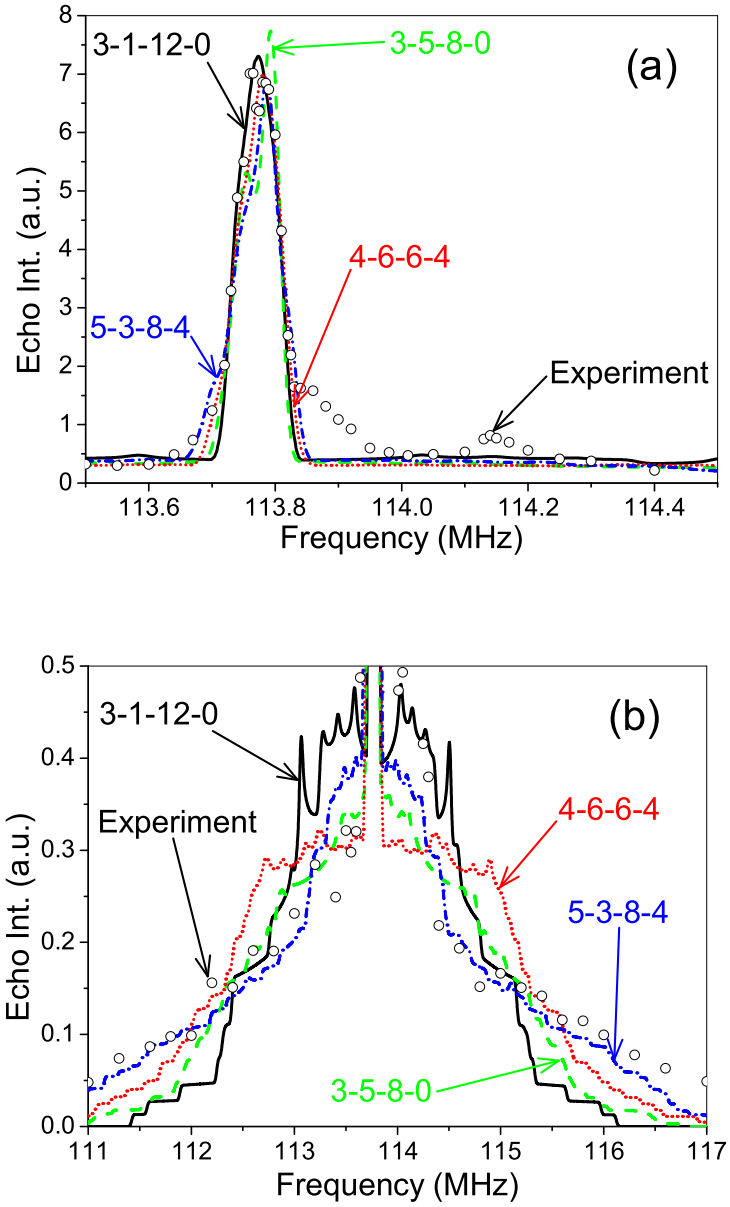

Fig. 18. ^{71}Ga NMR lineshape simulations for type-I $Ba_8Ga_{16}Sn_{30}$. (a)^{71}Ga NMR lineshape together with 4 calculated configurations in the central transition spectral region. (b)^{71}Ga NMR lineshape together with 4 calculated configurations in the satellite spectral region. Reprinted figure with permission from [96] © (2010) Cambridge Journals.

was previously obtained from EXAFS measurements [99]. Since the NMR resonance width varies rapidly with the number of Ga-Ga bonds, these results point to 4 per cell as the most likely number, even though the calculated energies for these configurations are higher than those of the ground state configuration. It is not entirely clear why the lowest energy configurations do not appear to be favored as they are in $Ba_8Ga_{16}Ge_{30}$ [97] and $Ba_8Al_{16}Ge_{30}$ [98], although the calculated results (Table VIII) indicate a generally smaller energy difference between different configurations than, for example, in $Ba_8Al_{16}Ge_{30}$ [98]. Also the results in Table VIII indicate that the 4-6-6-x configurations tolerate Ga-Ga contacts better than other configurations, since among these the 4-6-6-4 configuration has the lowest energy. With more phase space to explore, such a configuration might be favored on the basis of configurational entropy.

For the low-energy minimized type-I configurations, we found that the Ga-Ga framework bonds are shortened in the calculated results, relative to the other bonds, in general agreement with the trend identified experimentally through EXAFS [99]. Among the structures considered here, I looked carefully at the distribution of bond lengths in the 3-1-12-0, 3-5-8-0, 3-4-9-0, 4-6-6-4, 4-6-6-5, and 5-3-8-4 superstructures, the first three being the most stable calculated structures. In each configuration the average framework bond length falls between 2.77 and 2.79 Å. These values are 1-2% larger than the experimental average obtained crystallographically [94]; such a difference is typical of DFT calculated results using the PBE-GGA method [62]. The average Sn-Sn bond length is 2.89 Å in the three structures with no Ga-Ga bonds, and it is 2.86 Å in the 4-6-6-4, 4-6-6-5 and 5-3-8-4 configurations. The average Ga-Sn bond length ranges from 2.72-2.76 Å, while the Ga-Ga bond average for 4-6-6-4, 4-6-6-5 and 5-3-8-4 is 2.67 Å. Thus the calculated Ga-Ga bond-lengths are reduced by an average of 4% relative to the average framework bond, consistent with the

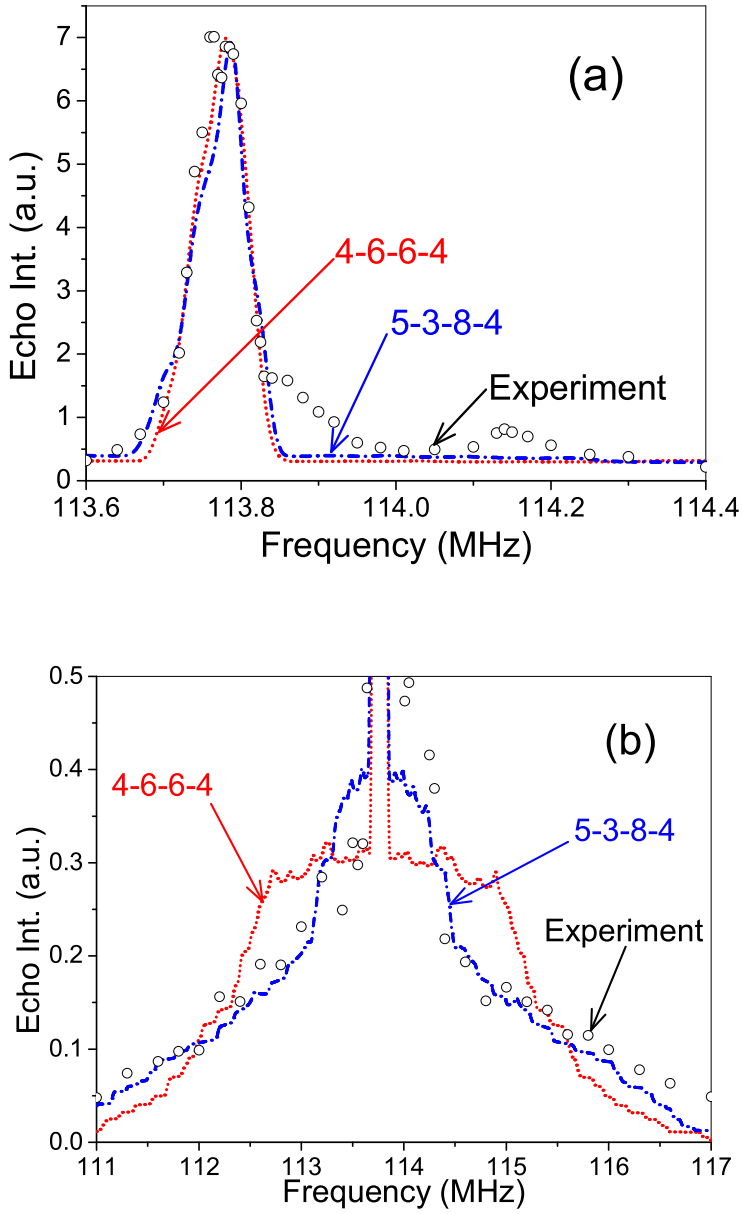

Fig. 19. NMR lineshape simulations and measurements for best fitting configurations in type-I $Ba_8Ga_{16}Sn_{30}$. (a) Central transition. (b) Satellites region. Reprinted figure with permission from [96] © (2010) Cambridge Journals.

experimental trend, although smaller by almost a factor of two than the reported reduction amount [99].

In our previous study on the $Ba_8Al_{16}Ge_{30}$ system [98] shown in the next section, calculated Al-Al bond lengths exceeded those of Ge-Ge by an average of 0.06 Å, a result that we have since observed for a number of additional configurations. An EXAFS report for $Ba_8Ga_{16}Ge_{30}$ [100] also indicated a small lengthening ($\sim$0.02 Å) of group-III atom bond lengths relative to the framework average, independent of carrier type. Thus the trend in type-I $Ba_8Ga_{16}Sn_{30}$ opposes that of the two Ge-based systems. The latter results may be explained by bond destabilization; indeed, for $Ba_8Al_{16}Ge_{30}$ our calculated results indicate an energy cost per Al-Al bond that is roughly twice the values found here for $Ba_8Ga_{16}Sn_{30}$. On the other hand, in $Ba_8Ga_{16}Sn_{30}$ the relative atomic sizes appear to dominate; the sum of covalent radii for Ga-Ga (2.5 Å) is considerably smaller than the expanded framework bond length in this material.

I also find that the large-cage Ba atoms have significant off-center displacements in the type-I $Ba_8Ga_{16}Sn_{30}$ configurations; for example in 3-1-12-0 the displacement is 0.5 Å from the cage center. This displacement is toward the center of a Ga-Sn pair occupying 24*k* sites of the original type-I lattice. Such large displacements are consistent with the reported very low-frequency vibrational mode for this cage [94]. However, calculated configurations do not feature large distortions of the cage shape itself.

2. $Ba_8Ga_{16}Sn_{30}$ Type-VIII Clathrates

a. Sample Preparation

I also succeeded in preparing two type-VIII samples of nominal composition $Ba_8Ga_{16}Sn_{30}$. These were prepared from the pure elements, mixed according to the

Table IX. Framework site occupations from Rietveld refinements, for two type-VIII $Ba_8Ga_{16}Sn_{30}$ samples.

Sample	Atom	2*a*	8*c*	12d	24*g*
VIIIA	Ga	0.55	2.13	5.15	6.50
VIIIA	Sn	1.38	4.82	6.97	16.42
VIIIB	Ga	0.32	2.83	5.22	6.49
VIIIB	Sn	1.25	5.21	5.43	19.97

desired composition, with an initial arc melting under argon. Subsequent annealing at 500 °C was used. This procedure agrees with the reported by Suekuni [34].

b. Experiment

XRD measurements were performed on a Bruker D8 X-ray Powder Diffractometer, with Rietveld refinement using EXPGUI [60]. Four-probe electrical resistivity (ρ), steady-state Seebeck coefficient (S), and steady-state thermal conductivity (κ) measurements were performed on a Quantum Design PPMS system from 270 K down to 2 K.

The refined Ga and Sn framework occupation values are summarized in Table IX. In WDS scans of our samples, the obtained average of the two samples composition is $Ba_{7.66}Ga_{16.28}Sn_{29.72}$ assuming a completely full framework for type-VIII. If we assume that the framework occupation is similar to the sum of the Ga and Sn atoms from Rietveld refinements shown in Table IX, the composition is: $Ba_{7.37}Ga_{15.69}Sn_{28.63}$.

Thermoelectric properties were measured for sample VIIIA. In Fig. 20(a) and Fig. 20(b) the resistivity, ρ and S from 270 to 2 K are shown. The positive S indicates that the majority carriers in the sample are holes. The magnitude of S increases with increasing temperature similar to the behavior of degenerate semiconductors. This be-

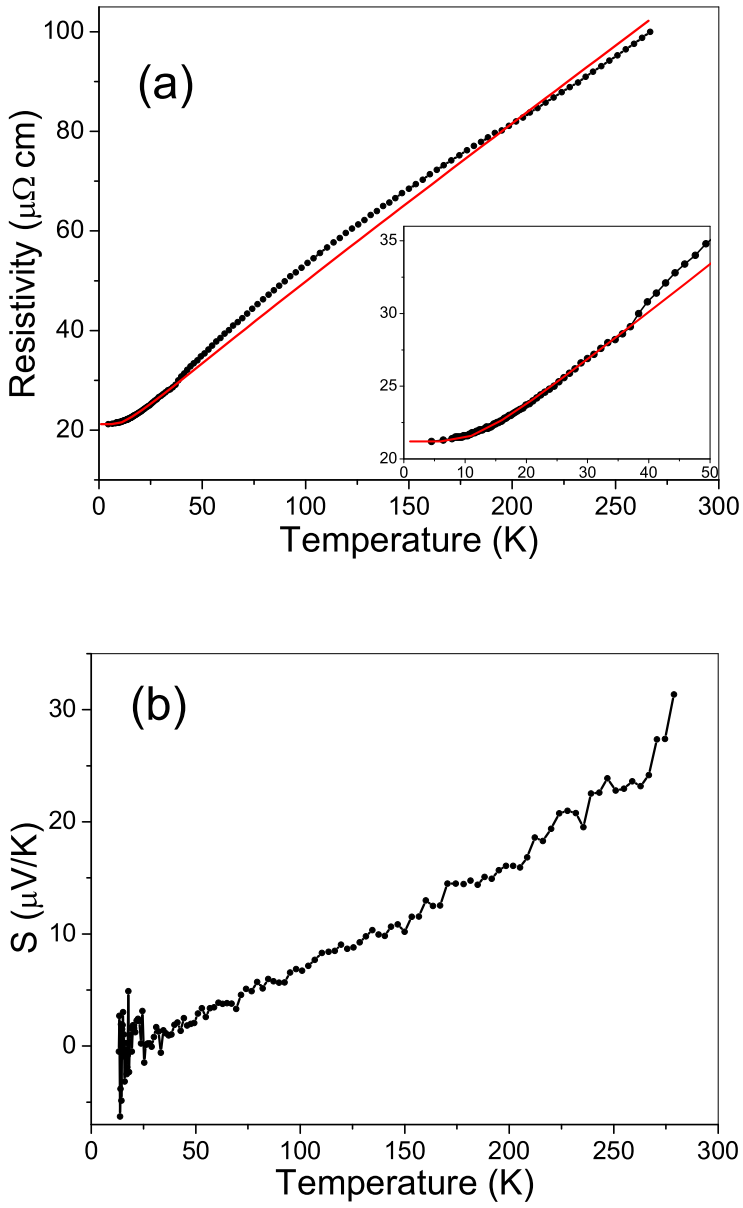

Fig. 20. (a) Resistivity data for $Ba_8Ga_{16}Sn_{30}$ type-VIII sample VIIIA. The red line corresponds a pure electron-phonon scattering plus an Einstein oscillator mechanisms. In the inset the low temperature data. (b) Seebeck coefficient measurements for $Ba_8Ga_{16}Sn_{30}$ type-VIII sample VIIIA.

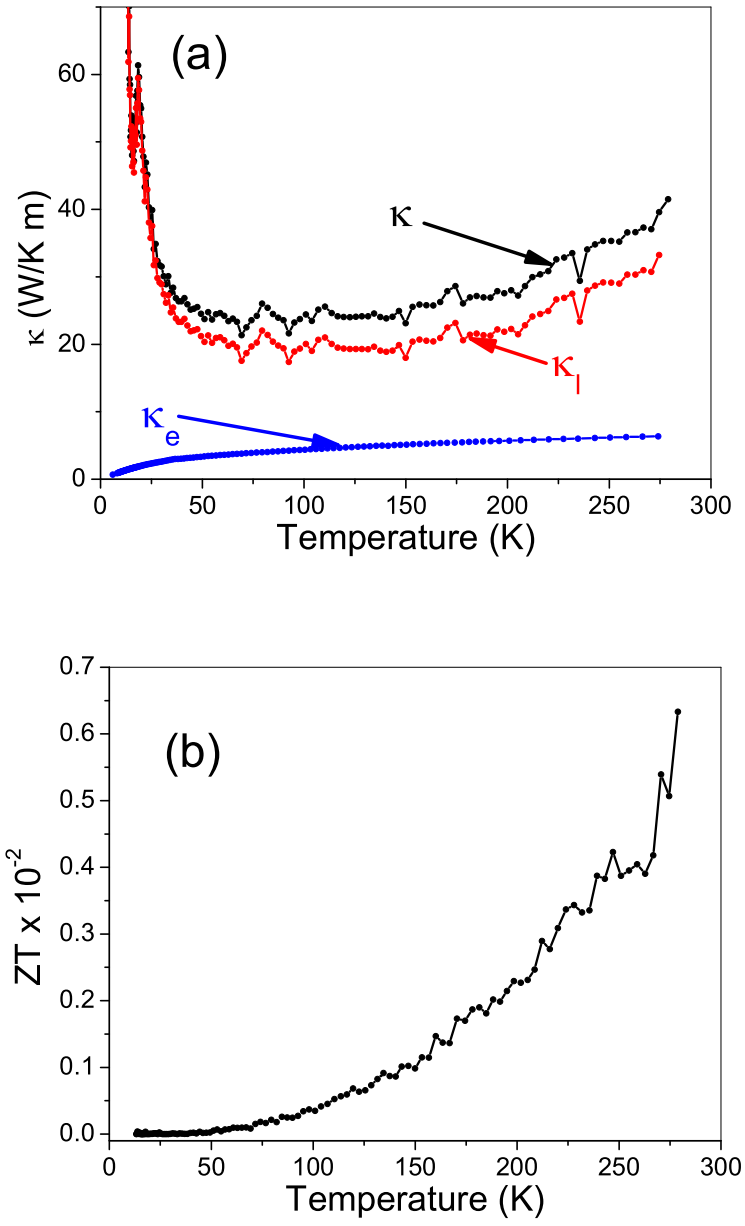

Fig. 21. (a) Total thermal conductivity (κ), together with phonon (κ_l) and electron (κ_e) contribution for $Ba_8Ga_{16}Sn_{30}$ type-VIII sample VIIIA. (b) Thermoelectric figure of merit (ZT) for $Ba_8Ga_{16}Sn_{30}$ type-VIII sample VIIIA.

havior is confirmed with monotonic temperature dependence of ρ where $d\rho/dT > 0$ is for metallic-like behavior. The resistivity was fitted with a Bloch-Grüneisen function for pure electron-phonon scattering [101] given by $\rho(T) = C_B \frac{T^5}{\theta_D^6} \int_0^{\theta_D/T} \frac{x^5}{(e^x-1)(1-e^{-x})} dx$ plus an Einstein oscillator term given by $\rho(T) = \frac{C_E}{T(e^{\theta_E/T}-1)(1-e^{-\theta_E/T})}$ [102]. The values from the fitting were: $\theta_D = 223$ K similar to the value by Nolas [103] and $\theta_E = 58$ K. Weiping Gou also obtained close values ($\theta_D = 187$ K and and $\theta_E = 51$ K) from specific heat measurements [104]. It is important to note that the Einstein oscillator model fit agrees extremely well at low temperatures, there is no sign of $\rho \sim T^2$ associated with a strongly anharmonic phonon mode [105].

The largest absolute value of S at 270 K of about 30 μV/K (Fig. 20(b)) is small compared with the value previously reported for an n-type single crystals [58] that show a value of approximately -250 μV/K at the same temperature, but it is still in agreement with polycrystalline samples [35, 106]. Large values of Seebeck coefficient are usually associated with low carrier density which in turn leads to high resistivity values.

The temperature dependent thermal conductivity $\kappa(T)$ was also measured, with the results displayed in Fig. 21(a). $\kappa(T)$ exhibits an increase as the temperature is decreased at low T, similar to the observed behavior in $Ba_8Al_{16}Si_{30}$ [107]. The total thermal conductivity can be written as $\kappa = \kappa_l + \kappa_e$. The electronic thermal conductivity κ_e was calculated using the Wiedemann-Franz relationship ($\kappa_e = L_0 \sigma T$ with $L_0 = 2.45 \times 10^{-8}$ V^2 K^{-2}) from the measured resistivity, ρ, with the results displayed in Fig. 21(a). The thermal conductivity in this case is much higher than that of many compounds presently under investigation having about $\kappa_L = 1$ Wm^{-1}K^{-1} [108]. The rise at high temperature might be due in part to radiation losses from the sample. Even though κ is higher than in many previous reports on clathrates [58] it is still low compared with most metals. The values are associated with the vibrations

of the guest atoms inside the cages, allowing them to rattle and dissipate heat. The raise in κ_l from 28 K to 18.5 K follows a $T^{-1.5}$ power law. For most materials κ follows a T^3 behavior at low temperatures due to scattering with the boundaries, therefore κ must go to zero as the temperature goes to zero, however this behavior is not observed up to 13 K in this case. In contrast, at high temperatures crystalline materials have a T^{-1} power law due to Umklapp phonon-phonon scattering processes. Meanwhile, glassy materials have a T^2 power law at low temperatures as seen in $Sr_8Ga_{16}Ge_{30}$ [27]. The S and κ measurements show large fluctuations, a possible reason is that S and κ were measured continuously as a function of temperature.

In Fig. 21(b) the dimensionless figure of merit given by $ZT = S^2\sigma T/\kappa$ is shown for type-VIII $Ba_8Ga_{16}Sn_{30}$ sample VIIIA. ZT remains low over this temperature range mainly because the Seebeck coefficient is below 100 μV/K, but also because κ is high. The overall figure of merit is on the same order of magnitude as the reported values for type-I $Ba_8Al_{16}Si_{30}$ [107], $Ba_8Cu_6Ge_{40}$ [109], and $Ba_8Ag_xGe_{46-x-y}\square_y$ [110]. For $Ba_8Al_{16}Si_{30}$ [107] the resistivity is around 870 $\mu\Omega$cm at room temperature which is about eight times higher than the value obtained in our measurements. However the thermal conductivity is about seven times smaller in the case of $Ba_8Al_{16}Si_{30}$. For $Ba_8Cu_6Ge_{40}$ [109] the resistivity is about twenty times higher than the obtained in our measurements. However the Seebeck coefficient is about two times larger and also the thermal conductivity is about twenty times smaller. A common feature in our measurements is the lower resistivity in our sample. The reported value of ZT for $Ba_8Ag_xGe_{46-x-y}\square_y$ [110] is over a wider range of temperature, and up to room temperature the reported results are very close to our values. In the case of $Ba_8Ag_{4.1}Ge_{41.4}\square_{0.5}$ [110] ZT reaches a maximum at 800 K of about 0.45.

Table X. Different computed configurations for type-VIII $Ba_8Ga_{16}Sn_{30}$. The first four columns designate Ga occupation of the corresponding framework sites per cubic cell. Energy refers to the relative energy with respect to the lowest energy configuration, 0-6-6-4-0 (absolute energies in parenthesis).

$2a$	$8c$	12d	$24g$	Ga-Ga bonds	Energy (eV)
0	6	6	4	0	0.00 (-12.21)
0	5	6	5	0	0.15 (-12.06)
0	4	7	5	1	0.48 (-11.73)
0	4	6	6	6	3.93 (-8.28)
0	8	8	0	0	4.19 (-8.02)

c. Computational Results and Discussion

Similar to what was done for type-I structures, first principles calculations were implemented with the FP-LAPW method by using the WIEN2k code [67]. The BoltzTraP code [111] was also used for calculation of the Seebeck coefficient, wherein there is only one adjustable parameter (carrier density). All structures were minimized in volume and internal parameters. For the parent I$\bar{4}$3m type-VIII structure there is only one guest site ($8c$), and 4 different framework sites denoted $2a$, $8c$, $12d$ and $24g$ in the Wyckoff notation. Five different superstructures were considered with different Ga occupation of the distinct sites in the parent I$\bar{4}$3m type-VIII structure. A cubic cell symmetry was retained, leaving 54 independent atoms ($P1$ space group), except for a few cases allowing higher symmetry. In Table X the five calculated configurations are shown together with the number of Ga-Ga bonds and formation energies of the diverse configurations.

The configurations in Table X are arranged from lowest to highest difference formation energy. The formation energy was calculated from Eq. 5.2, where E_{Ba} is the

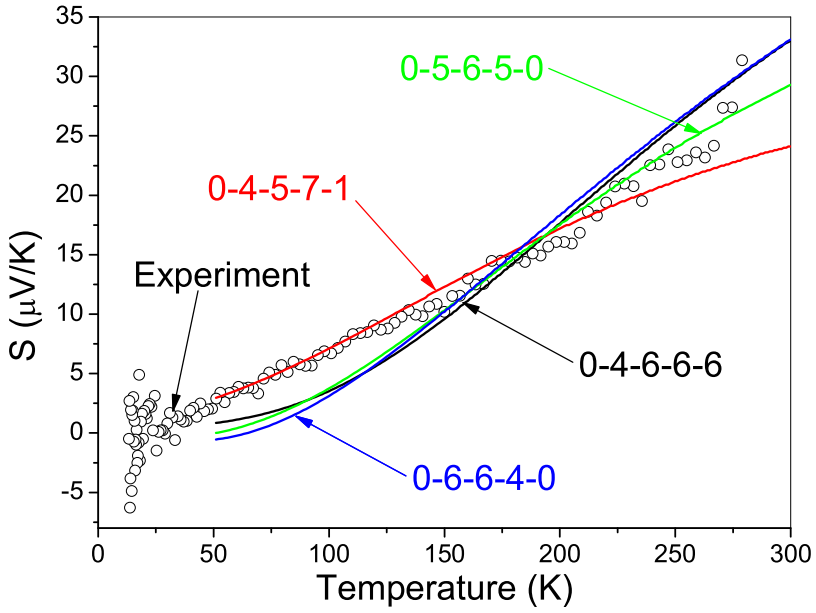

Fig. 22. Calculated Seebeck coefficients for $Ba_8Ga_{16}Sn_{30}$ type-VIII in the different considered configurations.

energy per Ba atom in Ba metal, and similarly for all others. The lowest formation energy was for the configuration 0-6-6-4-0, where the five numbers correspond to the first five columns in Table X. The lowest energy structure 0-6-6-4-0 follows the same trend as in $Ba_8Ga_{16}Ge_{30}$ [97] and $Ba_8Al_xGe_{46-x}$ [98] where the lowest energy configurations corresponded to no Ga-Ga or Al-Al bonds. Note that the configuration 0-8-8-0-0 was previously reported to be the lowest energy [112], which however is quite different from the results obtained here.

The Seebeck coefficients were calculated in the temperature range 50 K to 300 K by using the semi-classical Boltzmann model as described in chapter IV. The number of $k-$points considered for each calculation was 20000, somewhat larger than the value used in previous reports ($25 \times 25 \times 25$) [110]. Fig. 22 depicts the calculated and experimental Seebeck coefficients. All the considered configurations are shown.

The Fermi level was adjusted to obtain a fit to the data. In the case of the best fit configuration 0-4-5-7-1 the Fermi level used was 0.148 eV lower than the obtained from Wien2k calculations which would represent native acceptor density. From its calculated $g(E)$ (not shown), the 0-4-5-7-1 configuration is a semiconductor with the Fermi level placed just below the valence band. With the adjustment of the carrier density to match the experimental Seebeck coefficients the 0-4-5-7-1 configuration has more holes. The other three configurations agreed poorly with the experimental data at all temperature ranges. Thus with only one parameter we obtained excellent agreement and a best fitting for the configuration which also gave one of the lowest formation energy.

In summary a study on type-I and type-VIII $Ba_8Ga_{16}Sn_{30}$ is reported. For type-I $Ba_8Ga_{16}Sn_{30}$ a description of the Ga local configuration was obtained through NMR lineshape simulations, with the preferred configuration and Ga-Ga bonds similar to previously reported by EXAFS studies. Bond lengths in type-I $Ba_8Ga_{16}Sn_{30}$ showed behavior opposite to that previously observed in $Ba_8Al_{16}Ge_{30}$ and $Ba_8Ga_{16}Ge_{30}$. For type-VIII $Ba_8Ga_{16}Sn_{30}$ transport properties were measured. Resistivity data were fitted to an Einstein oscillator plus Bloch-Grüneisen electron-phonon term. From Seebeck coefficients calculations the best fit was for one of the lowest energy configurations.

E. Ba-Al-Ge Clathrates

In the case of Ba-Al-Ge clathrates the electric and thermal properties are affected by the partial substitution of the framework atoms with metallic species [113, 114]. Therefore a full description of the behavior as a function of the Al substitution will help in the understanding of vacancy formation and Al framework occupation.

The appearance of spontaneous vacancies as in the case of $Ba_8Ge_{43}\square_3$ [42] can serve to maintain electron charge balance in off-stoichiometry materials. In the case of $Ba_8Al_xGe_{46-x}$, near $x = 16$ spontaneous vacancies also appear, even though $x = 16$ should be an ideal Zintl phase and vacancies should not be needed for charge balance. Vacancy formation affects the electronic and transport properties significantly. Therefore it is important to know what is the vacancy variation as a function of Al substitution and also it is meaningful to obtain the framework Al occupation to get a better understanding of the changes in electrical and transport properties.

For large x, this material crystallizes as a type-I clathrate. On the other hand, for x=0, this material forms an ordered superstructure with composition Ba_8Ge_{43}, with three vacancies on the 6c site, arranged in a helical path along the [100] directions [93, 115]. For low Al concentration we may thus expect to observe this behavior.

A series of two studies were done to understand the Al effect in these materials. The first study corresponds to a purely computational work combined with NMR work from our research group. The second included experiments in conjunction with first principles calculations in order to further address vacancy formation and energetics.

1. Al Local Environment in $Ba_8Al_xGe_{46-x-y}\square_y$

In the NMR measurements of Weiping Gou [104] it was identified that there are two distinct local Al environments in the case of $Ba_8Al_{12}Ge_{34}$, and only one for

$Ba_8Al_{16}Ge_{30}$. To understand this behavior and the appearance of vacancies a series of *ab initio* computational studies were done on type-I $Ba_8Al_xGe_{46-x}$.

a. Computational Results and Discussion

For this first study I considered 33 distinct superstructures having different atomic arrangements, starting with atomic positions of the reported parent $Ba_8Ge_{30}Al_{16}$ structure [116]. Where justified by initial results we also used WIEN2k to minimize internal structural parameters before finalizing the results.

The 10 configurations considered for $Ba_8Ge_{30}Al_{16}$ are summarized in Table XI, where the first three columns indicate the number of Al atoms per cell in each framework site of the parent $Pm\bar{3}n$ structure, and the fourth shows the number of adjacent Al-Al pairs per cell. For these superstructures we retained the cubic cell symmetry, leaving 54 independent atoms ($P1$ space group), except for a few cases allowing higher symmetry. 8 of the configurations are the same as considered in reference [97] for $Ba_8Ga_{16}Ge_{30}$, while in reference [117] a 3-4-9 configuration was considered, similar to the structure determined for $Ba_8Si_{31}Al_{14}$ [118].

Computed NMR lineshapes could be distinguished by the shapes of the non-central portions of the lines, and we found that Al atoms situated in Al-Al pairs contributed the largest EFG's. For configurations with 3 or more Al-Al pairs this led to broad simulated lines providing poor agreement with the data. Thus we ruled out configurations with larger numbers of Al-Al pairs, a feature that is very difficult to determine via diffraction experiments. These configurations also had the highest energies; column 5 of Table XI shows computed total energies per formula unit after parameter optimization, relative to the most stable configurations. Note that in this case only the internal parameters were optimized, leaving identical lattice constants. The last four configurations were not optimized due to the long required computing

Table XI. Al framework occupation used in calculations of $Ba_8Al_{16}Ge_{30}$, per formula unit, along with the number of Al-Al neighbor pairs per cubic cell, χ^2 from the lineshape simulation, and the relative calculated energies per formula unit. Reprinted table with permission from [98] © (2009) by the American Physical Society.

$6c$	$16i$	$24k$	Al-Al	χ^2	Energy (eV)
3	1	12	0	2.9	0.00
3	3	10	0	2.3	0.60
3	4	9	1	8.0	0.00
3	4	9	2	1.6	1.03
4	2	10	2	5.5	1.28
5	3	8	4	6.4	2.31
4	6	6	3	3.6	–
5	1	10	7	5.4	–
6	4	6	5	4.6	–
6	0	10	10	3.9	–

time, however the default parameters gave poor fits and relative energies greater than 2 eV, while for other configurations optimization produced small changes in computed lineshapes and in total energy (typically 0.2 eV).

Fig. 23 shows several simulations compared to the Al_{16} spin-echo spectrum. The two valleys immediately adjacent to the central line are experimental artifacts. Among structures considered, 3-4-9-2 provided the best agreement, while the 3-3-10-0 and 3-1-12-0 also produced acceptable fits, the four numbers referring to the Al site occupations and number of Al-Al pairs, as shown left-to-right in Table XI. In the simulations an identical distribution of isotropic shifts was added to all sites, corresponding to the breadth of the central line, and representing a Knight shift distribution as evi-

denced by the T_1 measurements. Additional center-of-mass shifts for each site due to the second-order quadrupole effect are relatively small; such shifts are responsible for the just-discernible frequency differences between curves in the inset of Fig. 23. The only other parameter used was a single overall amplitude adjustment, the same for each configuration, to make the calculated central lines match the experiment. This produced a good match for the entire lineshape, with the 3-4-9-2 simulation falling particularly close to the data. The sum of square differences between the data and each fit provide an indication of the goodness of fit, as shown by the χ^2 (Table XI). Note that NMR, as a local probe, is much less sensitive to widely spaced defects and surface effects that, for example, transport measurements. This can explain why the fitting based on computed results for perfect single crystals can work well for polycrystalline samples.

Although 3-4-9-2 provided the best fit, 3-1-12-0 and 3-4-9-1 had nearly equivalent total energies that were the lowest calculated for Al_{16} configurations. Of these, 3-1-12-0 was also the minimum energy configuration identified in reference [97] for $Ba_8Ge_{30}Ga_{16}$, featuring a regular pattern of alternating Ge and group III atoms around each six-sided ring of the larger cages. Given its equivalent energy in our results, we would expect the 3-4-9-1 configuration to predominate at the growth temperature due to its greater configurational entropy. Yet, this configuration yielded a distribution of EFG's too small to agree with the NMR lineshapes. Instead, 3-4-9-2, with one additional Al-Al neighbor pair, was among the best fitting. (3-4-9-0 can also be formed, and it seems likely that its calculated energy would be lower than either 3-1-12-0 or 3-4-9-1, but presumably with a poor fit to the NMR.) The 3-4-9-x configurations are in line with the general framework occupation rules established in reference [113] from neutron scattering, and also consistent with our powder XRD refinement. Thus according to our results 3-4-9-2 is the best representation of the

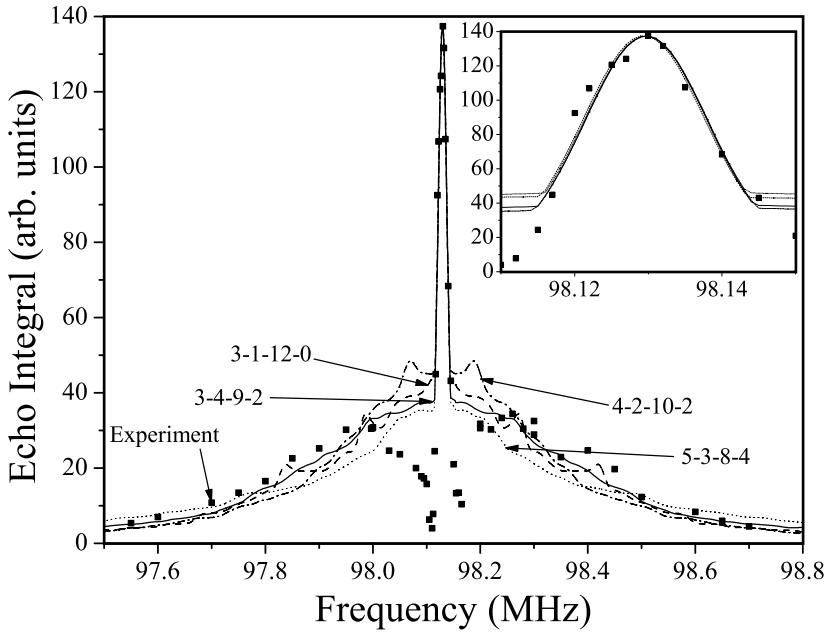

Fig. 23. Simulated NMR spectra for several $Ba_8Al_{16}Ge_{30}$ configurations, together with spin-echo spectrum measured at 4 K. Inset: expanded view of the central-transition region. Reprinted figure with permission from [98] © (2009) by the American Physical Society.

alloy configuration; it has more Al-Al pairs than energetically favored, although the difference is small and it is possible that entropic processes or incomplete equilibration may enhance the likelihood of this configuration.

Bandstructures for Al_{16} configurations 3-1-12-0 and 3-4-9-2 are shown in Fig. 24 (a) and (b). Both are semiconducting, and the latter is in general agreement with a previously report [117]. Our results for 3-4-9-1 and 3-4-9-2 are almost identical. The three-fold minimum at M is nearly isotropic, with an effective mass 1.93 m_e for 3-1-12-0 (2.35 m_e for 3-4-9-2). Decomposing the calculated density at this minimum inside the muffin-tin spheres, we find average Al s-partial contributions of 0.16%/0.18% for 3-1-12-0/3-4-9-2 (percentages relative to the entire 54-atom cell). In the effective mass approximation, the Pauli susceptibility (χ_p) can be calculated for a given electron

density, since it is proportional to the density of states[119]. Assuming conduction electrons introduced extrinsically through the presence of electronically active defects, we can thereby obtain the corresponding Knight shift using

$$K = \frac{\chi_p V_{cell} f_{\mathrm{Al}s} H_{HF}}{\mu_B}, \tag{5.3}$$

where $f_{\mathrm{Al}s}$ is the calculated partial s fraction on a given Al site, and H_{HF} is the s-hyperfine field, taken to be 1.9 MG [72]. Taking the average central-line shift at room temperature (0.0375%) to be a Knight shift, the computed results yield $n = 1.1 \times 10^{21}$ cm^{-3} for 3-1-12-0, corresponding to a small degenerate carrier pocket. 4.1×10^{20} cm^{-3} is calculated for 3-4-9-2. The calculated carrier densities are in the same range as those found for as-grown $Ba_8Ga_{16}Ge_{30}$ and $Sr_8Ga_{16}Ge_{30}$ [29], typically attributed to small departures of the framework composition from the ideal semiconducting materials. Note that Eqn. 5.3 will be valid only if enough carriers are present to reach the degenerate regime, which can be verified for the densities found here. This result is also consistent with the observed positive temperature coefficient of resistivity as will be described in the next section. The wide-line NMR fits, which are dominated by the EFG's, will be affected very little by the small density of such carriers. Also while these shifts are metallic, it is not unreasonable that the Zintl concept may still apply, since the carrier densities are small and thus the departure from the semiconducting configuration are small.

In addition to the average shift, the range of calculated partial densities on individual sites is large and can also account for the measured NMR line broadening. This is shown in Fig. 25, where by superposing lines for each Al site shifted according to its calculated $f_{\mathrm{Al}s}$ (with a single vertical scaling parameter) we obtain an inhomogeneously broadened line with a slightly larger intrinsic width than the measured central line. Results for 3-4-9-2 are similar with a larger width approximately twice

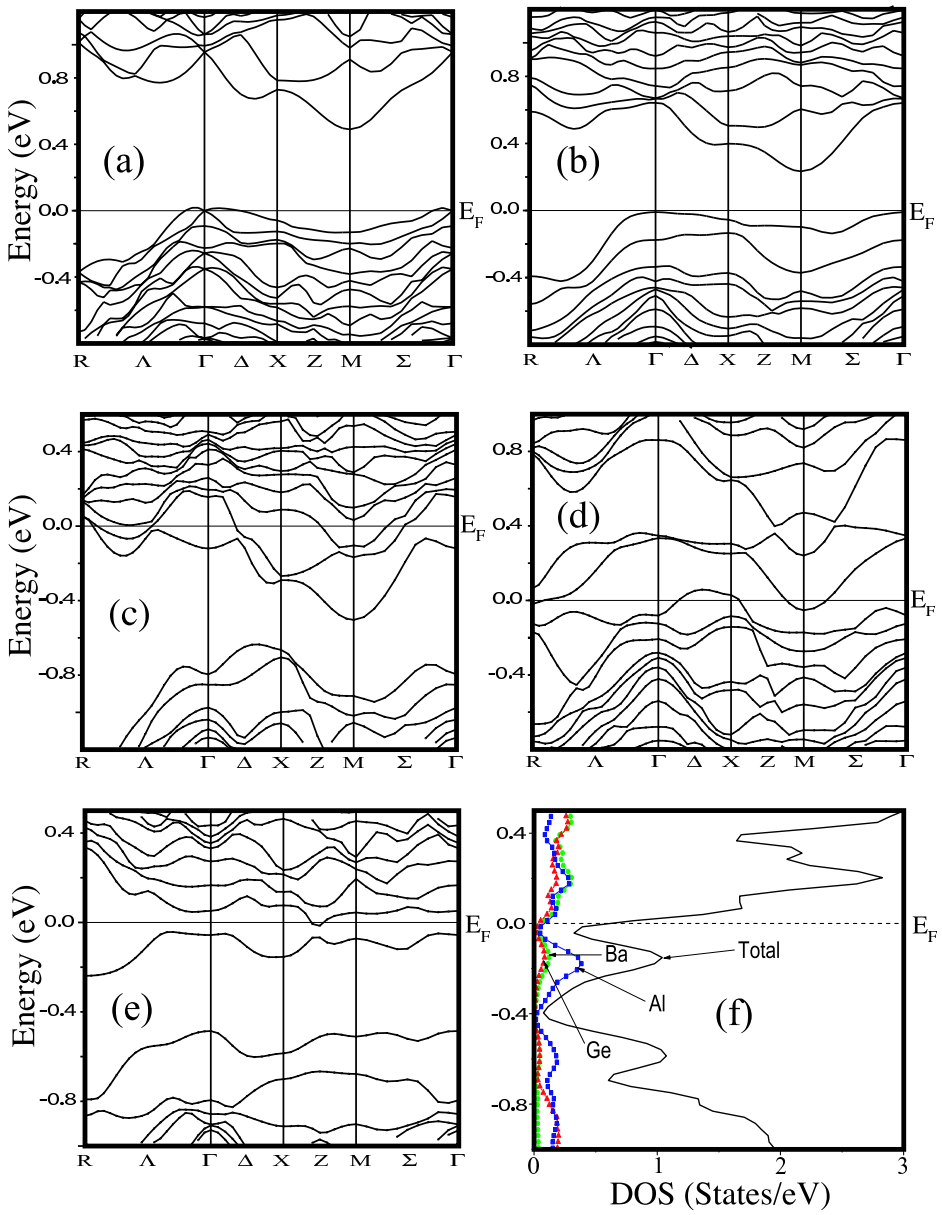

Fig. 24. Calculated electronic bandstructures for Ba-Al-Ge clathrate configurations. (a) and (b): Bandstructures for $Ba_8Al_{16}Ge_{30}$, 3-1-12-0 and 3-4-9-2 respectively, notation as defined in text; (c), (d), (e): Bandstructures for $Ba_8Al_{12}Ge_{34-y}\square_y$, $\square_0$ 4-8-0-0-0, $\square_1$ 4-8-0-0-0, and $\square_1$ 0-0-12-0-2 configurations respectively. (f): Density of states for the latter, including partial densities for Al adjacent to a vacancy, Ge (6*c*), Ba (2*d*), and the total scaled by 1/10. Reprinted figure with permission from [98] © (2009) by the American Physical Society.

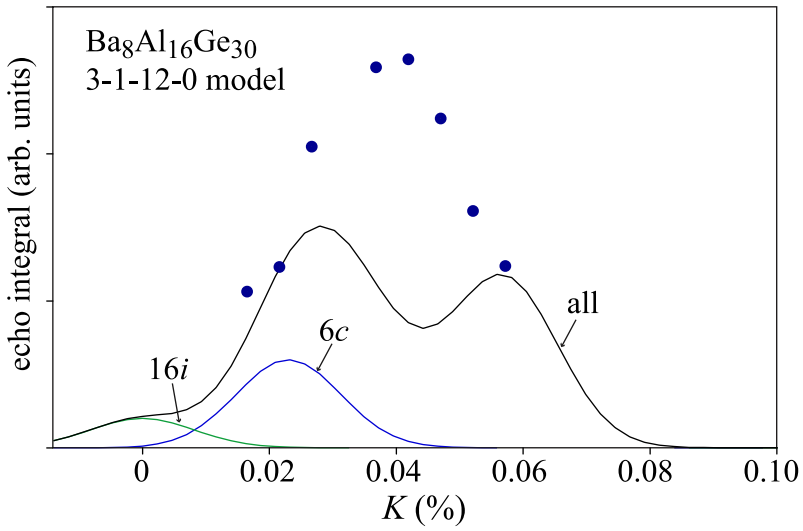

Fig. 25. Calculated NMR line shape from computed Knight shifts for 3-1-12-0 configuration, with carrier density 1.1 $\times$ 10^{21} cm^{-3}, compared to Al_{16} room-temperature data (filled circles). Calculated 6*c* and 16*i* portions are as indicated; remainder due to 24*k* sites. Reprinted figure with permission from [98] © (2009) by the American Physical Society.

that of the data. The detailed shape, with two main peaks, is not representative of the data, indicating that the calculated superstructures are only approximations to the alloy configuration, however clearly the width of the observed NMR line is an indication of the large variation of conducting states among local atomic configurations in the alloy.

In modeling the Al_{12} alloy we considered the 16 superstructures summarized in Table XII. The expected Al_{12} Zintl composition is $Ba_8Ge_{31}Al_{12}\square_1$, however for a nominal Al_{10} composition we found more vacancies than expected in initial WDS scans, so in this work we considered a range of vacancy concentrations. In all cases, vacancies were placed only on 6*c* sites, shown to be the preferred site for vacancies in the type-I structure [120, 43, 42].

Several calculated spectra are shown in Fig. 26, along with the Al_{12} spin-echo

Table XII. Configurations considered in calculations of $Ba_8Al_{12}Ge_{34-y}$. Number of framework vacancies, Al framework occupations, number of Al-Al pairs and number of Al adjacent to vacancies are given per formula unit. Calculated lattice constant and relative formation energy, per formula unit of $Ba_8Al_{12}Ge_{34}$, given for minimized configurations. Reprinted table with permission from [98] © (2009) by the American Physical Society.

vacancy	6*c*	16*i*	24*k*	Al-Al	Al-vac	*a* (Å)	Energy (eV)
$\square_0$	4	8	0	0	0	11.01	0.00
$\square_1$	4	8	0	0	0	11.01	0.22
$\square_1$	4	4	4	0	2	10.99	1.85
$\square_1$	4	3	5	1	5		
$\square_1$	4	2	6	1	5		
$\square_1$	0	0	12	0	0	10.97	1.08
$\square_1$	0	0	12	0	1	10.98	1.08
$\square_1$	0	0	12	0	2	10.97	1.30
$\square_1$	0	0	12	1	4	10.98	1.98
$\square_2$	4	8	0	0	0	10.84	1.86
$\square_2$	4	4	4	0	2		
$\square_2$	4	0	8	0	8		
$\square_2$	4	3	5	1	5		
$\square_2$	4	2	6	1	6		
$\square_2$	0	0	12	2	4	10.97	3.56
$\square_3$	0	0	12	0	6	10.95	5.03

spectrum. The $\square_1$ 0-0-12-0-2 and $\square_3$ 0-0-12-0-6 configurations (notation corresponding to first 6 columns of Table XII) provided a good fit, while other configurations agreed poorly. The large difference between calculated spectra was due most significantly to the large EFG for sites adjacent to a vacancy, ranging from $\nu_q = 1000$ to 2800 kHz. Normalization was similar to that of the Al_{16} curves, with a single overall scaling used to force agreement in the central-line region. However, because of the two-peaked central line, two distinct isotropic shifts were applied, with a portion of the sites having a larger shift than the others, plus an additional overall broadening function applied to the otherwise relatively narrow computed central-line. The shift distribution has almost no effect on the broad non-central region of the lines, and thus does not affect the fitting except for the appearance of the central line. We will return to consider a more detailed calculation of the Knight shift distribution below.

Calculated total energies and lattice constants are shown in Table XII for minimized configurations. In the formation energies we added the all-electron total energy per atom for diamond-structure Ge, after volume minimization using the same GGA-PBE formalism, to compensate for each vacancy. Configurations not minimized had simulated spectra differing significantly from the data and relative energies greater than 2.5 eV before minimization. There are a number of configurations relatively close in energy, however a general trend is seen with a preference for zero or one vacancy. Of the two configurations best fitting the NMR spectra, $\square_3$ 0-0-12-0-6 has a considerably higher calculated energy, while $\square_1$ 0-0-12-0-2 is energetically more favored and has the expected single-vacancy Zintl composition, thus provides a likely explanation for the data. This configuration also agrees with the trend from our XRD fits indicating Al occupation transferred to $24k$ sites as the Al concentration is reduced. (Note, however, that this trend does not continue over a wider range of Al concentration, as shown in the next section.)

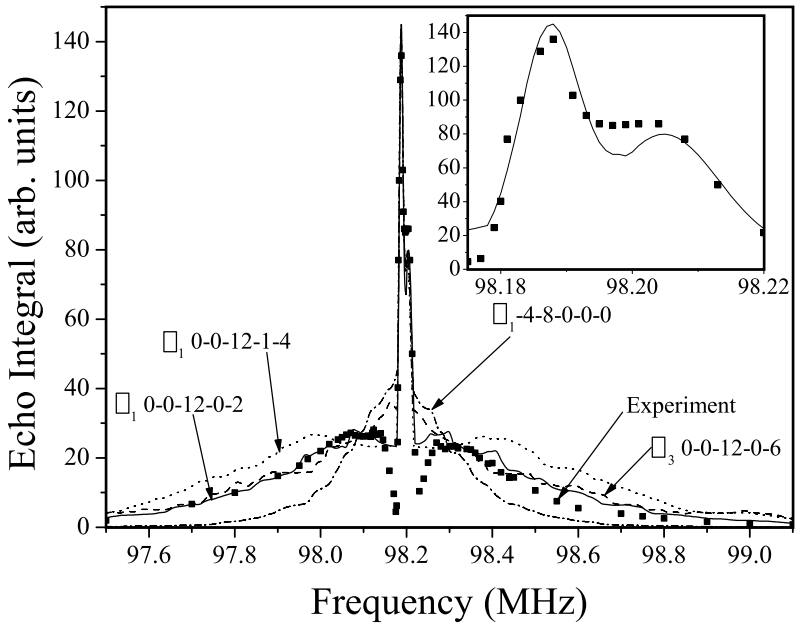

Fig. 26. Simulated NMR lines for several configurations of $Ba_8Al_{12}Ge_{34-y}$ together with spin-echo NMR lineshape. Inset: expanded view of the central transition region, with calculated spectrum only for $\square_1$ 0-0-12-0-2 configuration. Reprinted figure with permission from [98] © (2009) by the American Physical Society.

Compared to the best-fitting $\square_1$ 0-0-12-0-2, other configurations have lower energy:$\square_1$ 4-8-0-0-0 is 1.1 eV/cell lower in energy and is the most stable calculated one-vacancy configuration. Filling the vacancy with Ge yields $\square_0$ 4-8-0-0-0 with a still lower energy, although the additional vacancy-formation entropy of the $\square_1$ configuration may negate the small difference. Yet none of the 4-8-0-0-0 simulations agree with the NMR data; the $\square_1$ simulation is shown in Fig. 26, and that of $\square_0$ is similar, both having EFG's too small.

Bandstructures for some of these configurations are shown in Fig. 24. From the calculated densities of states for the $\square_1$ 0-0-12-0-2 configuration (Fig. 24(f)) we can calculate the site-dependent Knight shift, using Eqn. 5.3, with the local susceptibility taken from the local Fermi-level density of states, using a similar method as used

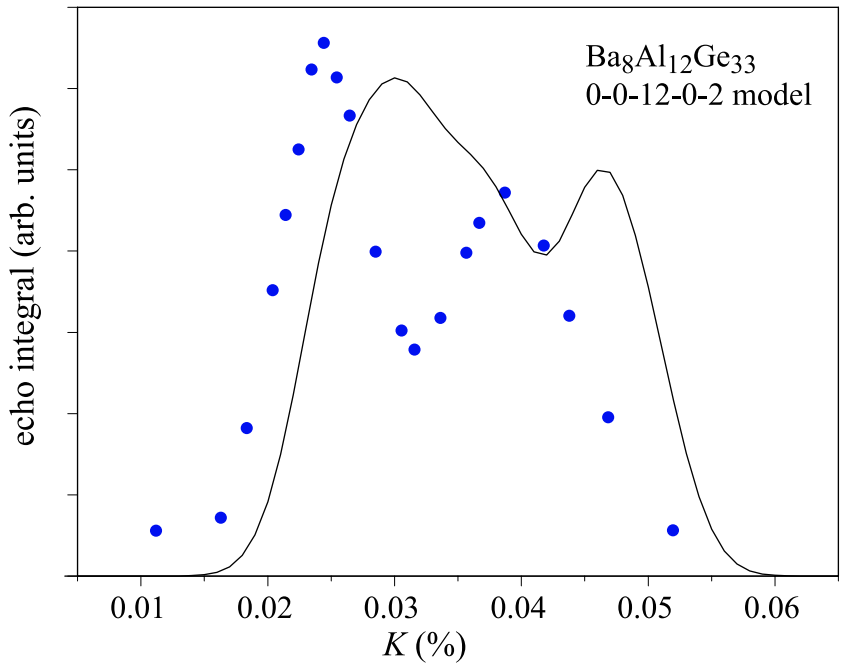

Fig. 27. Calculated NMR line shape (solid curve) from computed Knight shifts for $\square_1$ 0-0-12-0-2 configuration, compared to Al_{12} room-temperature data (filled circles). Reprinted figure with permission from [98] © (2009) by the American Physical Society.

for the Al_{16} calculation. The result is shown in Fig. 27 as the solid curve, obtained by superposing a line for each of the 12 calculated Knight shifts, with an identical Gaussian broadening given to each line. Note that in contrast to the Al_{16} case, for which a small carrier density was added to the otherwise insulating configuration, for this case there are no adjustable parameters, save for a vertical scaling. The calculated peak at the right edge is due to the two Al sites adjoining a vacancy in this configuration, for which the local charge density is larger. Overall, the calculated shifts are larger than observed, although it is possible that the pseudogap at E_F might become deeper, and hence the shifts smaller, if not for the well-known tendency for band-gap underestimation in the PBE-GGA method. Thus the agreement seems quite reasonable.

While the calculated $\square_1$ 0-0-12-0-2 configuration is not semiconducting, E_F falls between bands over much of k space (Fig. 24). In this way, this configuration might be considered to satisfy the Zintl criterion, in which a semiconductor would be expected, with a hybridization gap at E_F. From the partial density of states [Fig. 24(f)] it can be seen that contributions from the two Al vacancy neighbors dominate the highest filled band, making up the peak just below E_F, far outweighing contributions from any other site; the sites with the largest Ge and Ba contributions in this region give the two additional curves also plotted in Fig. 24(f). It is thus apparent that the associated states are largely non-bonding hybrids adjoining the vacancy. The concentration of such states for this band explains the larger Knight shift for such Al sites, and hence the observed split-off central peak.

Having minimized the internal parameters for a number of configurations, we can also address the atomic displacements which are of potential significance for thermoelectric applications. In Al_{16}, calculated Ba displacements from symmetry positions are very small even for 6d atoms identified through diffraction experiments as having distorted nuclear density profiles [113], and which exhibit a low-energy "rattling" mode [117]. In the 3-4-9-2 configuration, the largest calculated Ba 6d displacement is 0.019 Å. Of the six optimized Al_{16} structures, no Ba 6d was more than 0.07 Å from the cage center, and the overall average displacement was 0.025 Å. Also the longest framework bonds appeared in structures having Al-Al neighbors, for example in the 3-4-9-2 configuration the Al-Al bonds increased to 2.61–2.77 Å, compared to the Ge-Ge bond lengths of 2.51–2.53 Å; this reflects the weakness of the Al-Al bond. Calculated Ba 6d displacements are consistently smaller that the experimental values [113]. The calculated results do not include dynamical terms, and also may reflect a balance between opposing tendencies for different growth conditions, for which displacements tended toward perpendicular crystal directions [113], presumably due to

different dominant defect types. For Al_{12} configurations with vacancies, the calculated structural distortions are considerably larger; all framework atoms next to the vacancy shift toward the open space (by 0.35 to 0.55 Å), while the four Ba 6*d* sites in cages including the vacancy shift toward the 24*k* framework sites (Ge or Al) immediately adjacent to the vacancy. This decreases the Ba 6*d*-(Ge/Al)24*k* bond length from 3.64 Å to 3.39–3.43 Å. This is not quite as short as the sum of the covalent radii (3.35–3.36 Å), however it is clear what develops is a much more localized covalent bond involving the atoms adjacent to the vacancy.

As described in the last section, NMR combined with *ab initio* computational studies was also used with success in exploring the local configuration of type-I $Ba_8Ga_{16}Sn_{30}$ clathrates. The results demonstrate opposing trends for Ga-Ga as Al-Al framework bonding, which we showed to be related to differences in the energies of the corresponding configurations. For the Ba-Al-Ge clathrates described here, we found a good match between energetically formed configurations and those that best fit the NMR data, thereby also providing new information about the local electronic and structural configurations in these alloys.

2. $Ba_8Al_xGe_{46-x-y}\square_y$ Vacancy Formation

For a further study of the Ba-Al-Ge system, I studied $Ba_8Al_xGe_{46-x-y}\square_y$ alloys, for $4 \leq x \leq 16$, where $\square$ represents a vacancy, to better understand the Al preferential site occupation and vacancy occurrence. These studies examined changes in electrical and transport properties, as well as in the composition and structure vs. x. In addition first principles calculations were carried out to examine the deficit of framework occupation observed in these samples. These calculations examined local variations in electronic behavior as the Al composition was varied and vacancies formed.

a. Sample Preparation

Several samples of nominal composition $Ba_8Al_xGe_{46-x}$ with $4 \leq x \leq 16$ were prepared from the pure elements mixed according to the desired compositions, and arc melted in argon following by annealing at 900 °C for 100 hours. This procedure is slightly different than the one used for the materials in the previous section, synthesized by Weiping Gou [104]. The higher annealing temperature lead to a better stability of these materials. Five different samples with stoichiometric starting compositions $x = 4$, 8, 12, 14 and 16 were prepared for the studies described here.

b. Experiment

XRD measurements at room temperature were performed using a Bruker D8 X-ray Powder Diffractometer, with Rietveld refinement performed using EXPGUI [60]. WDS measurements were done in a Cameca SX50 equipped with 4 wavelength-dispersive X-ray spectrometers. Four probe resistivity measurements were performed using a Quantum Design Physical Property Measurement System from room temperature to 2 K.

Table XIII. Number of atoms and vacancies per unit cell obtained by WDS measurements for $Ba_{8-z}Al_xGe_{46-y}$. Reprinted table with permission from [121]

Sample	Ba	Al	Ge	# of vacancies
4	8	4.10	39.60	2.3
8	8	7.37	37.12	1.5
12	7.91 ± 0.09	9.00	35.82	1.2 ± 0.5
14	7.84 ± 0.10	11.15	34.29	0.6 ± 0.6
16	7.83 ± 0.03	14.28	31.54	0.2 ± 0.2

Samples are denoted here by Al_x according to the starting compositions, for example Al_{16} representing $Ba_8Al_{16}Ge_{30}$, although the actual configuration is as given in Table XIII. From WDS and XRD measurements we find that for Al_8 and Al_{16}, the samples are type-I clathrates with an additional small amount of diamond structure Ge. In the Al_{12}, and Al_{14} samples an additional minor phase was seen, apparently an oxide of Ba and Al. Finally the Al_4 sample also exhibited superstructure reflections identical to those of $Ba_8Ge_{43}\square_3$ with its ordered vacancy configuration [93, 115]. From WDS measurements all the samples showed a lower Al concentration than the expected stoichiometric compositions.

In scans of our samples by WDS we scaled the clathrate-phase atomic percentages to obtain the total number of Ba, Al, and Ge atoms per cell. In the case of Al_4 and Al_8 we set the Ba sites to be completely full. For Al_{12}, Al_{14} and Al_{16} it was not possible to have complete Ba site occupation, and thus we found a range of possible Ba, Al, and Ge concentrations. The upper bound was determined by full framework occupation, and the lower bound following an electron balance according to the theoretical Zintl concept. The center value corresponded to a smooth variation of the WDS scaling

Table XIV. Al framework occupation per cell obtained by XRD measurements at 300 K for $Ba_{8-z}Al_xGe_{46-y}$, along with the lattice constant, and the goodness of fit parameters. Reprinted table with permission from [121] © (2010) by the American Physical Society.

Sample	$6c$	$16i$	$24k$	a(Å)	WR_p	R_p
4	0.86	1.62	0.80	10.716	0.1793	0.1201
8	1.20	1.00	4.99	10.760	0.1933	0.1306
12	1.99	3.73	5.92	10.787	0.1873	0.1369
14	3.18	0.77	7.97	10.821	0.1449	0.1088
16	3.01	2.66	10.22	10.849	0.0473	0.0359

factor. The results are summarized in Table XIII.

From XRD measurements, as described above we found that for Al_8 and higher there were only type-I reflections. The data obtained from Rietveld refinements are summarized in Table XIV. Lattice constants gradually decreased from 10.849 Å for Al_{16} to 10.716 Å for Al_4. For Al_{16} the obtained value is similar to the values reported by Christensen *et al.* [113], for various growth techniques. Al_4 exhibits a symmetry similar to that of the defect clathrate $Ba_8Ge_{43}\square_3$ where there are extra peaks in the XRD spectrum due to ordering of vacancies. In this case the symmetry is changed from the ideal type-I clathrate structure ($Pm\overline{3}n$) to a ($2\times2\times2$) cubic superstructure having symmetry ($Ia\overline{3}d$) [43]. The Rietveld refinement in this case was done for the superstructure ($Ia\overline{3}d$), and the Al content was given by a sum of the respective type-I parent sites. The lattice constant was divided by 2 to compare with the type-I structures.

Combining the results from XRD and WDS measurements, the lattice constant shows a linear behavior as a function of Al substitution for low Al concentration, as

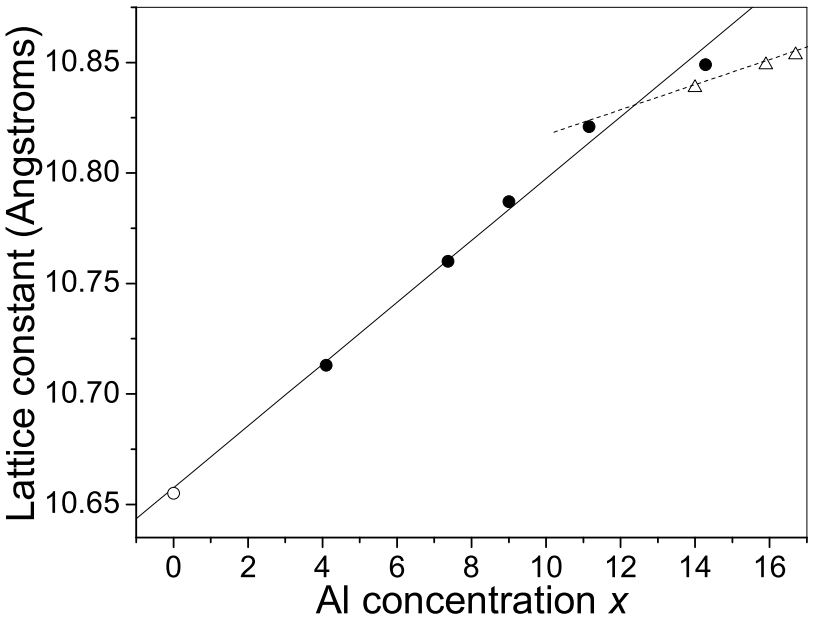

Fig. 28. Lattice constant as a function of Al doping. Filled circles correspond to our measured samples. Hollow circle is the reported value for Ba_8Ge_{43}, and hollow triangles correspond to samples measured. Straight lines correspond to linear fits described in text. Reprinted figure with permission from [121] © (2010) by the American Physical Society.

shown in Fig. 28, where the solid line is a linear fit to low Al content samples. The hollow circle is the reported value for Ba_8Ge_{43} [43]. This reported value is in close agreement with a linear extrapolation to zero Al content. The hollow triangles are the values reported by Christensen *et al.* [113]. In this case the high Al content values appear to go over to a different slope compared to those for low Al content. The dashed line corresponds to a linear fit to the values reported by Christensen [113] and our two highest Al content samples.

The Al occupation of framework sites obtained from XRD on Al_{16} (Table XIV) follows closely the relationship from our fit to the NMR data for Al_{16}, described in the previous section [98], where the best description of the NMR lineshape was for a

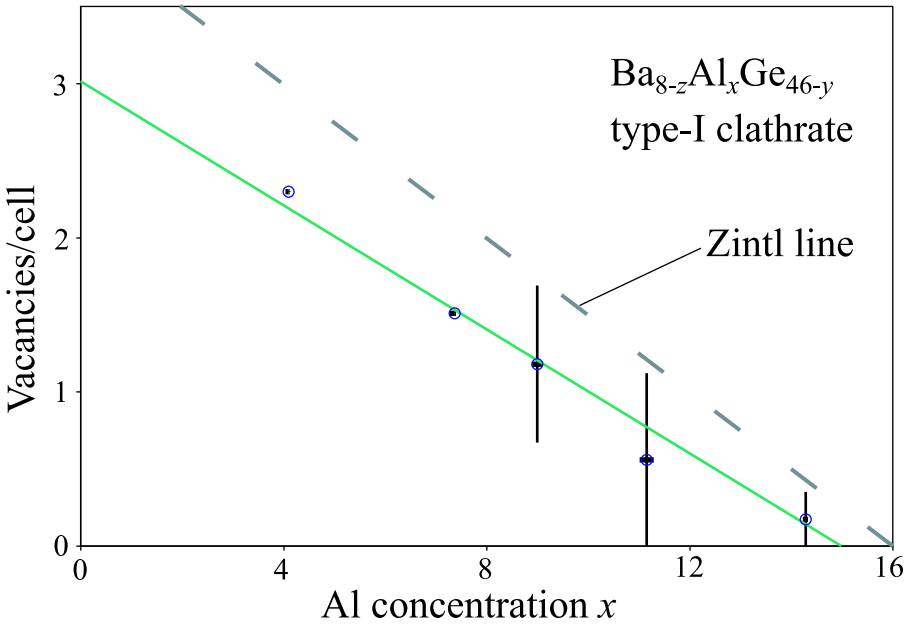

Fig. 29. Number of vacancies obtained experimentally as a function of Al doping. Continuous line is a linear fit to the data. Zintl line is also included as a reference. Horizontal and vertical error bars as described in text. Reprinted figure with permission from [121] © (2010) by the American Physical Society.

configuration of 3, 4, and 9 Al on the 6*c*, 16*i*, and 24*k* sites, respectively. These are close to the values obtained from Rietveld refinements in the new sample.

A feature of $Ba_8Al_xGe_{46-y}$ is the occurrence of spontaneous vacancies to balance the electron count in the framework, according to the Zintl concept [122]. For example, for Al_{12} the theoretical Zintl composition is $Ba_8Al_{12}Ge_{33}\square_1$, since if each Ba donates two electrons and Al has valence 3, there are four excess framework electrons per cell after filling all bonds, enough to fill the nonbonding orbitals adjoining a single vacancy. The expected result is a semiconductor or low-carrier density material. For $Ba_8Al_{16}Ge_{30}$ one expects a balanced framework electron count and no spontaneous vacancies, while as the Al content decreases the vacancy count should increase, the limiting case being the ordered superstructure $Ba_8Ge_{43}\square_3$. However, the latter composition does not correspond to a Zintl compound because it exhibits one less vacancy

than expected. For comparison in $Ba_8Ga_xGe_{46-y}$ the vacancy count was determined experimentally to be about half the expected Zintl value over a range of compositions [115].

The variation of vacancy count as a function of Al concentration is shown in Fig. 29. The number of vacancies per cell varies from 0.3 for Al_{16} to 2.3 for Al_4. A straight-line fit extends from 3.0 vacancies for $x = 0$ to 0 vacancies at $x = 15.0$. Thus the vacancy count smoothly approaches a limiting value equivalent to that of Ba_8Ge_{43}. The uncertainty in vacancy count is relatively large for large x, even though the uncertainty in x (horizontal bars) is small. However the values connect smoothly to those for low x, and remain below the theoretical Zintl line.

In resistivity measurements we studied polycrystalline bars cut from ingots, with lengths between 3 and 6 mm. All samples exhibited positive temperature coefficients, typical of metals or heavily-doped semiconductors, with, for example, Al_{16} having a low-temperature value of 376 $\mu\Omega$-cm, within the range observed previously for $Ba_8Al_{16}Ge_{30}$ samples [113]. As the number of Al decreases the resistivity diminishes. For Al_4 the low temperature values are similar to those reported for Ba_8Ge_{43} [123, 101], but Ba_8Ge_{43} has a steeper slope, so that at room temperature the resistivity for Ba_8Ge_{43} is almost 5 times larger [123, 101]. The behavior *vs* Al content matches the expected behavior for increased deviation from Zintl behavior thus increasing carrier density with decreasing x as shown in Fig.30(a). The solid curves are fits to the data assuming a Bloch-Grüneisen function for pure electron-phonon scattering [124], for which the fitted values of the Debye temperature are 380 K for Al_{16} and Al_4, and 330 K for Al_8. In limited modeling in the BoltzTraP routine based on *ab initio* electronic structures, we have obtained some results reproducing the small anomalous upturns in resistivity at low temperatures. This result is apparently tied to changes in carrier mass associated with the narrow electron bands characteristic of these structures.

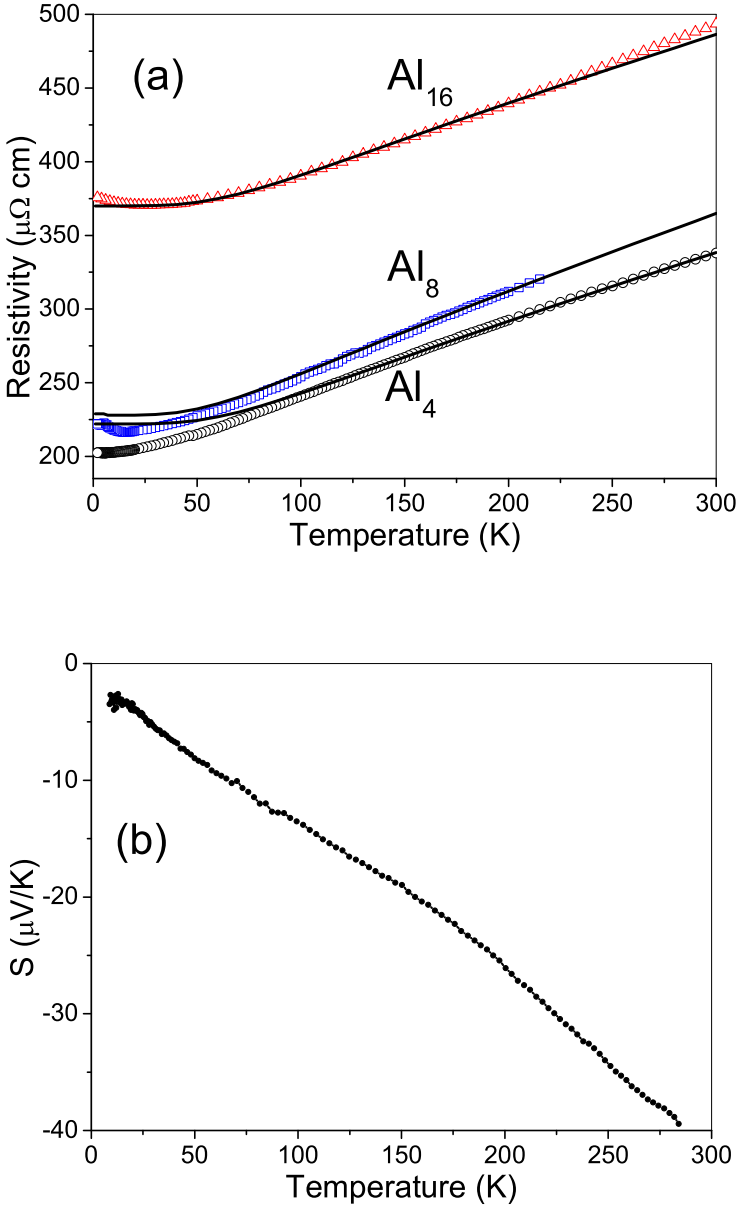

Fig. 30. (a) Resistivity as a function of temperature for Al_4, Al_8 and Al_{16}. Solid curves: Bloch-Grüneisen fits. (b) Seebeck coefficient (S) for type-I Al_{16} sample.

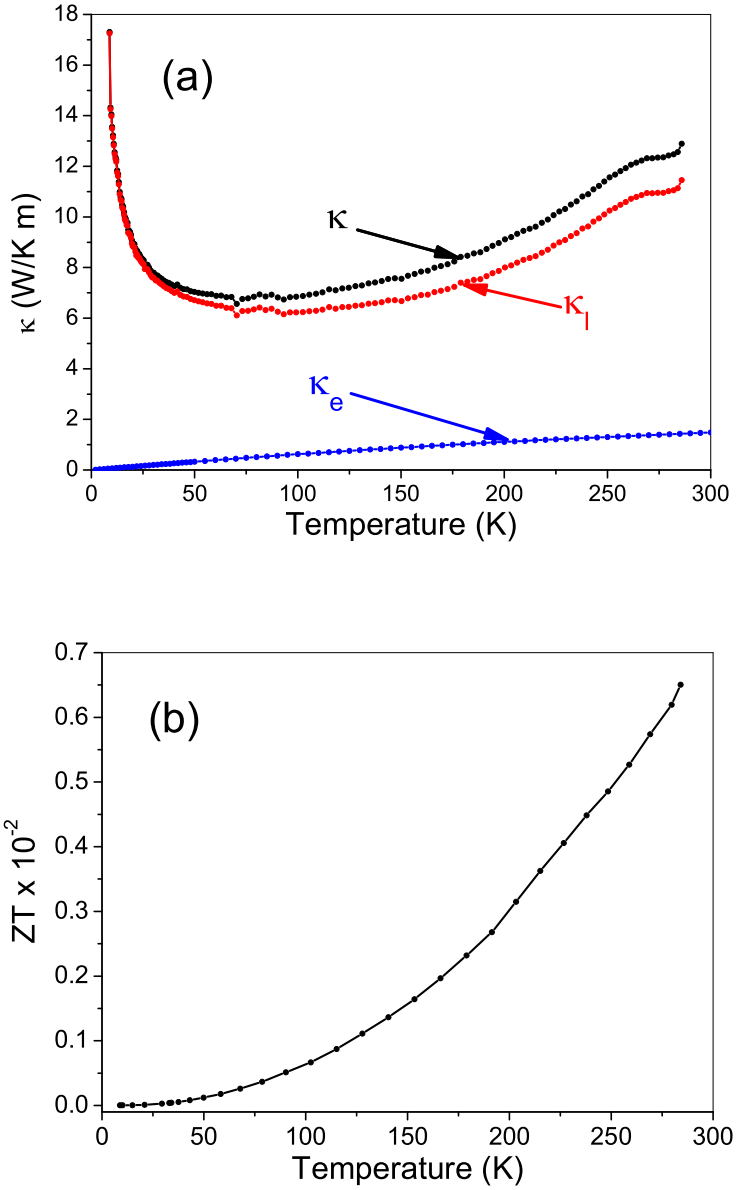

Fig. 31. (a) Total thermal conductivity (κ), together with derived phonon (κ_l) and electron (κ_e) contributions for Al_{16} type-I sample. (b) Thermoelectric figure of merit (ZT) for Al_{16} type-I sample.

However these studies have not yet been carried out in a systematic way, and we have not ruled out other possible mechanisms for this behavior, also observed in some of the Ba-Ga-Sn clathrates.

Thermoelectric properties were measured for the Al_{16} sample. Fig. 30(b) shows S from 285 K to 2 K. The negative S indicates electrons as the majority carriers in the sample. The behavior of this sample is similar to the previous description for type-VIII $Ba_8Ga_{16}Sn_{30}$, also a degenerate semiconductor. The largest absolute value of S at 285 K, of about -40 μV/K, is in agreement with other reports for $Ba_8Ga_{16}Ge_{30}$ samples [35, 106].

Results for the temperature dependent thermal conductivity, $\kappa(T)$, are displayed in Fig. 31(a). $\kappa(T)$ exhibits an increase as the temperature is decreased, similar to the observed behavior in type-VIII $Ba_8Ga_{16}Sn_{30}$ from section D.2.b, and type-I $Ba_8Al_{16}Si_{30}$ [107]. As shown previously for $Ba_8Ga_{16}Sn_{30}$ the total thermal conductivity can be written as $\kappa = \kappa_e + \kappa_l$. The electronic thermal conductivity κ_e was calculated according to the Wiedemann-Franz relationship as for type-VIII $Ba_8Ga_{16}Sn_{30}$ in section D.2.b. The low values in thermal conductivity are associated with the vibrations of the guest atoms inside the cages, allowing them to rattle and dissipate heat. The partial contribution of each component, κ, κ_e and κ_l, are shown in Fig. 31(a). The upturn below 50 K follows a T^{-1} power law behavior, similar to the expected from phonon-phonon Umklapp scattering for crystalline materials, somewhat different than type-VIII $Ba_8Ga_{16}Sn_{30}$ shown in the previous section. It is interesting that in this case, the glassy behavior and large reduction in κ at low temperature is not observed here, as it is for some clathrates such as $Sr_8Ga_{16}Ge_{30}$ [27]. This result appears to indicate that Ba-Al-Ge clathrates lacks the enhanced "rattling" behavior of Sr-Ga-Ge. At low temperatures the anticipated T^3 is not observed up to 9 K, probably due to extremely smooth boundaries. This statement could be reinforced from

backscattered electron images (not shown) where no boundaries can be observed up to 50 μm for $Ba_8Al_{16}Ge_{30}$.

In Fig. 31(b) the dimensionless figure of merit given by $ZT = S^2\sigma T/\kappa$ is shown for type-I $Ba_8Al_{16}Ge_{30}$. As for type-VIII $Ba_8Ga_{16}Sn_{30}$, it remains low over the temperature range mainly because the Seebeck coefficient is below -100 μV/K, and the resistivity is also higher than for type-VIII $Ba_8Ga_{16}Sn_{30}$. On the other hand κ is smaller, but the overall figure of merit is similar to the reported values for $Ba_8Al_{16}Si_{30}$ [107] and $Ba_8Ag_xGe_{46-x-y}\square_y$ [110].

c. Computational Results and Discussion

Ab-initio calculations were done for analysis of the electronic structure and to understand the stability of the different configurations. A linear extrapolation of the measured number of vacancies as a function of Al concentration, for low x, intercepts 0 vacancies for x close to 15 as shown in Fig. 29. This is less than the expected value for the Zintl composition, $Ba_8Al_{16}Ge_{30}$. To study this behavior, we examined a number of filled-framework structures with fewer than 16 Al per cell. In all, I considered more than 16 different superstructures with several framework arrangements, and a range of Al occupation. All superstructures were minimized in volume and internal structural parameters.

Formation energies were obtained from the equation,

$$E_{\rm form}(Ba_8Al_xGe_{46-x}) = E_{Ba_8Al_xGe_{46-x}} - 8E_{\rm Ba} - xE_{\rm Al} - (46-x)E_{\rm Ge}, \qquad (5.4)$$

where x is the number of Al per unit cell. Cases we considered included x =16, 15, 14, and 12. $E_{\rm Ba}$ is the energy per Ba atom in Ba metal, and similarly for the others.

The lowest-energy configurations obtained are summarized in Table XV, where the first column is the total number of Al per unit cell, and the next three columns

indicate the Al framework occupation on the 6c, 16i, and 24k parent sites, and the fifth column is the total calculated formation energy relative to the lowest-energy. The occupation of three Al on the 6c site has been found to be the preferred value from computations as reported for Ba-Al-Ge [98], Ba-Ga-Sn [96], and Ba-Ga-Ge [97] clathrates with the first two been having been described in previous sections. Some configurations with two and four Al on the 6c site (not shown here) were also considered, but their energies were much higher than for those with 3 Al. The number of Al on the 16i site was varied systematically from 1 to 5, with respective changes in the 24k site occupation.

As shown in Table XV we found that among zero-vacancy configurations 3-1-12 was lowest in energy, where the three numbers refer to the first three columns in Table XV. Energies are given relative to that of the 3-1-12 configuration, whose formation energy is -17.9 eV. This is somewhat lower than previously reported for $Ba_8Al_{16}Ge_{30}$ [117], using a different functional. The 3-1-12 configuration was shown above in the previous section to have the lowest energy specifically for Al_{16} configurations, and also for $Ba_8Ga_{16}Ge_{30}$ [97] and $Ba_8Ga_{16}Sn_{30}$ described above in section D [96].

From Table XV it is seen that several configurations are rather close in energy to the 3-1-12 configuration, with the difference between the lowest-energy $x = 16$ configurations appearing hardly significant. The $x = 15$ configuration 3-1-11 has a formation energy roughly 2% higher than that of 3-1-12; this is 0.006 eV per atom, corresponding to a temperature of about 70 K, much less than the growth temperature. Thus though the Zintl $x = 16$ configurations have the lowest computed energies, it appears that n-type $x = 15$ and 14 configurations may readily form with little cost in energy. It is interesting to note that in type-I Ba-Ga-Ge the energy cost for off-Zintl configurations was found to be significantly higher [97] than obtained here for

Table XV. Al framework occupation per formula unit used in calculations of $Ba_8Al_xGe_{46-x}$ clathrates, for configurations with no Al-Al pairs, and the calculated difference of total formation energy per formula unit with respect to lowest energy configuration, 3-1-12. Reprinted table with permission from [121] © (2010) by the American Physical Society.

x	$6c$	$16i$	$24k$	ΔE (eV)
16	3	1	12	0.000
16	3	2	11	0.027
16	3	3	10	0.074
16	3	4	9	0.126
16	3	5	8	0.164
15	3	1	11	0.275
15	3	2	10	0.344
15	3	3	9	0.736
15	3	4	8	0.390
15	3	5	7	0.452
14	3	1	10	0.734
14	3	2	9	0.750
14	3	3	8	0.692
14	3	4	7	0.739
14	3	5	6	0.828
12	3	1	8	1.606

Ba-Al-Ge.

To further examine whether these configurations follow the Zintl prescription, we have calculated their bandstructures. Selected results for $Ba_8Al_{15}Ge_{31}$, $Ba_8Al_{14}Ge_{32}$ and $Ba_8Al_{12}Ge_{34}$ are shown in Fig. 32(b-d). Whereas $Ba_8Al_{16}Ge_{30}$ in minimized configurations is a semiconductor [98], for those with lower x, E_F falls above the gap as expected. The calculated results are close to a rigid band model, with little change in the bandstructure while the Fermi level changes with the Al variation. This is the situation expected in the Zintl model, whereby reduction in x for $x = 16$ corresponds to over-filling of framework electron states. Also the fact that the gap remains below E_F in these results seems to rule out a transfer of fewer than 2 electrons from Ba as a possible explanation of observed non-Zintl compositions.

To compare for low x, we have also calculated the electronic structure for Ba_8Ge_{43} in its reported superstructure configuration. The bandstructure and density of states ($g(E)$) results are shown in Fig. 32(a) and Fig. 33(a), respectively, with good agreement with recent reports [125, 101]. The labeled upper curve in Fig. 33(a) corresponds to the total $g(E)$, the Ba and Ge contributions are also shown. (The total $g(E)$ also includes a contribution from the interstitial regions, in the full-potential LAPW method.) There is also a small gap of approximately 0.1 eV appearing below E_F. The $g(E)$ for the $Ba_8Al_{12}Ge_{34}$ (Fig. 33(b)), $Ba_8Al_{15}Ge_{31}$, and $Ba_8Al_{14}Ge_{32}$ (not shown) lowest-energy structures have a similar overall broad features where the Ba maximum contribution is around 7 eV. The main differences are the band gap and the location of the Fermi level.

Interpreting the small gap in Ba_8Ge_{43} as a boundary between bonding and antibonding states [101], it appears that Ba_8Ge_{43} has an over-filled framework, just as would be expected from an electron-counting argument. Aydemir *et al.* [101] speculated that the incomplete Zintl behavior in Ba_8Ge_{43} is due to a strain desesta-

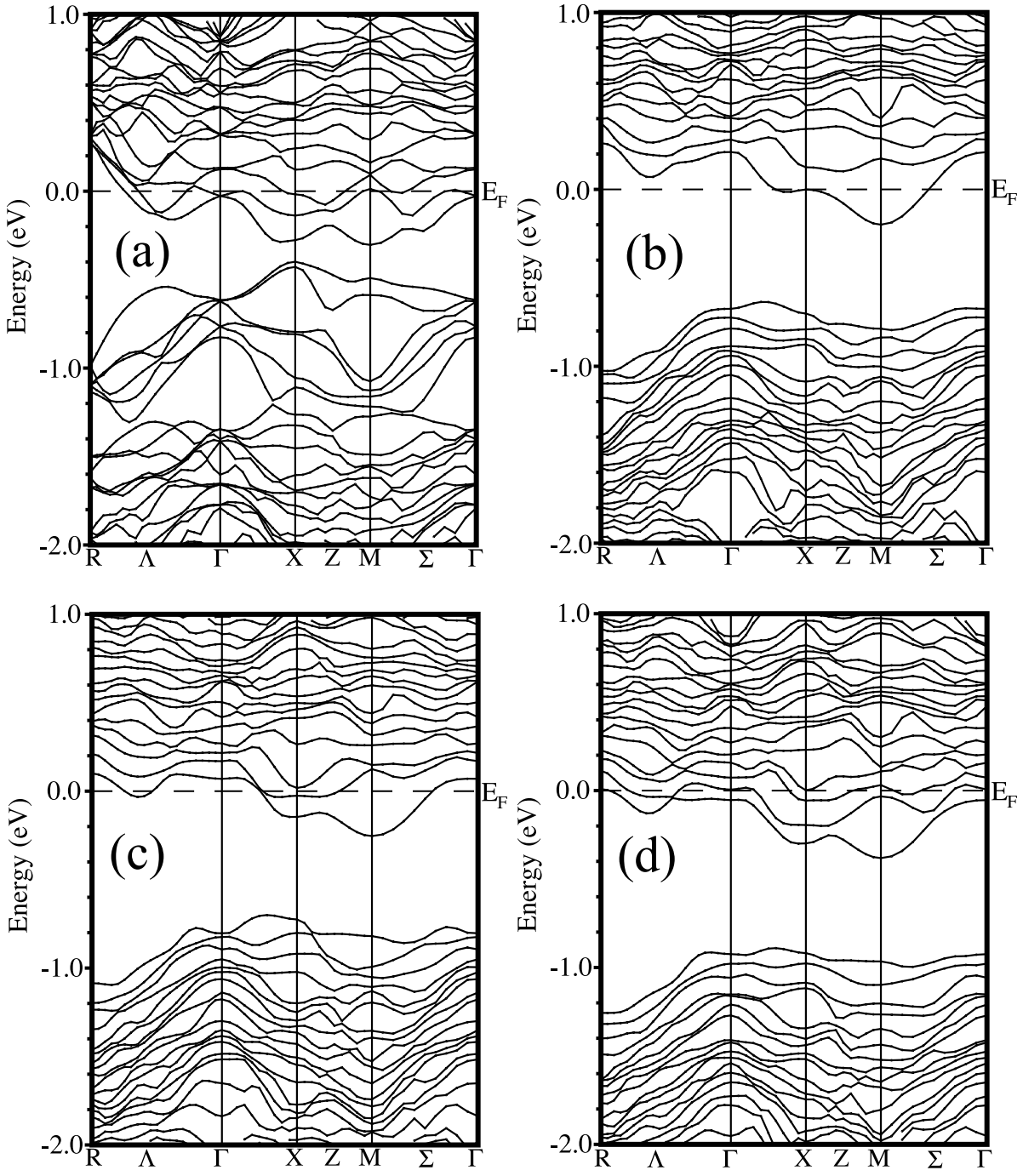

Fig. 32. Calculated bandstructures for (a) $Ba_8Ge_{43}\square_3$ and for the lowest energy configurations of (b) $Ba_8Al_{15}Ge_{31}$, (c) $Ba_8Al_{14}Ge_{32}$ and (d) $Ba_8Al_{12}Ge_{34}$. Reprinted figure with permission from [121] © (2010) by the American Physical Society.

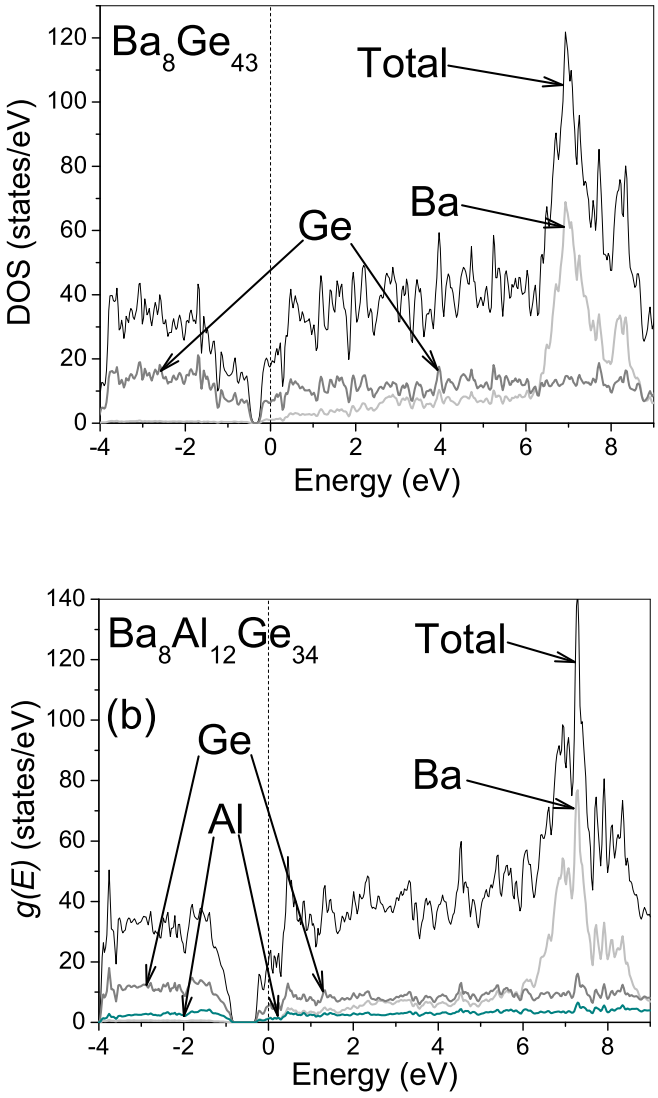

Fig. 33. (a) Total calculated density of states for Ba_8Ge_{43}. (b) Total calculated density of states for $Ba_8Al_{12}Ge_{34}$ in 3-1-8-0 configuration. Reprinted figure with permission from [121] © (2010) by the American Physical Society.

bilization. Their explanation is that the vacancies in the 6c sites might induce excess strain when more than 3 vacancies per cell are present, limiting their number. The superstructure configuration for Ba_8Ge_{43} may indeed be one that minimizes strain by avoidance of nearby vacancies; for example if alternatively attributed to a charge density wave, the period might be expected to differ in the Al_4 sample, with differing charge density. However note that we find the number of vacancies to approach that of Ba_8Ge_{43} smoothly as x decreases (Fig. 28), rather than reaching a plateau at 3 vacancies/cell as would be expected if this were a threshold separating configurations with differing strain energy.

We infer that the reduced vacancy count is due to a competition between the formation energy per vacancy and Zintl stabilization energy. Examining Fig. 33(a) we see that although E_F falls above the bandgap, it falls within a larger pseudogap approximately 2 eV in width. With E_F maintained in this region the number of high-energy occupied states can be kept relatively low while also reducing the number of vacancies that must be formed. Results are similar for other configurations we have calculated; for example in $Ba_8Al_{12}Ge_{34}$ [Fig. 33(b)] although E_F appears above the gap it remains in a region of reduced $g(E)$. Thus we infer that the deviation from Zintl behavior may result from balancing the vacancy formation energy vs. antibond occupation in the framework, across the range of composition. It is interesting to note that by contrast, Ba-Cu-Ge clathrate was shown to agree quite precisely with the Zintl formalism, the difference apparently being the lesser substitution energy for Cu $vs.$ vacancy formation energy.

In Fig. 34(a) the calculated Seebeck coefficient for all the considered configurations in the $Ba_8Al_{14}Ge_{32}$ structure. Similarly Fig. 34(b) and Fig. 35 shows all the calculated configurations for $Ba_8Al_{15}Ge_{31}$ and $Ba_8Al_{16}Ge_{30}$ structures, respectively. The Seebeck coefficient was calculated by using the BoltzTraP routine (Eq. 4.9)

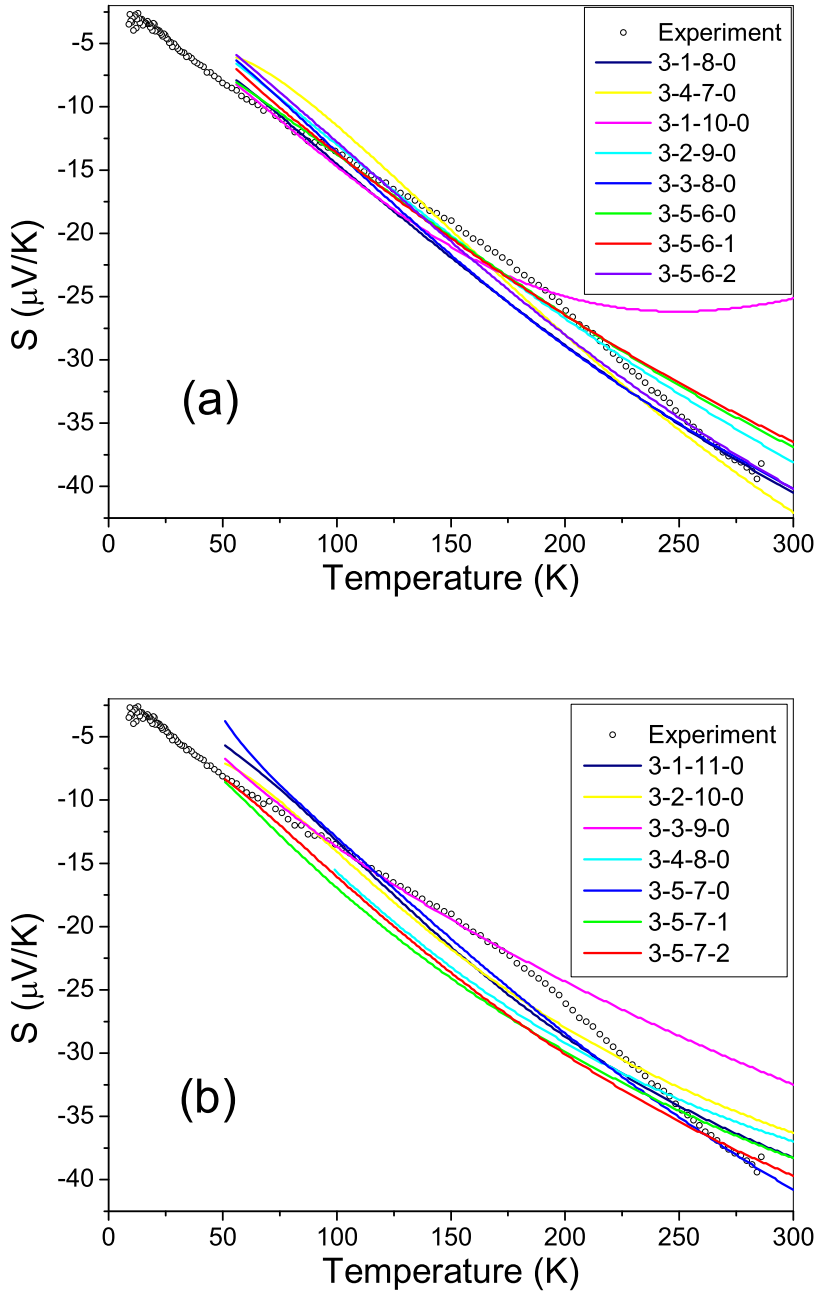

Fig. 34. Experimental Seebeck coefficient for $Ba_8Al_{16}Ge_{30}$ together with calculated curves for all type-I configurations in (a) $Ba_8Al_{14}Ge_{32}$, (b) $Ba_8Al_{15}Ge_{31}$.

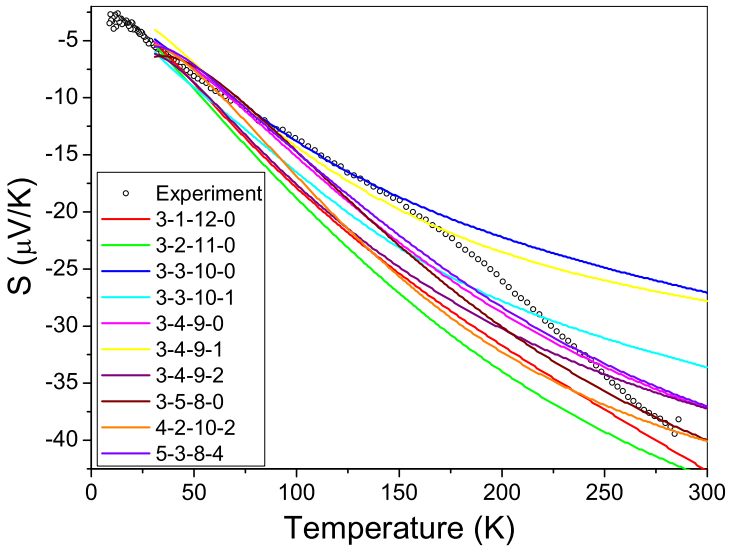

Fig. 35. Calculated Seebeck for type-I $Ba_8Al_{16}Ge_{30}$, compared with the experimental values for Al_{16}.

based on the calculated *ab initio* results. The calculation includes one adjustable parameter, which is the carrier density. The number of k-points used was 20000 as previously used for type-VIII $Ba_8Ga_{16}Sn_{30}$. From the sum of square differences between the data and each fit, the best fits correspond to $Ba_8Al_{14}Ge_{32}$ 3-3-8-0 and 3-5-6-2 configurations. Recall that from WDS measurements we obtained the composition $Ba_{7.83}Al_{14.28}Ge_{31.54}\square_{0.2}$ for Al_{16}, and from XRD we obtained a best fit for 3, 3, and 10 corresponding to the occupations of the $6c$, $16i$, and $24k$ sites, respectively. The 3-3-10-0 configuration is 0.074 eV higher than the lowest energy configuration 3-1-12-0, but its conformational entropy may be lower in this case. This composition is close to that of the 3-4-9 configuration that provided one of the best fits to the NMR lineshapes, as described in the previous section.

CHAPTER VI

CONCLUSIONS

A wide range of experiments and computational methods were implemented in rattling-type materials to successfully understand and describe some of the structural, vibrational and magnetic properties. Among these studied materials I considered Fe-Al-Zn, Al-V-La, Ba-Cu-Ge, Ba-Ga-Sn and Ba-Al-Ge clathrates.

Magnetic properties of Fe-Al and Fe-Al-Zn materials were investigated by experimental and first principles calculations. From the results I observed that the magnetization increases with the increase of Fe content along the partially occupied chains. However there is an intrinsic dilute magnetic contribution corresponding to specific local configurations for Fe, which contributes narrow peaks in the density of states near the Fermi energy. The Fe replacement on chain sites also induces an enhancement in the density of states at the Fermi level that leads to higher moments. For Fe-Al-Zn compounds the calculations predict that the full substitution of Zn for Fe in the chain leads to a reduction in the majority spin for partial Zn substitution, and a complete suppression for the $Fe_4Al_{10}Zn$ configuration.

The presence of loosely bound atoms in Al-V-La materials were investigated with *ab initio* calculations. Previous reports indicated that the main contribution to the heat capacity was due to Einstein oscillators, this behavior is confirmed from the results. I was also able to identify the contributions from all Al sites to the NMR wide-line spectrum. From QTAIM calculations the existence of two different atoms both loosely bonded in this material was confirmed.

A combination of experiments and computational studies were performed for type-I and type-VIII $Ba_8Ga_{16}Sn_{30}$ polycrystalline clathrates. NMR lineshape measurements coupled with *ab initio* calculations for type-I gave a good fit, with best

agreement corresponding to the 5-3-8-4 configuration. The best fit results indicate four Ga-Ga bonds, similar to what was previously extracted from EXAFS simulations. Note that in this case this configuration does not have the lowest energy in our ab initio results, and it is speculated that the configurational entropy might dominate. The calculated Ga-Ga bond-lengths are the shortest framework bonds, in agreement with reported experimental results, although this trend is opposite to that observed in $Ba_8Ga_{16}Ge_{30}$ and $Ba_8Al_{16}Ge_{30}$. In addition we find a significant displacement of the large-cage Ba atom. For type-VIII transport measurements are in agreement with polycrystalline clathrate results.

In the case of Ba-Cu-Ge clathrates the Zintl stabilities of these materials were studied by computational methods. It was observed that these compounds follows quite closely relation with the Zintl electron balance concept. These materials were found to be semiconductor with the Fermi level located at the band gap. From first principles it was confirmed that the most likely site for the Cu atoms is the 6*c*. Also from QTAIM calculations it is observed that the framework atoms form a network with sp^3 character and that the guest atoms can rattle inside the cages. The atoms inside the bigger cage showed a larger movement along the planes where the large cage six atoms rings are oriented.

Wide-line ^{27}Al NMR measurements on Ba-Al-Ge clathrates yielded quadrupole broadened lineshapes that help to establish the local configuration of Al atoms in these alloys. Combined with *ab initio* calculations of a number of superstructure configurations, I obtained a good fit to the NMR measurements for $x = 16$ that corresponded to the most stable configurations identified by computations. For $x < 16$ we found a splitting in the main NMR peak, coinciding with the appearance of vacancies in order to approximate a Zintl composition. Detailed analysis for $x = 12$ yielded a configuration giving very good agreement with the NMR spectrum. The

fitting indicates that Al atoms tend to shift to the $24k$ framework site for $x < 16$. From an analysis of the NMR shifts we deduced that Al non-bonding states play a significant role near the Fermi edge. Calculations also indicate rather small static distortions from the type-I structure for intrinsic $Ba_8Al_{16}Ge_{30}$, but more significant distortions with vacancies present.

In the case of $Ba_8Al_xGe_{46-x}$ WDS and XRD measurements indicated that the lattice constant varied smoothly as a function of Al content with extrapolation to that of Ba_8Ge_{43} as $x \to 0$. The vacancy count as a function of Al concentration also showed a linear behavior with a limiting value of 3 vacancies as $x \to 0$ and also remaining below the Zintl curve for large x. Resistivities decreased for lower-x samples but with similar shapes, indicating enhanced metallic behavior for low Al content. Thermoelectric transport properties showed a similar behavior as in type-VIII $Ba_8Ga_{16}Sn_{30}$. First principles computations showed that $Ba_8Al_{16}Ge_{30}$ with a balanced electron count has the lowest formation energy, as expected. However configurations with unbalanced electron counts were found to be nearly equivalent in energy, and I speculate that the departures from a Zintl model may be due to a competition between framework antibond energies and vacancy formation energies.

REFERENCES

[1] C. Uher, Semiconduct. Semimet. **69**, 139, (2001).

[2] S. M. Kauzlarich, S. R. Brown, and G. J. Snyder, Dalton Trans. **21**, 2099, (2007).

[3] G. S. Nolas, J. Poon, and M. Kanatzidis, Mater. Res. Soc. Bull. **31**, 199, (2006).

[4] M. Cutler, J. F. Leavy, and R. L. Fitzpatrick, Phys. Rev. **133**, A1143, (1964).

[5] L. D. Hicks and M. Dresselhaus, Phys. Rev. B **47**, 12727, (1993).

[6] J. M. O. Zide, D. Vashaee, Z. X. Bian, G. Zeng, J. E. Bowers, A. Shakouri, and A. C. Gossard, Phys. Rev. B **74**, 205335, (2006).

[7] G. J. Snyder and E. S. Toberer, Nature Materials **7**, 105, (2008).

[8] J. R. Drabble and C. H. L. Goodman, J. Phys. Chem. Solids **5**, 142, (1958).

[9] R. O. Carlson, J. Phys. Chem. Solids **13**, 65, (1960).

[10] H. J. Goldsmid, Proc. Phys. Soc. London Sect. B **69**, 203, (1956).

[11] C. B. Satterthwaite and R. W. Ure, Phys. Rev. **108**, 1164, (1957).

[12] H. J. Goldsmid, Proc. Phys. Soc. London **76**, 113, (1958).

[13] U. Birkholz, Z. Naturforsch. Teil A **13**, 780, (1958).

[14] A. G. Ioffe, A. V. Airapetyants, A. V. Ioffe, N.V. Kolomoets, and L. S. Stilibans, Dokl. Akad. Nauk SSSR **106**, 981, (1956).

[15] V. Fano, *CRC Handbook of Thermoelectrics.* (CRC Press, Boca Raton, FL, 1995).

[16] D. M. Rowe and C. M. Bhandari, *Modern Thermoelectrics*. (Rinehart & Winston, London, 1983).

[17] E. A. Skrabek and D. S. Trimmer, *CRC Handbook of Thermoelectrics*. (CRC Press, Boca Raton, FL, 1995).

[18] A. I. Hochbaum, R. Chen, R. D. Delgado, W. Liang, E. C. Garnett, M. Najarian, A. Majumdar, and P. Yang, Nature **451**, 163, (2008).

[19] A. I. Boukai, Y. Bunimovich, J. Tahir-Kheli, J. Yu, W. A. Goddard III, and J. R. Heath, Nature **451**, 168, (2008).

[20] C. M. Bhandari, *CRC Handbook of Thermoelectrics*. (CRC Press, Boca Raton, FL, 1995).

[21] K. W. Jang and D. H. Lee. *14th International Conference on Thermoelectrics*. (IEEE, New York, Long Beach, CA, 1995), p. 108.

[22] T. Ikeda, S. M. Haile, V. A. Ravi, H. Azizgolshani, F. Gascoin, and G. J. Snyder, Acta Mater. **55**, 1227, (2007).

[23] M. I. Aliev, A. A. Khalilova, D. G. Arsaly, R. N. Ragimov, and M. Tanogly, Inorg. Mater. **40**, 331, (2004).

[24] G. A. Slack, in *MRS Symposia Proceedings* **478** (Materials Research Society, Pittsburgh, PA, 1997), p. 47.

[25] D. G. Cahill, S. K. Watson, and R. O. Pohl, Phys. Rev. B **46**, 6131, (1992).

[26] J. S. Kasper, P. Hagenmuller, M. Pouchard, and C. Cros, Science **150**, 1713, (1965).

[27] G. S. Nolas, J. L. Cohn, G. A. Slack, and S. B. Schujman, Appl. Phys. Lett. **73**, 178, (1998).

[28] J. L. Cohn, G. S. Nolas, V. Fessatidis, T. H. Metcalf, and G. A. Slack, Phys. Rev. Lett. **82**, 779, (1999).

[29] V. L. Kuznetsov, L. A. Kuznetsova, A. E. Kaliazin, and D. M. Rowe, J. Appl. Phys. **87**, 7871, (2000).

[30] B. C. Chakoumakos, B. C. Sales, D. G. Mandrus, and G. S. Nolas, J. Alloys Compd. **296**, 80, (2000).

[31] J. H. Ross, Jr. and Yang Li, in *Nanoscale Magnetic Materials and Applications* edited by J. P. Liu, E. Fullerton, O. Gutfleisch, and D. Sellmyer, (Springer, New York, 2009), p. 105.

[32] E. N. Nenghabi and C. W. Myles, Phys. Rev. B **78**, 195202, (2008).

[33] A. F. May, E. S. Toberer, A. Saramat, and G. J. Snyder, Phys. Rev. B **80**, 125205, (2009).

[34] K. Suekuni, M. A. Avila, K. Umeo, H. Fukuoka, S. Yamanaka, T. Nakagawa, and T. Takabatake, Phys. Rev. B **77**, 235119, (2009).

[35] A. Saramat, G. Svensson, A. E. C. Palmqvist, C. Stiewe, E. Mueller, D. Platzek, S. G. K. Williams, D. M. Rowe, J. D. Bryan, and G. D. Stucky, J. Appl. Phys. **99**, 023708, (2006).

[36] E. S. Toberer, M. Christensen, B. B. Iversen, and G. J. Snyder, Phys. Rev. B **77**, 075203, (2008).

[37] H. Kawaji, H. Horie, S. Yamanaka, and M. Ishikawa, Phys. Rev. Lett. **74**, 1427, (1995).

[38] S. Paschen, W. Carrillo-Cabrera, A. Bentien, V. H. Tran, M. Baenitz Y. Grin, and F. Steglich, Phys. Rev. B **64**, 214404, (2001).

[39] J. Gryko, P. F. McMillan, R. F. Marzke, G. K. Ramachandran, D. Patton, S. K. Deb, and O. F. Sankey, Phys. Rev. B **62**, R7707, (2000).

[40] A. M. Guloy, R. Ramlau, Z. Tang, W. Schnelle, M. Baitinger, and Y. Grin, Nature **443**, 320, (2006).

[41] H. Schäfer, Annu. Rev. Mater. Sci. **15**, 1, (1985).

[42] H. Shimizu, T. Iitaka, T. Fukushima, T. Kume, S. Sasaki, N. Sata, Y. Ohishi, H. Fukuoka, and S. Yamanaka, J. Appl. Phys. **101**, 063549, (2007).

[43] W. Carrillo-Cabrera, S. Budnyk, Y. Prots, and Y. Grin, Z. Anorg. Allg. Chem. **630**, 2267, (2004).

[44] K. Moriguchi, M. Yonemura, A. Shintani, and S. Yamanaka, Phys. Rev. B **61**, 9859, (2000).

[45] R. P. Hermann, V. Keppens, P. Bonville, G. S. Nolas, F. Grandjean, G. J. Long, H. M. Christen, B. C. Chakoumakos, B. C. Sales, and D. Mandrus, Phys. Rev. Lett. **97**, 017401, (2006).

[46] H. Fukuoka, J. Kiyoto, and S. Yamanaka, Inorg. Chem. **42**, 2933, (2003).

[47] S. Saito and A. Oshiyama, Phys. Rev. B **51**, 2628, (1995).

[48] T. Kawaguchi, K. Tanigaki, and M. Yasukawa, Appl. Phys. Lett. **77**, 3438, (2000).

[49] Yang Li, Ji Chi, W. Gou, S. Khandekar, and J. H. Ross, Jr., J. Phys.: Condens. Matter. **15**, 5535, (2003).

[50] J. S. Tse, T. Iitaka, T. Kume, H. Shimizu, K. Parlinski, H. Fukuoka, and S. Yamanaka, Phys. Rev. B **72**, 155441, (2005).

[51] N. Kamakura, T. Nakano, Y. Ikemoto, M. Usuda, H. Fukuoka, S. Yamanaka ans S. Shin, and K. Kobayashi, Phys. Rev. B **72**, 014511, (2005).

[52] Y. Li, R. Zhang, Y. Liu, N. Chen, Z. P. Luo, X. Ma, G. Cao, Z. S. Feng, C. R. Hu, and J. H. Ross, Jr., Phys. Rev. B **75**, 054513, (2007).

[53] L. Qiu, M. A. White, Z. Li, J.S. Tse, C. I. Ratcliffe, C. A Tulk, J. Dong, and O. F. Sankey, Phys. Rev. B **64**, 024303, (2001).

[54] I. Fujita, K Kishimoto, M. Sato, and T. Koyanagi, J. Appl. Phys. **99**, 093707, (2006).

[55] G. K. H. Madsen, K. Schwarz, P. Blaha, and D. J. Singh, Phys. Rev. B **68**, 125212, (2003).

[56] E. Nenghabi and C.W. Myles, J. Phys.: Condens. Matter. **20**, 415214, (2008).

[57] H. Anno, M. Hokazono, M. Kawamura, J. Nagao, and K. Matsubara, in *Proceedings of the 21st International Conference on Thermoelectrics* (IEEE, New York, 2002), pp. 77-80

[58] S. Deng, Y. Saiga, K. Suekuni, and T. Takabatake, J. Appl. Phys. **108**, 073705, (2010).

[59] C. S. Lue and J. H. Ross, Jr., Phys. Rev. B **58**, 9763, (1998).

[60] B. H. Toby, J. Appl. Cryst. **34**, 210, (2001).

[61] W. Kohn and K. Sham, Phys. Rev. **140**, A1133, (1965).

[62] J. P. Perdew, K. Burke, and M. Ernzerhof, Phys. Rev. Lett. **77**, 3865, (1996).

[63] O. K. Andersen, Phys. Rev. B **12**, 3060, (1975).

[64] P. Hohenberg and W. Kohn, Phys. Rev. B **136**, B864, (1964).

[65] J. C. Slater, Phys. Rev. **51**, 846, (1937).

[66] D. J. Singh, Phys. Rev. B **43**, 6388, (1991).

[67] P. Blaha, K. Schwarz, G. Madsen, D. Kvasnicka, and J. Luitz, *Wien2k: An Augmented Plane Wave+Local Orbitals Program for Calculating Crystal Properties*. (Technische Universität Wien, Wien, Austria, 2001).

[68] S. Pillet, M. Souhassou, C. Lecomte, K. Schwarz, P. Blaha, M. Rerat, A. Lichanot, and P. Roversi, Acta Cryst. Sect. A **57**, 290, (2001).

[69] P. Blaha, K. Schwarz, W. Faber, and J. Luitz, Hyperf. Int. **126**, 389, (2000).

[70] T. J. Bastow and G. W. West, J. Phys.: Condens. Matter. **15**, 8389, (2003).

[71] J. Cuny, S. Messaoudi, V. Alonzo, E. Furet, J. F. Halet, E. Le Fur, S. E. Ashbrook, C. J. Pickard, R. Gautier, and L. Le Polles, J. Comput. Chem. **29**, 2279, (2008).

[72] G. C. Carter, L. H. Bennett, and D. J. Kahan, *Metallic Shifts in NMR*. (Pergamon, Oxford, UK, 1977).

[73] G. H. Stauss, J. Chem. Phys. **40**, 1988, (1964).

[74] R. F. W. Bader, *Atoms in Molecules: A Quantum Theory (International Series of Monographs on Chemistry).* (Oxford University Press, Oxford, UK, 1990).

[75] P. B. Allen, in *Quantum Theory of Real Materials* edited by J. R. Chelikowsky and S. G. Louie, (Kluwer, Boston, 1996), p. 219.

[76] C. S. Lue, Y. Öner, D. G. Naugle, and J. H. Ross, Jr., Phys. Rev. B **63**, 184405, (2001).

[77] J. Chi, X. Zheng, S. Y. Rodriguez, Y. Li, W. Gou, V. Goruganti, K. D. D. Rathnayaka, and J. H. Ross, Jr., Phys. Rev. B **82**, 174419, (2010).

[78] T. Fujiwara and T Yokokawa, Phys. Rev. Lett. **66**, 333, (1991).

[79] J. Delahaye, T. Schaub, C. Berger, and Y. Calvayrac, Phys. Rev. B **67**, 214201, (2003).

[80] R. Widmer, P. Gröning, M. Feuerbacher, and O. Gröning, Phys. Rev. B **79**, 104202, (2009).

[81] A. D. Caplin, G. Grüner, and J. B. Dunlop, Phys. Rev. Lett. **30**, 1138, (1973).

[82] M. Jahnátek, M. Krajčí, and J. Hafner, J. Phys: Condens. Matter. **15**, 5675, (2003).

[83] Sergio Y. Rodriguez, V. Goruganti, K. D. D. Rathnayaka, Laziz Saribaev, Ji Chi, and J. H. Ross, Jr., submitted to Phys. Rev. B, March 2011.

[84] P. J. Brown, Acta Cryst. **10**, 133, (1957).

[85] G. T. de Laissardiere, D. Nguyen-Manh, and D. Mayou, Prog. Mater. Sci. **50**, 679, (2005).

[86] C. Gatti, Z. Kristallogr. **229**, 399, (2005).

[87] H. Zhang, J. T. Zhao, M. B. Tang, Z. Y. Man, H. H. Chen, and X. X. Yang, J. Alloy Compd. **476**, 1, (2009).

[88] H. Fukuyama and R. Kubo, J. Phys. Soc. Jpn. **28**, 570, (1970).

[89] A. Principi, M. Polini, G. Vignale, and M. I. Katsnelson, Phys. Rev. Lett. **104**, 225503, (2010).

[90] G. Cordier and P. Woll. J. Less-Common Met. **169**, 291, (1990).

[91] J. H. Chen. Texas A&M Universiy, private communication, (2011).

[92] S. Johnsen, A. Bentien, G. K. H. Madsen, M. Nygren, and B. B. Iversen, *Proceedings of the 26th International Conference on Thermoelectrics* (IEEE, New York, 2007), p. 219.

[93] R. F. W. Herrmann, K. Tanigaki, T. Kawaguchi, S. Kuroshima, and O. Zhou, Phys. Rev. B **60**, 13245, (1999).

[94] M. A. Avila, K. Suekuni, K. Umeo, H. Fukuoka, S. Yamanaka, and T. Takabatake, Appl. Phys. Lett. **92**, 041901, (2008).

[95] D. Huo, T. Sakata, T. Sasakawa, M. A. Avila, M. Tsubota, F. Iga, H. Fukuoka, S. Yamanaka, S. Aoyagi, and T. Takabatake, Phys. Rev. B **71**, 075113, (2005).

[96] S. Y. Rodriguez, X. Zheng, and J. H. Ross, Jr., in *MRS Symposia Proceedings* **1267** (Material Research Society, Pittsburgh, 2010), p. DD04.07.

[97] N. P. Blake, D. Bryan, S. Latturner, L. Mollnitz, G. D. Stucky, and H. Metiu, J. Chem. Phys. **114**, 10063, (2001).

[98] W. Gou, S. Y. Rodriguez, Y. Li, and J. H. Ross, Jr., Phys. Rev. B **80**, 144108, (2009).

[99] M. Kozina, F. Bridges, Y. Jiang, M. A. Avila, K. Suekuni, and T. Takabatake, Phys. Rev. B **80**, 212101, (2009).

[100] Y. Jiang, F. Bridges, M. A. Avila, T. Takabatake, J. Guzman, and G. Kurczveil, Phys. Rev. B **78**, 014111, (2008).

[101] U. Aydemir, C. Candolfi, H. Borrmann, M. Baitinger, A. Ormeci, W. Carrillo-Cabrera, C. Chubilleau, B. Lenoir, A. Dauscher, N. Oeschler, F. Steglich, and Yu. Grin, Dalton Trans. **39**, 1078, (2010).

[102] J. R. Cooper, Phys. Rev. B **9**, 2778, (1974).

[103] G. Nolas, J. L. Cohn, J. S. Dyck, C. Uher, G. A. Lamberton, and T. M. Tritt, J. Mater. Res. **19**, 3556, (2004).

[104] W. Gou, Texas A&M Universiy, Ph. D. Dissertation, 2008.

[105] T. Dahm and K. Ueda, Phys. Rev. Lett. **99**, 187003, (2007).

[106] J. D. Bryan, N. P. Blake, H. Metiu, G. D. Stucky, B. B. Iversen, and A. Bentien, J. Appl. Phys. **92**, 7281, (2002).

[107] Y. Mudryk, P. Rogl, C. Paul, S. Berger, E. Bauer, G. Hilscher, C. Godart, and H. Nöel, J. Phys.: Condens. Matter **14**, 7991, (2002).

[108] T. M. Tritt, *Recent Trends in Thermoelectric Materials.* (Academic Press, New York, 2001).

[109] S. Johnsen, A. Bentien, G. K. H. Madsen, and B. B. Iversen, Chem. Mater. **18**, 4633, (2006).

[110] I. Zeiringer, MingXing Chen, I. Bednar, E. Royanian, E. Bauer, R. Podloucky, A. Grytsiv, P. Rogl, and H. Effenberger, Acta Mater. **59**, 2368, (2011).

[111] G. K. H. Madsen and D. J. Singh, Comp. Phys. Commun. **175**, 67, (2006).

[112] K. Koga, T. Kamei, K. Akai, K. Oshiro, and M. Matsuura, in *Proceedings of the 24th International Conference on Thermoelectrics* (IEEE, New York, 2005), p. 222.

[113] M. Christensen and B. B. Iversen, Chem. Mater. **19**, 4896, (2007).

[114] T. Uemura, K. Akai, K. Koga, T. Tanaka, H. Kurisu, S. Yamamoto, K. Kishimoto, T. Koyanagi, and M. Matsuura, J. Appl. Phys. **104**, 013702, (2008).

[115] N. L. Okamoto, K. Kishida, K. Tanaka, and H. Inui, J. Appl. Phys. **100**, 073504, (2006).

[116] B. Eisenmann, H. Schäfer, and R. Zagler, J. Less-Common Met. **118**, 43, (1986).

[117] E. N. Nenghabi and C. W. Myles, J. Phys.: Condens. Matter **20**, 415214, (2008).

[118] C. L. Condron, J. Martin, G. S. Nolas, P. M. B. Piccoli, A. J. Schultz, and S. M. Kauzlarich, Inorg. Chem. **45**, 9381, (2006).

[119] N. W. Ashcroft and N. D. Mermin, *Solid State Physics*. (Saunders, New York, 1976).

[120] H. Fukuoka, J. Kiyoto, and S. Yamanaka, J. Solid State Chem. **175**, 237, (2003).

[121] S. Y. Rodriguez, Y. Li, and J. H. Ross, Jr., Phys. Rev. B **80**, 064111, (2010).

[122] G. J. Miller. In *Chemistry, Stucture, and Bonding of Zintl Phases and Ions*, edited by S. M. Kauzlarich, (VCH, New York, 1996) p. 1.

[123] C. Candolfi, U. Aydemir, M. Baitinger, N. Oeschler, F. Steglich, and Y. Grin, JEM **38**, 12, (2009).

[124] J. M. Ziman, *Principles of the Theory of Solids.* (Cambridge University Press, London, UK, 1972).

[125] Yang Li, Yang Liu, N. Chen, G. Cao, Z. Feng, and J. H. Ross, Jr., Phys. Lett. A **345**, 398, (2005).

VITA

Sergio Yanuen Rodríguez Robles is from Zacatecas, Mexico. He received his B.S. degree in physics from Universidad Autonoma de Zacatecas, Mexico in 2002. His work was in the development of an efficient algorithm for inversion of tridiagonal matrices. He obtained his M.S. degree in physics at the University of Texas at El Paso, in 2004. The field of specialization was on surface characterization of CdS/CdTe solar cells. He received his Ph.D. degree in physics from Texas A&M University in 2011, with emphasis on computational and experimental studies on thermoelectric clathrate materials. His email address is yanuen@yahoo.com.

Contact information: Department of Physics and Astronomy, c/o Dr. Joseph H. Ross, Jr., Texas A&M University, College Station, TX 77843-4242.

The typist for this thesis was Sergio Yanuen Rodríguez Robles.